NAVAL POSTGRADUATE SCHOOL

MONTEREY, CALIFORNIA

THESIS

ADVANCED TECHNIQUES TO IMPROVE THE PERFORMANCE OF OFDM WIRELESS LAN

by

Michail Segkos

June 2004

Thesis Advisor:	Tri T. Ha
Thesis Co-Advisor:	Brett H. Borden

Approved for public release; distribution is unlimited

THIS PAGE INTENTIONALLY LEFT BLANK

REPORT DOCUMENTATION PAGE			Form Approved OMB No. 0704-0188
Public reporting burden for this collection of information is estimated to average 1 hour per response, including the time for reviewing instruction, searching existing data sources, gathering and maintaining the data needed, and completing and reviewing the collection of information. Send comments regarding this burden estimate or any other aspect of this collection of information, including suggestions for reducing this burden, to Washington headquarters Services, Directorate for Information Operations and Reports, 1215 Jefferson Davis Highway, Suite 1204, Arlington, VA 22202-4302, and to the Office of Management and Budget, Paperwork Reduction Project (0704-0188) Washington DC 20503.			
1. AGENCY USE ONLY *(Leave blank)*	**2. REPORT DATE** June 2004	**3. REPORT TYPE AND DATES COVERED** Master's Thesis	
4. TITLE AND SUBTITLE: Advanced Techniques to Improve the Performance of OFDM Wireless LAN.			**5. FUNDING NUMBERS**
6. AUTHOR(S) Michail Segkos			
7. PERFORMING ORGANIZATION NAME(S) AND ADDRESS(ES) Naval Postgraduate School Monterey, CA 93943-5000			**8. PERFORMING ORGANIZATION REPORT NUMBER**
9. SPONSORING /MONITORING AGENCY NAME(S) AND ADDRESS(ES) N/A			**10. SPONSORING/MONITORING AGENCY REPORT NUMBER**
11. SUPPLEMENTARY NOTES The views expressed in this thesis are those of the author and do not reflect the official policy or position of the Department of Defense or the U.S. Government.			
12a. DISTRIBUTION / AVAILABILITY STATEMENT Approved for public release; distribution is unlimited.			**12b. DISTRIBUTION CODE**

13. ABSTRACT *(maximum 200 words)*

OFDM systems have experienced increased attention in recent years and have found applications in a number of diverse areas including telephone-line based ADSL links, digital audio and video broadcasting systems, and wireless local area networks (WLAN). Orthogonal frequency-division multiplexing (OFDM) is a powerful technique for high data-rate transmission over fading channels. However, to deploy OFDM in a WLAN environment, precise frequency synchronization must be maintained and tricky frequency offsets must be handled. In this thesis, various techniques to improve the data throughput of OFDM WLAN are investigated. A simulation tool was developed in Matlab to evaluate the performance of the IEEE 802.11a physical layer. We proposed a rapid time and frequency synchronization algorithm using only the short training sequence of the IEEE 802.11a standard, thus reducing the training overhead to 50%. Particular attention was paid to channel coding, block interleaving and antenna diversity. Computer simulation showed that drastic improvement in error rate performance is achievable when these techniques are deployed.

14. SUBJECT TERMS OFDM, WLAN, IEEE 802.11a, Exponential Channel Model, Packet Detection, Frame Synchronization, Frequency Synchronization, Carrier Offset, Phase Noise, Pilot Phase Tracking, Channel Estimation, Equalization, Scrambling, Convolutional Coding, Interleaving, Maximal Ratio Combining, Selection Diversity, Viterbi Algorithm, Soft Decision Decoding, Puncturing			**15. NUMBER OF PAGES** 135
			16. PRICE CODE
17. SECURITY CLASSIFICATION OF REPORT Unclassified	**18. SECURITY CLASSIFICATION OF THIS PAGE** Unclassified	**19. SECURITY CLASSIFICATION OF ABSTRACT** Unclassified	**20. LIMITATION OF ABSTRACT** UL

NSN 7540-01-280-5500

Standard Form 298 (Rev. 2-89)
Prescribed by ANSI Std. 239-18

THIS PAGE INTENTIONALLY LEFT BLANK

Approved for public release; distribution is unlimited

ADVANCED TECHNIQUES TO IMPROVE THE PERFORMANCE OF OFDM WIRELESS LAN

Michail Segkos
Lieutenant, Hellenic Navy
B.S., Hellenic Naval Academy, 1994

Submitted in partial fulfillment of the
requirements for the degree of

MASTER OF SCIENCE IN ELECTRICAL ENGINEERING
and
MASTER OF SCIENCE IN APPLIED PHYSICS

from the

NAVAL POSTGRADUATE SCHOOL
June 2004

Author: Michail Segkos

Approved by: Tri T. Ha
Thesis Advisor

Brett H. Borden
Co-Advisor

James Luscombe
Chairman, Department of Physics

John P. Powers
Chairman, Department of Electrical Engineering

THIS PAGE INTENTIONALLY LEFT BLANK

ABSTRACT

OFDM systems have experienced increased attention in recent years and have found applications in a number of diverse areas including telephone-line based ADSL links, digital audio and video broadcasting systems, and wireless local area networks (WLAN). Orthogonal frequency-division multiplexing (OFDM) is a powerful technique for high data-rate transmission over fading channels. However, to deploy OFDM in a WLAN environment, precise frequency synchronization must be maintained and tricky frequency offsets must be handled. In this thesis, various techniques to improve the data throughput of OFDM WLAN are investigated. A simulation tool was developed in Matlab to evaluate the performance of the IEEE 802.11a physical layer. We propose a rapid time and frequency synchronization algorithm using only the short training sequence of the IEEE 802.11a standard, thus reducing the training overhead by 50%. Particular attention was paid to channel coding, block interleaving and antenna diversity. Computer simulation showed that drastic improvement in error rate performance is achievable when these techniques are deployed.

THIS PAGE INTENTIONALLY LEFT BLANK

TABLE OF CONTENTS

I. INTRODUCTION....1
A. OBJECTIVE....2
B. THESIS OUTLINE....3

II. BACKGROUND....5
A. MULTIPATH FADING....5
1. Attenuation in Signal Strength....7
2. Time Dispersion....8
3. Frequency Broadening....11
4. Characterization of Small Fading....11
B. CHANNEL MODEL....12
1. Impulse Response of the Time Varying Channel....12
2. Exponential Channel Model (IEEE 802.11)....14
3. Rayleigh Fading....18
C. OFDM OVERVIEW....19
1. Concept of Parallel Data Transmission....20
2. Orthogonal Frequency Division Multiplexing (OFDM)....22
a. OFDM Implementation....24
b. Cyclic Prefix....24
D. IEEE 802.11a OVERVIEW....26
1. Specifications....26
2. OFDM Physical Layer (PHY) Architecture....28
3. MAC Layer....30
E. SUMMARY....30

III. SYNCHRONIZATION....31
A. IEEE 802.11a PREAMBLE....31
B. PACKET DETECTION....34
1. Using the Preamble for Packet Detection....35
2. Packet Detection When Preamble Is Not Available....37
C. FRAME/SYMBOL TIME SYNCHRONIZATION....38
1. Symbol Timing in a Multipath Channel....39
D. FREQUENCY SYNCHRONIZATION....41
1. Maximum-Likelihood (ML) Estimation of Frequency-Offset....45
2. Properties of the Frequency-offset Estimation Algorithm....47
E. COMBINED FRAME AND FREQUENCY ESTIMATION....48
F. SAMPLING CLOCK ERROR....56
G. CARRIER PHASE TRACKING....58
H. CHANNEL ESTIMATION....60
1. Frequency Domain Approach....60
2. Time Domain Approach....61
3. Simulation and Results....62

I. EQUALIZATION 64
J. SUMMARY 64

IV. PERFORMANCE OF IEEE 802.11A 67
A. OVERVIEW OF THE PPDU ENCODING PROCESS 67
B. SIMULATION TOOL OVERVIEW 68
C. TRANSMITTER 70
1. PLCP DATA Scrambler 70
2. Convolutional Encoder 71
3. Bit Puncturing 72
4. Interleaver 73
5. Modulation Mapping 76
6. OFDM Multiplexing 77
D. RECEIVER 80
E. PERFORMANCE OF IEEE 802.11a IN AWGN 82
F. PERFORMANCE OF IEEE 802.11a IN MULTIPATH FADING 87
G. SPACE DIVERSITY 94
1. Selection Diversity 95
2. Maximal Ratio Combining 96
H. SUMMARY 98

V. CONCLUSIONS AND FUTURE WORK 99
A. CONCLUSIONS 99
B. FUTURE WORK 100

APPENDIX A: PHYSICAL MECHANISMS LEADING TO SMALL-SCALE MULTIPATH FADING 103

LIST OF REFERENCES 107

INITIAL DISTRIBUTION LIST 111

LIST OF FIGURES

Figure 1. Multipath Interference 6
Figure 2. Large and Small-scale Fading (From Ref. [3].) 7
Figure 3. PDS for a Small Room with $\sigma_\tau = 50$ ns (After Ref. [3].) 9
Figure 4. Average Power Profile for $\tau_{rms} = 50$ ns, $f_s = 20$ MHz 16
Figure 5. Sample Realization for $\tau_{rms} = 50$ ns, $f_s = 20$ MHz 17
Figure 6. Block Diagram of Flat Fading & ISI (After Ref. [12].) 18
Figure 7. Channel Impulse Response in Time and Frequency Domain (After Ref. [14].) 20
Figure 8. FDM with Subbands 21
Figure 9. Overlapping Orthogonal Carriers 22
Figure 10. Orthogonal Frequency Division Multiplexing 23
Figure 11. Cyclic Prefix (CP) in OFDM Symbol 25
Figure 12. PPDU in IEEE 802.11a (After Ref. [19].) 28
Figure 13. PLCP Preamble (From Ref. [19].) 32
Figure 14. Short Training Sequence (Real Part.) 32
Figure 15. Long Training Sequence (Real Part.) 33
Figure 16. Block Diagram of Delay and Correlate Algorithm 35
Figure 17. Packet Detection Using the Preamble (SNR = 0 dB.) 36
Figure 18. Packet Detection Algorithm Based on Received Signal Energy (SNR = 0 dB.) 37
Figure 19. Response of the Symbol Timing Cross-correlator 39
Figure 20. DFT Window Timing 40
Figure 21. Performance of BPSK/QPSK, 16-QAM and 64-QAM in AWGN 42
Figure 22. Distortion as Function of Relative Frequency-offset 43
Figure 23. Distortion as Function of Oscillator Linewidth 44
Figure 24. Symbol Timing Estimate in AWGN, SNR = 10 dB 50
Figure 25. PDF of Symbol-timing Estimate in AWGN, SNR = 10 dB 51
Figure 26. PDF of Symbol-timing Estimate in 50 ns Delay Spread, SNR = 10 dB 52
Figure 27. PDF of Frequency-offset Estimate in AWGN, SNR = 10 dB 53
Figure 28. PDF of Frequency-offset Estimate in 50 ns Delay Spread, SNR = 10 dB 53
Figure 29. PDF of SNR Estimate in 50nsec Delay Spread, SNR = 10 dB 55
Figure 30. Flow Chart of the Proposed Synchronization Algorithm 56
Figure 31. Constellation Rotation with 3-kHz Frequency Error 58
Figure 32. Performance Comparison of Channel Estimation Algorithms 63
Figure 33. Simplified Block Diagram of the IEEE 802.11a Transceiver (After Ref. [19].) 67
Figure 34. Snapshot of Graphical User Interface 68
Figure 35. Block Diagram of the Main Function 69
Figure 36. Frame Synchronous Scrambler/Descrambler (After Ref. [19].) 71
Figure 37. Convolutional Encoder of IEEE 802.11a (From Ref. [19].) 71

Figure 38. Bit Puncturing Pattern in the IEEE 802.11a (After Ref. [19].) 72
Figure 39. Bit Error Rate of IEEE 802.11a 12-Mbps Mode with and without Interleaving in 75-ns RMS Delay Spread Fading Channel 75
Figure 40. Packet Error Rate of IEEE 802.11a 12-Mbps Mode with and without Interleaving in 75-ns RMS Delay Spread Fading Channel 75
Figure 41. 64-QAM Constellation Bit Encoding 76
Figure 42. Inputs and Outputs of IFFT (From Ref.[19].) 77
Figure 43. Time Domain Representation of the Transmitted Packet 78
Figure 44. PSD of the Transmitted Packet 79
Figure 45. Baseband Receiver Functional Block Diagram 80
Figure 46. Subcarrier Constellation at the Demodulator (SNR = 18 dB, AWGN) 82
Figure 47. Coding Gain in BER of IEEE 802.11a 54-Mbps Mode, in AWGN 83
Figure 48. Coding Gain in PER of IEEE 802.11a 54-Mbps Mode, in AWGN 84
Figure 49. Coding Gain in BER of IEEE 802.11a 48-Mbps Mode, in AWGN 85
Figure 50. Coding Gain in PER of IEEE 802.11a 48-Mbps Mode, in AWGN 85
Figure 51. Performance Comparison of all IEEE 802.11a modes in AWGN and SDD ... 86
Figure 52. Subcarrier Constellation of IEEE 802.11a 54-Mbps mode at the Demodulator (SNR = 20 dB, 50-ns RMS Delay Spread.) 88
Figure 53. Equalized Subcarrier Constellation of IEEE 802.11a 54-Mbps Mode at the Demodulator (SNR = 20 dB, 50-ns RMS Delay Spread.) 89
Figure 54. BER of IEEE 802.11a 6-Mbps Mode in Rayleigh Fading, 50-ns RMS Delay 90
Figure 55. Performance of IEEE 802.11a BPSK/QPSK Modulation in an Exponential-decaying Channel, 50-ns rms Delay Spread 91
Figure 56. Performance of IEEE 802.11a 16-QAM Modulation in an Exponential-decaying Channel, 50 ns RMS Delay Spread 92
Figure 57. Performance of IEEE 802.11a 64-QAM Modulation in an Exponential-decaying Channel, 50 ns RMS Delay Spread 93
Figure 58. Packet Error Rate of IEEE 802.11a Using Weighted SDD in an Exponential-decaying Channel, 50 ns RMS Delay Spread 93
Figure 59. Performance of IEEE 802.11a 54-Mbps Mode, Employing Selection Diversity in an Exponential-decaying Channel, 50-ns RMS Delay Spread 95
Figure 60. Performance of IEEE 802.11a 54-Mbps Mode, Employing MRC Diversity in an Exponential-decaying Channel, 50-ns RMS Delay Spread 97
Figure 61. Two Plane-wave Model 103
Figure 62. Doppler Spread for a Two Plane-wave Model (After Ref. [6].) 105

LIST OF TABLES

Table 1. Typical RMS Delay Spread for Indoor Environments (After Ref. [8].) 10
Table 2. Types of Small Scale Fading (After Ref. [5].) 12
Table 3. Rate-dependent Parameters of IEEE 802.11a (From Ref. [19].) 27
Table 4. Timing-related Parameters of IEEE 802.11a (From Ref. [19].) 27
Table 5. Free Distances of the Codes Used in IEEE 802.11a (After Ref. [28].) 73
Table 6. Modulation-dependent Normalization Factor K_{MOD} 77

THIS PAGE INTENTIONALLY LEFT BLANK

LIST OF ACRONYMS AND/OR ABBREVIATIONS

ADC	Analog to Digital Converter
ADSL	Asymmetric Digital Subscriber Line
AP	Access Point
AWGN	Additive White Gaussian Noise
BER	Bit Error Rate
BPSK	Binary Phase Shift Keying
CCA	Clear Channel Assessment
CIR	Channel Impulse Response
CP	Cyclic Prefix
CSMA-CA	Carrier Sense Multiple Access with Collision Avoidance
CTF	Channel Transfer Function
CTS	Clear to Send
DAB	Digital Audio Broadcasting
DAC	Digital to Analog Converter
DEMUX	Demultiplexer
DFT	Discrete Fourier Transform
DMT	Discrete Multi-tone
DVB-T	Digital Video Broadcasting – Terrestrial
ETSI	European Telecommunications Standard Institute
FDM	Frequency Division Multiplexing
FEC	Forward Error Correction
FFT	Fast Fourier Transform
FIR	Finite Impulse Response
FSK	Frequency shift keying
GUI	Graphical User Interface
HDD	Hard Decision Decoding
HIPERLAN/2	High Performance Local Area Network Type 2
ICI	Inter-carrier Interference

IDFT	Inverse Discrete Fourier Transform
IEEE	Institute of Electrical and Electronics Engineers
IFFT	Inverse Fast Fourier Transform
ISI	Inter-symbol Interference
LAN	Local Area Network
LO	Local Oscillator
MAC	Medium Access Control
MCM	Multicarrier Modulation
MIMO	Multiple Input Multiple Output
MISO	Multiple Input Single Output
MPDU	MAC Protocol Data Units
MRC	Maximal Ratio Combining
MT	Mobile Terminal
MUX	Multiplexer
NMSE	Normalized Mean Square Error
OFDM	Orthogonal Frequency Division Multiplexing
PDF	Probability Density Function
PDS	Power Delay Spectrum
PER	Packet Error Rate
PHY	Physical Layer
PLCP	Physical Layer Convergence Protocol
PMD	Physical Medium Dependent
PPDU	PLCP Protocol Data Unit
PSD	Power Spectrum Density
PSDU	PHY Service Data Units
QAM	Quadrature Amplitude Modulation
QPSK	Quadrature Phase Shift Keying
RF	Radio Frequency
RMS	Root Mean Square
RTS	Request to Send

SC	Single Carrier
SDD	Soft Decision Decoding
SIFS	Short Inter-frame Spacing
SIMO	Single Input Multiple Output
SNR	Signal to Noise Ratio
WLAN	Wireless Local Area Network
WSSUS	Wide-sense Stationary Uncorrelated Scattering

THIS PAGE INTENTIONALLY LEFT BLANK

EXECUTIVE SUMMARY

With the integration of Internet and multimedia applications in next generation wireless communications, the demand for reliable high data rate services and increasingly greater bandwidth capacity is rapidly growing. The next evolution of wireless will be in data communications applications that can deliver broadband services to anyone, any-time, anywhere. From the military perspective, reliable communications are critical on the modern battlefield. Individual units require a steady flow of accurate information to remain effective.

Multicarrier modulation, in particular orthogonal frequency division multiplexing (OFDM), has been successfully applied to a wide variety of digital communications applications for several years. Although OFDM has been chosen as the physical layer standard for many wireless local area networks, such as IEEE 802.11a, 802.11g, and HIPERLAN/2, the theory, algorithms, and implementation techniques remain subjects of current interest. This thesis is intended to be a concise summary of current techniques to improve performance of wireless networks employing OFDM technology.

The orthogonal nature of the OFDM subchannels allows them to be overlapped, thereby increasing the spectral efficiency. Another advantage of OFDM is its ability to handle the effects of multipath delay spread. In any radio transmission, the channel spectral response is not flat. It has fades or nulls in the frequency response due to reflections causing cancellation of certain frequencies at the receiver. For narrowband transmissions, if the null in the frequency response occurs at the transmission frequency, then the entire signal can be lost.

Multipath delay spread can also lead to inter-symbol interference. This is due to a delayed multipath signal overlapping with the following symbol. This problem is solved by adding a guard interval to each OFDM symbol. Inter-carrier interference (ICI) can be avoided by making the guard interval a cyclic extension of the OFDM symbol.

There are, however, certain negatives associated with this technique. It is more sensitive to carrier frequency offset and sampling clock mismatch than single carrier systems. Therefore, a fine synchronization algorithm is necessary at the receiver. Since many OFDM systems, such as the IEEE 802.11a, employ coherent modulation schemes, channel estimation is mandatory. If the receiver knows the channel's frequency response, then equalization can be performed by a simple division in the frequency domain. A new rapid synchronization algorithm is presented in this thesis in which only the short training sequence is used for both time and frequency synchronization. This algorithm can also be used for SNR estimation, so an appropriate data rate mode can be selected to optimize network performance. If the channel is known at the receiver, the long training sequence of the IEEE 802.11a system can be skipped, thus reducing the training overhead by 50%

The thesis concludes with performance evaluations of several operational modes of the IEEE 802.11a system. For that reason, a simulation toolbox was developed in Matlab. This toolbox consists of more than 40 functions emulating the sub-blocks of the IEEE 802.11a transceiver. The Graphical User Interface (GUI) was carefully designed to serve two main purposes:

- Allow testing of the various algorithms presented in this thesis, and
- Allow evaluating all available operational modes of the IEEE 802.11a Physical layer under multipath fading channel and Additive White Gaussian Noise (AWGN).

Moreover, a modular approach was adopted to allow future modifications of the toolbox or independent use of each function in other projects. For instance, the channel function can be slightly modified to include jamming or multi-user interference.

The Bit Error Rate (BER) and the Packet Error Rate (PER) were computed using Monte-Carlo simulations. The impact of channel coding, interleaving and receiver diversity on the data throughput was emphasized. The IEEE 802.11a system was evaluated under Additive White Gaussian Noise (AWGN) where it was found that the coding gain can be 3 to 5.5 dB for hard and soft decision decoding, respectively. Evaluation was also performed under multipath fading channel conditions. It was shown that the channel cod-

ing alone cannot recover the signal, and thus additional signal processing is required at the receiver. This processing involves equalization and any kind of frequency or space diversity. Frequency diversity can be achieved by data interleaving or by weighting the soft decisions with the channel estimates. Space diversity can be achieved by multiple antennas with uncorrelated signals. Frequency diversity can achieve a performance gain of 36 to 40 dB for all operational modes of IEEE 802.11a. If combined with space diversity (such as maximal ratio combining), the performance gain can be tremendous and excellent data throughput can be achieved.

THIS PAGE INTENTIONALLY LEFT BLANK

ACKNOWLEDGMENTS

First and foremost I am grateful to my beautiful wife, Eva, who patiently and lovingly stood by me through the rigors of my research here at the Naval Postgraduate School. Words cannot express my love and gratitude for all she has done.

Secondly I would like to thank my thesis advisors, Dr. Tri Ha and Dr. Brett Borden, for their invaluable help, advice and insightful mentoring during the development of this thesis. Thanks go out as well to my editor, Ron Russell, for his attentive assistance.

Finally, I would like to express my deepest gratitude to the Hellenic Navy for providing me the opportunity to pursue my postgraduate degree.

THIS PAGE INTENTIONALLY LEFT BLANK

I. INTRODUCTION

Orthogonal Frequency Division Multiplexing (OFDM) is a multicarrier transmission technique whose history dates back to the mid-1960's. Although the concept of OFDM has been around for a long time, it has only recently been recognized as an excellent method for high speed bi-directional wireless data communication. The first systems using this technology were military HF radio links. Today, this technology is used in wireless LAN standards such as IEEE 802.11a, IEEE 802.11g and the European Telecommunications Standard Institute (ETSI) Hiperlan/2. In addition, it is used in broadcast systems such as Asymmetric Digital Subscriber Line (ADSL), radio (DAB: Digital Audio Broadcasting) and TV (DVB-T: Digital Video Broadcasting-Terrestrial). In terms of military applications, the OPNET version 7 comes with an IEEE 802.11 model and it can be modified to function as an IEEE 802.11a or IEEE 802.11g WLAN.

OFDM efficiently squeezes multiple modulated carriers tightly together reducing the required bandwidth but keeping the modulated signals orthogonal so they do not interfere with each other. Any digital modulation technique can be used on each carrier and different modulation techniques can be used on separate carriers. The outputs of the modulated carriers are added together before transmission. At the receiver, the modulated carriers must be separated before demodulation. The traditional method of separating the bands is to use filters.

The orthogonal nature of the OFDM sub-channels allows them to be overlapped, thereby increasing the spectral efficiency. In other words, as long as orthogonality is maintained, there will be no Intercarrier Interference (ICI) in an OFDM system. In any real implementation, however, several factors will cause a certain loss in orthogonality. Designing a system that will minimize these losses therefore becomes a major technical focus.

Another advantage to OFDM is its ability to handle the effects of multipath delay spread. In any radio transmission, the channel frequency response is not flat. It has fades or nulls in the response due to reflections causing cancellation of certain frequencies at

the receiver. For narrowband transmissions, if the null in the frequency response occurs at the transmission frequency, then the entire signal can be lost.

Multipath delay spread can also lead to ISI. This is due to a delayed multipath signal overlapping with the subsequent symbol. This problem is solved by adding a time domain guard interval to each OFDM symbol. Inter-carrier interference (ICI) can be avoided by making the guard interval a cyclic extension of the OFDM symbol.

There are, however, certain negatives associated with this technique. It is more sensitive to carrier frequency offset and sampling clock mismatch than the single carrier systems. The phase noise and frequency offset of the receiver's local oscillators can significantly degrade performance.

The incorporation of pilot subcarrier symbols and a known training sequence in the transmitted OFDM symbol stream, either in addition to or as part of the OFDM symbols themselves, allows for the correction of such effects as transmitter/receiver carrier frequency and sampling frequency offsets, and fading due to multipath transmission. The training symbols and the pilot subcarrier symbols are known to the receiver; hence the received symbols can be compared against the reference symbols and the result used to characterize the impulse response of the transmission channel. The impulse response can be used to provide channel equalization information at the receiver. Additionally, the channel information can be sent back to the transmitter to pre-distort data prior to transmission and avoid high peak-to-average ratio signals.

A. OBJECTIVE

The objective of this thesis was to discuss and simulate techniques to mitigate the degradation caused by some major OFDM based WLAN impairments such as multipath fading, phase noise and frequency offset. A new rapid synchronization algorithm is proposed, where only the short training sequence of the IEEE 802.11a standard is required for time and frequency synchronization. Hence, the overhead is reduced by 50% Additionally, a simulation toolbox was developed in Matlab, where the bit error rate and packet error rate of the IEEE 802.11a system is evaluated under several operational modes using Monte-Carlo simulations.

B. THESIS OUTLINE

The thesis starts with a discussion of indoor propagation channels, followed by an overview of the basics of OFDM and the IEEE 802.11a standard. Next, readers are lead through a complete design cycle of an OFDM transceiver, starting with channel estimation and synchronization functionality, and carried through to actual realizations.

In particular, this thesis is organized as follows:

Chapter II discusses the multipath channel models used in this thesis, provides a brief overview of OFDM WLAN and offers the reader a brief description of the physical layer specifications for the IEEE 802.11a standard.

Chapter III provides a detailed discussion of many of the popular synchronization algorithms used in OFDM networks. Specifically, packet detection, sample clock estimation and correction, fine time synchronization and channel estimation are covered. In addition, other important system impairments such as phase noise and carrier frequency offset are covered. A combined frame and frequency synchronization is proposed using only the short training sequence of IEEE 802.11a.

Chapter IV emphasizes channel coding techniques and some forms of frequency and space diversity. In particular, discussions of block interleavers and convolutional codes with both hard and soft decision Viterbi decoding are provided. An introduction to space diversity and the two most popular receiver diversity techniques is also presented in this chapter. Several operational modes of the IEEE 802.11a physical specification are evaluated under AWGN and multipath fading.

Chapter V summarizes this thesis research and offers a road map for future research.

Finally, Appendix A discusses the physical mechanisms leading to small-scale multipath fading under narrow-band conditions.

THIS PAGE INTENTIONALLY LEFT BLANK

II. BACKGROUND

Multipath fading is widely recognized as a major impairment for wireless communications. The distortions caused by multipath can be represented by a channel-model waveform. The channel model and its parameters should be selected in a way that is fair to all proposals, independent of data rate and bandwidth. Moreover, the channel model should reflect realistic radio conditions, e.g., including noise.

This chapter discusses these performance criteria and selects the exponential channel model from the IEEE 802.11 Task Group *b* to simulate multipath fading. In order to have consistent use of the model, the model is truncated to a finite length and normalized in the expected value sense. In addition to the exponential channel model, a Rayleigh fading model is added. A brief discussion of OFDM transmission is also provided, explaining why OFDM technology is the highway to achieving high-speed wireless communications.

Finally, this chapter ends with an overview of the IEEE 802.11a standard, the WLAN that was used as a test-bed for our simulations.

A. MULTIPATH FADING

In mobile wireless communications, the information signals are distorted by reflection, diffraction and scattering when signals interact with obstacles and terrain conditions, as shown at the top of Figure 1. Hence, the received signal has a different appearance from the transmitted signal. The distortions experienced by the communication signals include attenuation in signal strength, delay spread, and frequency broadening [1].

As illustrated at the bottom of Figure 1, these distortions can be represented by a single-channel model. This channel model is then used to simulate the distortions encountered in similar wireless environments. In this simple example, the received signal can be modeled as three combined signals arriving at different times and with different amplitudes.

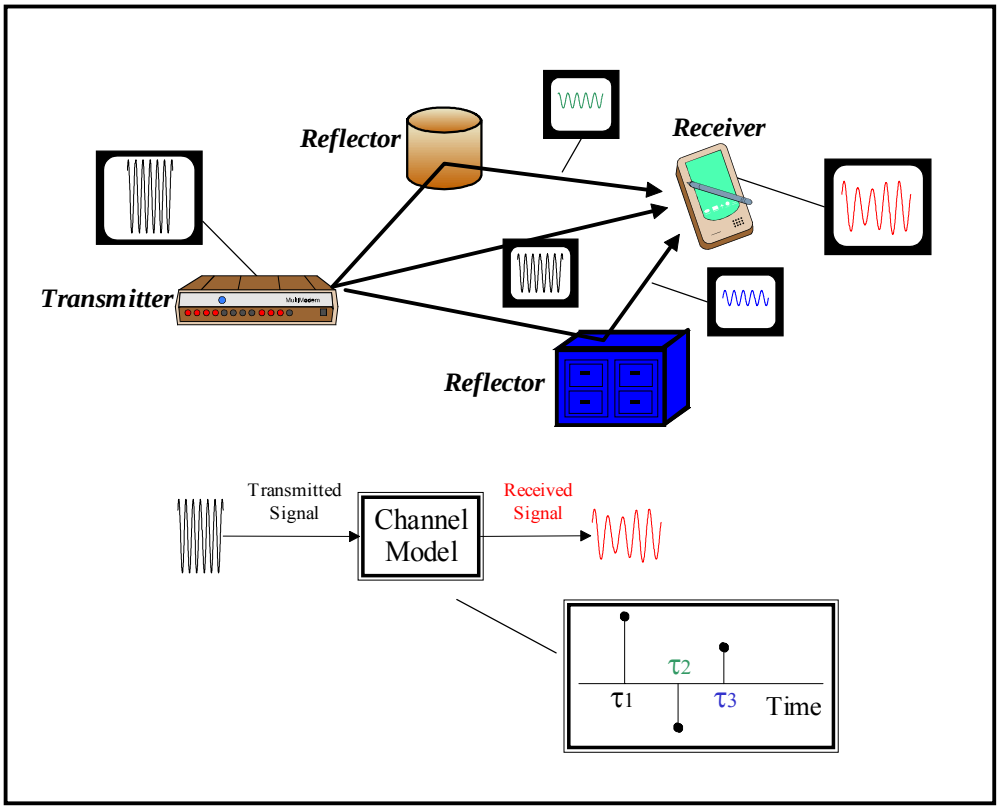

Figure 1. Multipath Interference

The delay and amplitude of each path is largely a function of the length of the path; however, other factors such as how much of the signal is absorbed by the reflector and movement of the reflector also impact the delay and amplitude of a given signal path.

The unpredictable nature of the time variations in the channel may be described by narrowband random processes [2]. For a large number of signal reflections impinging at the receiver, the central limit theorem can be invoked to model the distortions as complex-valued Gaussian random processes.

The envelope of the received signals is comprised of two components, rapidly varying fluctuations superimposed onto slowly varying ones. When a mean envelope suffers a drastic reduction in signal strength resulting from “destructive” combining of the phase terms from the individual paths, the signal is said to be experiencing a fade in signal strength.

1. Attenuation in Signal Strength

The effect of multipath fading on the received signal amplitude is broken into two components, large-scale fading and small-scale fading. A typical channel impulse response (CIR) is shown in Figure 2 for a carrier frequency of 5.2 GHz and a small room environment with a delay spread $\tau_{RMS} = 50$ ns and a relative velocity of $v_r = 1$ m/s.

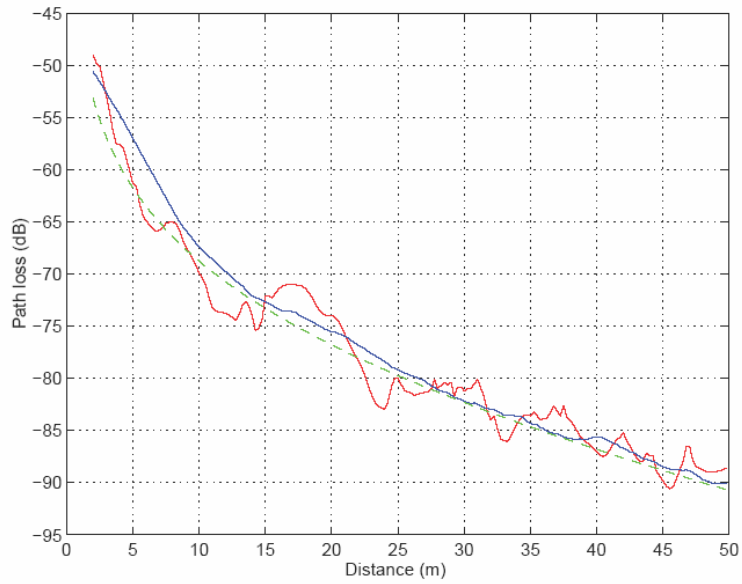

Figure 2. Large and Small-scale Fading (From Ref. [3].)

Large-scale fading represents the average received signal power attenuation or the path loss over the transmitter-to-receiver separation distance *d*. The overall path loss L_p depends on many factors [4]. The impact of *d* on the path loss depends on the path loss coefficient *c* which determines how fast the signal power attenuates as it travels. This relationship is

$$L_p \propto \frac{1}{d^c}. \tag{2.1}$$

The value of the path-loss coefficient depends on the environment and a large number of studies have been performed to determine its value in various cases. The basic case is free space where $c = 2$; in an indoor environment, a value of $c = 3$ can be used [5].

Small-scale fading is used to describe the rapid fluctuation of the amplitude of a radio signal over a short period of time or travel distance. It is caused by interference between two or more versions of the transmitted signal that arrive at the receiver at slightly different times. These waves, called multipath waves, combine at the receiver antenna to give a resultant signal which can vary widely in amplitude and phase, depending on the distribution of the intensity, the relative propagation time of the waves and the bandwidth of the transmitted signal.

2. Time Dispersion

As previously mentioned, the channel can be modeled by a random process. Hence, the state of the channel can be accurately described by its time and frequency autocorrelation functions [6]:

$$R_{hh}(\tau_1,\tau_2;t_1,t_2)=\frac{1}{2}E\left\{h^*(\tau_1;t_1)h(\tau_2;t_2)\right\}, \tag{2.2}$$

$$R_{HH}(f_1,f_2;t_1,t_2)=\frac{1}{2}E\left\{H(f_1;t_1)H^*(f_2;t_2)\right\}, \tag{2.3}$$

where $h(\tau;t)$ is the channel's time varying impulse response, and $H(f;t)$ is the Fourier transform of $h(\tau;t)$ with respect to time difference of arrival τ.

The wide-sense stationary uncorrelated scattering (WSSUS) model [2] makes physical assumptions that are valid for most radio transmission channels :

- The signal variations on paths arriving at different delays are uncorrelated.
- The correlation properties of the channel are stationary.

It can be shown [6] that with this WSSUS model, the autocorrelation function becomes:

$$R_{hh}(\tau_1,\tau_2;\Delta t)=P_h(\tau_1;\Delta t)\delta(\tau_1-t_2), \tag{2.4}$$

where $P_h(\tau_1;\Delta t)$ is the inverse Fourier transform of $R_{HH}(\Delta f;t_1,t_2)$ with respect to Δf :

$$P_h(\tau;\Delta t)=\int_{-\infty}^{\infty}R_{HH}(\Delta f;\Delta t)e^{j2\pi\tau(\Delta f)}d(\Delta f). \tag{2.5}$$

If we let $\Delta t = 0$, the resulting function $P_h(\tau;0) \equiv P_h(\tau)$ is simply the average power output of the channel as a function of the time delay τ. This quantity is called the *multipath intensity profile* or the *power delay spectrum* (PDS) of the channel.

In practice, the PDS of the channel can be measured by transmitting very narrow pulses (or, equivalently, a wideband signal) and cross-correlating the received signal with a conjugate delayed version of itself [7]. Figure 3 compares the measured mean PDS with the theoretical exponential PDS, i.e.,

$$P_h(\tau) = \frac{1}{\sigma_\tau} e^{-\frac{\tau}{\sigma_\tau}}, \tag{2.6}$$

where σ_τ denotes the delay spread. The range of values of τ over which $P_h(\tau)$ is essentially non-zero is called the *multipath spread* of the channel and is denoted by T_m.

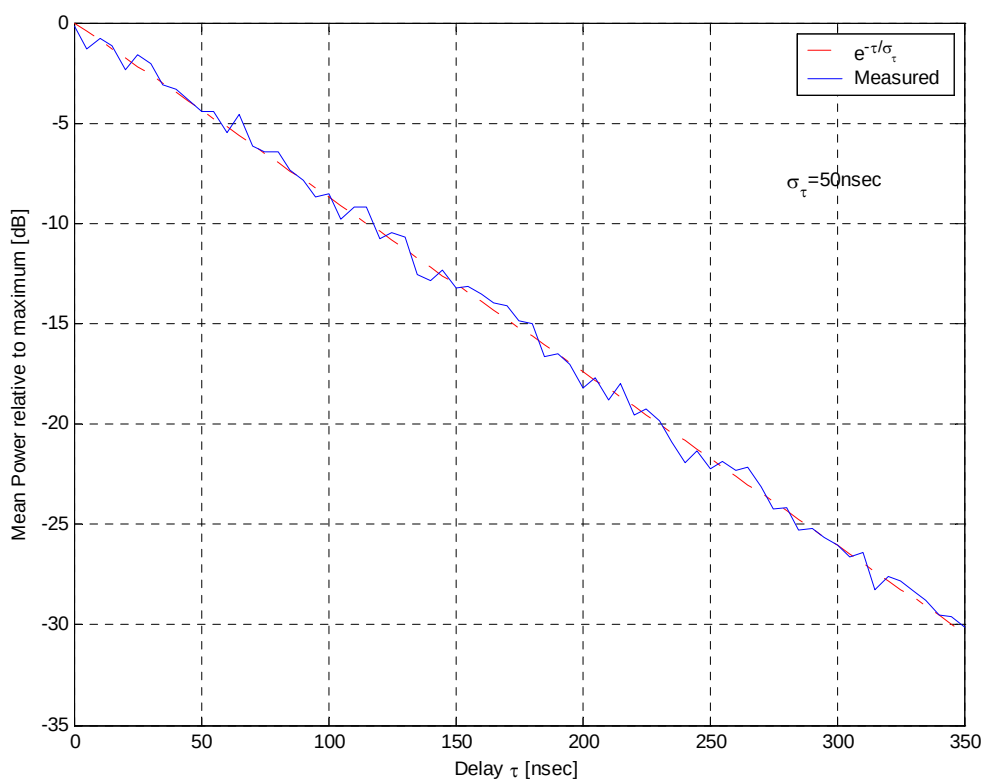

Figure 3. PDS for a Small Room with $\sigma_\tau = 50$ ns (After Ref. [3].)

The spreading of the narrow pulse is measured quantitatively in terms of the standard deviation about the mean excess delay ($\overline{\tau}$) and is termed the *rms delay spread* (σ_τ).

The mean-excess delay is the first moment of the power delay profile and is defined as [5]:

$$\overline{\tau} = \frac{\sum_{\kappa} P(\tau_\kappa)\tau_k}{\sum_{\kappa} P(\tau_\kappa)}. \tag{2.7}$$

The rms delay spread is the square root of the second central moment of the power-delay profile and is defined as:

$$\sigma_\tau = \sqrt{\frac{\sum_{\kappa} P(\tau_\kappa)(\tau_k - \overline{\tau})^2}{\sum_{\kappa} P(\tau_\kappa)}}. \tag{2.8}$$

These delays are measured relative to the first detectable signal arriving at the receiver at $\tau_0 = 0$.

For digital signaling, the time dispersion leads to a form of ISI whereby a given received data sample is corrupted by the responses of neighboring data symbols. The severity of this ISI depends on the degree of multipath induced time dispersion relative to the data symbol period. It is generally agreed that, if the ratio of the rms delay spread to symbol period is greater than about 0.3, then the multipath induced ISI must be corrected if the system's performance is to be acceptable [8]. Typical values of the rms delay spread are on the order of microseconds in outdoor mobile radio channels and on the order of nanoseconds in indoor radio channels.

The amount of σ_τ depends on the type of the environment, as shown in Table 1.

Environment	RMS Delay Spread
Home	< 50 nsec
Office	~ 100 nsec
Factory	200-300 nsec

Table 1. Typical RMS Delay Spread for Indoor Environments (After Ref. [8].)

More spreading of the signal occurs in highly cluttered areas. Surfaces of furniture, elevator shafts, walls, factory machinery, and metal buildings all contribute to the amount of delay spread in a given environment.

3. Frequency Broadening

Time variations of the radio channel caused by angular spread and motion make the transfer function of the channel change from instant to instant, resulting in output frequencies different from input frequencies. The radio channel behaves much like a time-varying linear filter whose transfer function at any time describes the frequency response of the channel [7]. This is the Doppler spreading caused by the mobile channel. The physical mechanisms leading to small-scale fading and Doppler spreading are discussed in Appendix A.

The amount of spectral broadening depends on Doppler shift f_D, which is defined as [5]:

$$f_D = \frac{v_r \cos(\phi)}{\lambda} = \frac{v_r f_c}{c} \cos(\phi), \tag{2.9}$$

where ϕ is a random phase angle uniformly distributed from 0 to 2π, v_r is the relative velocity and f_c is the carrier frequency.

For example, at 5.2 GHz, and a mobile speed of 1 m/s (walking speed), the maximum Doppler shift is 17.33 Hz.

4. Characterization of Small Fading

The time variations of the channel are quantified in terms of the channel coherence time [5], which is roughly equal to the reciprocal of the maximum Doppler shift. The frequency variations of the channel are quantified in terms of the channel coherence bandwidth.

Depending on the relation between the signal parameters and channel parameters, different transmitted signals will experience different types of fading, as illustrated in Table 2.

Small-Scale Fading (based on multipath delay spread)	
Frequency Non-selective (Flat) Fading	***Frequency Selective Fading***
1. BW of Signal < Coherence BW of Channel 2. Delay Spread < Symbol Period	1. BW of Signal > Coherence BW of Channel 2. Delay Spread > Symbol Period

Small-Scale Fading (based on Doppler spread)	
Fast Fading	***Slow Fading***
1. High Doppler Spread 2. Coherence Time < Symbol Period 3. Channel Variations Faster than Baseband Signal Variations	1. Low Doppler Spread 2. Coherence Time > Symbol Period 3. Channel Variations Slower than Baseband Signal Variations

Table 2. Types of Small Scale Fading (After Ref. [5].)

Information-bearing signals whose bandwidth is small compared to the coherence bandwidth of the channel experience *frequency nonselective* or *flat* fading. However, if the information-bearing signals have bandwidth greater than the coherence bandwidth of the channel, then the channel is said to be *frequency selective*. Channels whose statistics remain fairly constant over several symbol intervals are considered *slow fading* in contrast to channels whose statistics change rapidly during a symbol interval. Such channels are considered *fast fading*. In general, indoor wireless channels are well characterized by frequency-selective, slow-fading channels [9].

B. CHANNEL MODEL

In this section, we discuss a model to predict the effects of multipath on the transmitted communication signal. First we show that the channel's impulse response can be modeled as a FIR filter with taps being independent complex Gaussian variables. We then discuss the exponential channel model developed by IEEE 802.11 Task Group b. This is the channel model used in this thesis for the various simulations.

1. Impulse Response of the Time Varying Channel

Let the transmitted signal be represented in general as:

$$s(t) = \mathrm{Re}\left[s_l(t) e^{j2\pi f_c t} \right], \tag{2.10}$$

where $s_l(t)$ denotes the equivalent lowpass transmitted signal.

We assume that there are multiple paths. Associated with each path is a propagation delay and an attenuation factor. Both the propagation delays and the attenuation factors are time variant as a result of changes in the structure of the medium. Consequently, the received bandpass signal may be expressed in the form [7]:

$$r(t) = \sum_n \alpha_n(t) s\left[t - \tau_n(t)\right], \tag{2.11}$$

where $\alpha_n(t)$ is the attenuation factor for the signal received on the *n*th path and $\tau_n(t)$ is the propagation delay for the *n*th path. Substitution for $s(t)$ from Equation (2.10) into Equation (2.11) yields the result:

$$r(t) = \mathrm{Re}\left(\left\{ \sum_n \alpha_n(t) e^{-j2\pi f_c \tau_n(t)} s_l\left[t - \tau_n(t)\right] \right\} e^{j2\pi f_c t} \right). \tag{2.12}$$

It is apparent from Equation (2.12) that the equivalent lowpass received signal is

$$r_l(t) = \sum_n \alpha_n(t) e^{-j2\pi f_c \tau_n(t)} s_l\left[t - \tau_n(t)\right]. \tag{2.13}$$

Since $r_l(t)$ is the response of an equivalent lowpass channel to the equivalent lowpass signal $s_l(t)$, it follows that the equivalent lowpass channel is described by the time-variant impulse response,

$$h(\tau;t) = \sum_n \alpha_n(t) e^{-j2\pi f_c \tau_n(t)} \delta\left[t - \tau_n(t)\right], \tag{2.14}$$

where $h(\tau;t)$ is the response of the channel at time *t* due to an impulse applied at time $t - \tau_n(t)$, $\alpha_n(t)$ is the attenuation factor for the signal received on the *n*th path and $\tau_n(t)$ is the propagation delay for the *n*-th path.

Wireless LAN applications generally assume that the channel is "quasi-stationary", i.e., the channel's properties do not change over the duration of the data

packet. Under this assumption, the time dependency in Equation (2.14) can be dropped to yield

$$h(\tau) = \sum_n \alpha_n e^{-j2\pi f_c \tau_n} \delta(\tau - \tau_n). \tag{2.15}$$

When there are a large number of paths, the central limit theorem can be applied. That is, $r_l(t)$ may be modeled as a complex-valued Gaussian random process. This means that the time variant impulse response is a complex-valued Gaussian random process in the *t* variable.

When the impulse response is modeled as a zero-mean complex-valued Gaussian process, the envelope $|h(\tau;t)|$ at any instant *t* is Rayleigh distributed [10]. In this case, the channel is said to be a *Rayleigh fading channel*. The probability density function for a Rayleigh fading channel is given by

$$p_R(r) = \frac{r}{\sigma^2} e^{-\frac{r^2}{2\sigma^2}} \qquad r \geq 0, \tag{2.16}$$

where $2\sigma^2$ represents the received diffuse signal power.

In the event that there are fixed scatterers and a line of sight (LOS) path to the receiver, in addition to randomly moving scatterers, the envelope of $h(\tau;t)$ has a Rice distribution whose density is given by [10]

$$p_R(r) = \frac{r}{\sigma^2} e^{-\frac{r^2+\zeta^2}{2\sigma^2}} I_o\left(\frac{r\zeta}{\sigma^2}\right) \qquad r > 0, \tag{2.17}$$

where $I_o(\cdot)$ is the modified Bessel function of the zeroth kind and ζ is the mean due to the fixed scatterers or LOS path. In this case, the channel is said to be a *Rician fading channel*.

2. Exponential Channel Model (IEEE 802.11)

In an environment where the performance measurement of the same radio is used in the same location, the results may not agree over time. A consistent channel model is required to compare different WLAN systems.

The literature describes a plethora of channel models; however, the 802.11 task group b chose the exponential channel model because it is easy to generate, and it is a reasonably accurate model of the real world [8]. This model provides a good compromise between simplicity and reality. In doing so, the exponential channel model is ideal for software simulations to predict the performance of a given WLAN implementation.

The taps in this model are complex zero-mean Gaussian random variables with average power profile that decays exponentially (hence the name *exponential channel model*.).

Theoretically, an infinite number of taps exist in the exponential model; however, the magnitude of the taps decays rapidly. Therefore, truncating the taps at some point is reasonable. This point is determined by the sampling frequency f_s and the rms delay spread τ_{rms}. In other words, the channel can be represented by a finite impulse response (FIR) model.

A mathematical expression of this model is [11]

$$h_k = N(0, \frac{1}{2}\sigma_k^2) + j \cdot N(0, \frac{1}{2}\sigma_k^2) \quad \text{for } k = 0,1,...,k_{\max}, \tag{2.18}$$

where

$$\begin{aligned} k_{\max} &= \lceil 10 \cdot f_s \cdot \tau_{rms} \rceil, \\ \beta &\approx e^{-\frac{1}{f_s \cdot \tau_{rms}}}, \\ \sigma_0^2 &= \frac{1-\beta}{1-\beta^{k_{\max}+1}}, \\ \sigma_k^2 &= \sigma_0^2 \beta^k, \text{ and,} \\ j &= \sqrt{-1}\ . \end{aligned} \tag{2.19}$$

The parameters are the sampling frequency f_s and the rms delay spread τ_{rms}. The normalization factor σ_0 ensures that the sum of the average power profile is one. This model is shown in Figure 4. It should be noted that the sampling period $T_s = 1/f_s$ is equal to the gap between the taps.

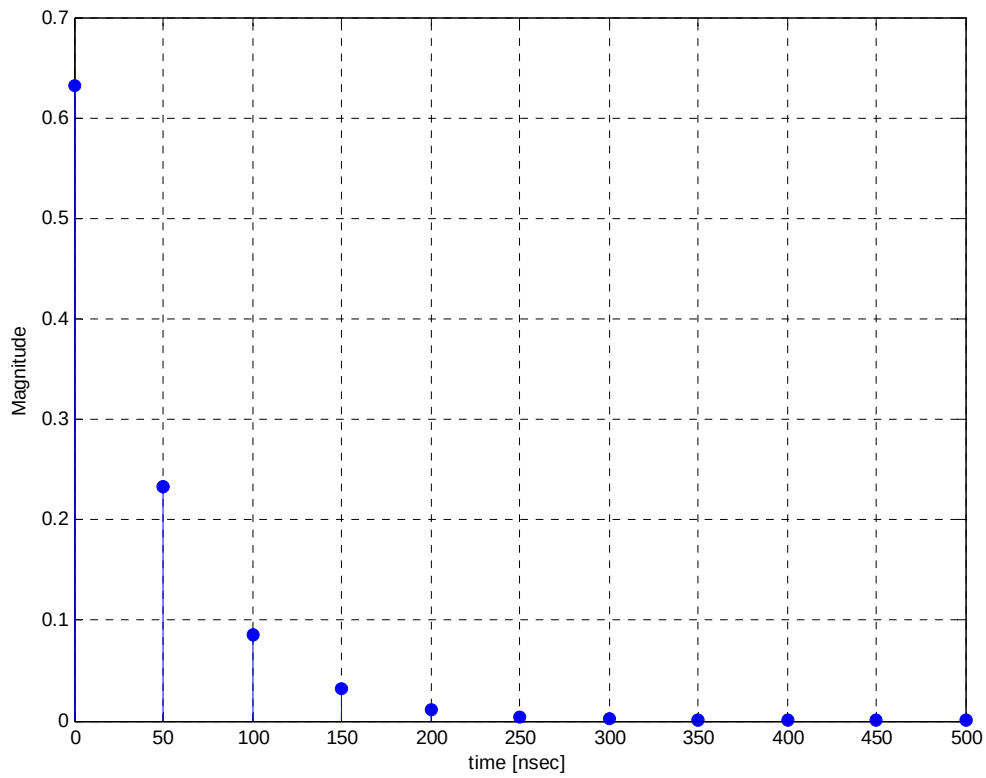

Figure 4. Average Power Profile for $\tau_{rms} = 50$ ns, $f_s = 20$ MHz

In the 802.11b channel model, the taps are truncated to $k_{\max}$ [11]. This is an appropriate truncation for our purposes; since the exponential channel is decaying monotonically, if the last tap is small, then we know that the channel is sufficiently long.

Indeed, the value of the last tap in the truncated exponential channel is

$$e^{-\frac{k_{\max}}{f_s \cdot \tau_{rms}}} = e^{-10} \approx 4.5 \times 10^{-5}. \tag{2.20}$$

This is a reasonably small number. Thus we conclude that truncating at $k_{\max}$ has not significantly altered our exponential channel model.

An actual realization of the exponential channel profile will look quite different from the averaged model, as shown in Figure 5. We point out that in this sample realization, the largest path actually occurs at a delay of two sampling periods rather than at a delay of zero.

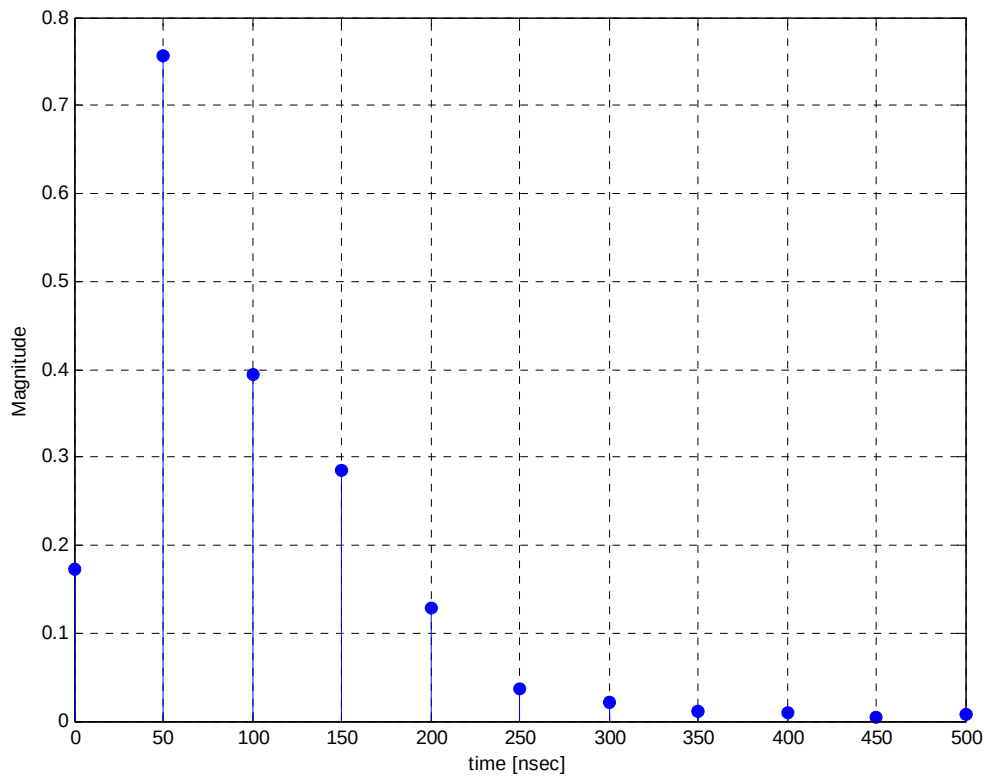

Figure 5. Sample Realization for $\tau_{rms} = 50$ ns, $f_s = 20$ MHz

The existing exponential channel model is normalized in the expected-value sense [11]:

$$E\left\{\sum_{k=0}^{k_{\max}} |h_k|^2\right\} = \sum_{k=0}^{k_{\max}} \sigma_k^2 = \sigma_0^2 \sum_{k=0}^{k_{\max}} e^{-\frac{k}{f_s \cdot \tau_{rms}}} = \sigma_o^2 \frac{1-e^{-\frac{k_{\max}+1}{f_s \cdot \tau_{rms}}}}{1-e^{-\frac{1}{f_s \cdot \tau_{rms}}}}$$
$$\Rightarrow \sigma_o^2 = \frac{1-e^{-\frac{1}{f_s \cdot \tau_{rms}}}}{1-e^{-\frac{k_{\max}+1}{f_s \cdot \tau_{rms}}}} = \frac{1-\beta}{1-\beta^{k_{\max}+1}}. \tag{2.21}$$

In other words, individual realizations do not necessarily have a power gain of 0 dB, but when taken over the ensemble of realizations, the average power gain is 0 dB.

This expected-value normalization is due to the selection of the parameter σ_0^2. It must be emphasized that this is not the same as generating the channel model and forcing each realization to have an average power gain of 0 dB. Consequently, this exponential channel model includes both inter-symbol interference and flat fading [12].

A simplified block diagram of a multipath wireless channel simulation using the exponential channel model is illustrated in Figure 6.

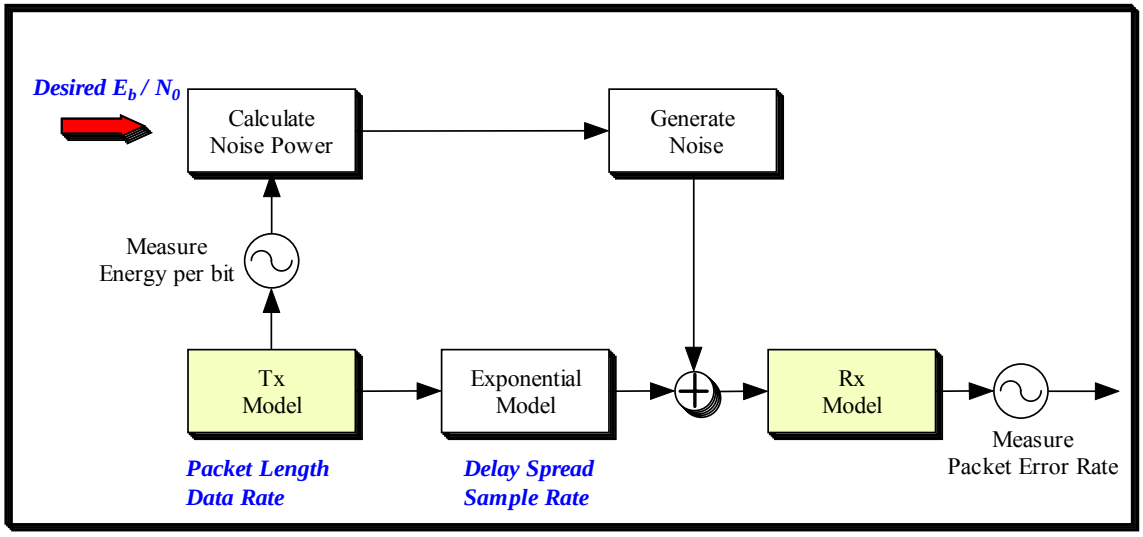

Figure 6. Block Diagram of Flat Fading & ISI (After Ref. [12].)

The items in blue italics are the inputs to the test procedure. The output of the test procedure is the observed packet error rate.

For practical implementation, the energy per bit does not need to be measured for each simulation run but rather can be derived theoretically. The purpose of the measurement in this block diagram was to show at what point in the system the energy should be measured.

All simulation results should include the inputs and packet error rate.

3. Rayleigh Fading

When the relative power delay is much less than the sample rate, the receiver cannot resolve or does not see the individual paths. A common channel model for this scenario is the classic channel model of Rayleigh Fading. This is realistic for wireless LANs and should be addressed in evaluating the performance [7].

The Rayleigh fading model assumes that there is no direct line of sight between the transmitter and receiver. The amplitude of the received signal is a Rayleigh distributed random variable, while the phase is uniformly distributed between $[0, 2\pi]$. Another

important characteristic of this model is that a Rayleigh channel is memoryless, i.e., all frequencies are affected the same (frequency non-selective fading).

To simplify the simulation procedure, the Rayleigh fading case can be seen as a limiting case of the exponential channel model, where $k_{\max}$ is fixed to 1 and the rms delay spread is fixed to zero [12]. Essentially, the variance of the noise used to generate is fixed at 1/2 for the real and imaginary component:

$$h_{Rayleigh} = h_0 = N(0, \frac{1}{2}\sigma_0^2) + j \cdot N(0, \frac{1}{2}\sigma_0^2), \tag{2.22}$$

where $\sigma_0^2 = 1$. This results in a single tap channel model or multiplication of the signal by the value of the type.

Additive White Gaussian Noise (AWGN) was also included in multipath simulations to reflect more realistic conditions.

C. OFDM OVERVIEW

In a traditional serial communication system, data are sent as a serial pulse train of information symbols. During the sequence of transmission of each symbol through the channel, the symbol frequency spectrum is allowed to occupy the entire available bandwidth. However, in a multipath environment the signal envelope fluctuates. The time dispersion nature of the multipath channel also causes adjacent symbols of the serial stream to interfere when the symbols are short compared to the rms delay spread, causing ISI and degrading system performance [5]. From the frequency domain point of view, the indoor wireless environment is characterized by the enhancement of some frequencies and the attenuation of others (frequency selective fade).

Using adaptive equalization techniques at the receiver is one way to equalize the received signal [13]. However, in practice, achieving this equalization at several megabits per second with compact and low-cost hardware is quite difficult.

1. Concept of Parallel Data Transmission

A typical impulse response of a frequency-selective channel in the time and frequency domains was depicted at the top of Figure 7.

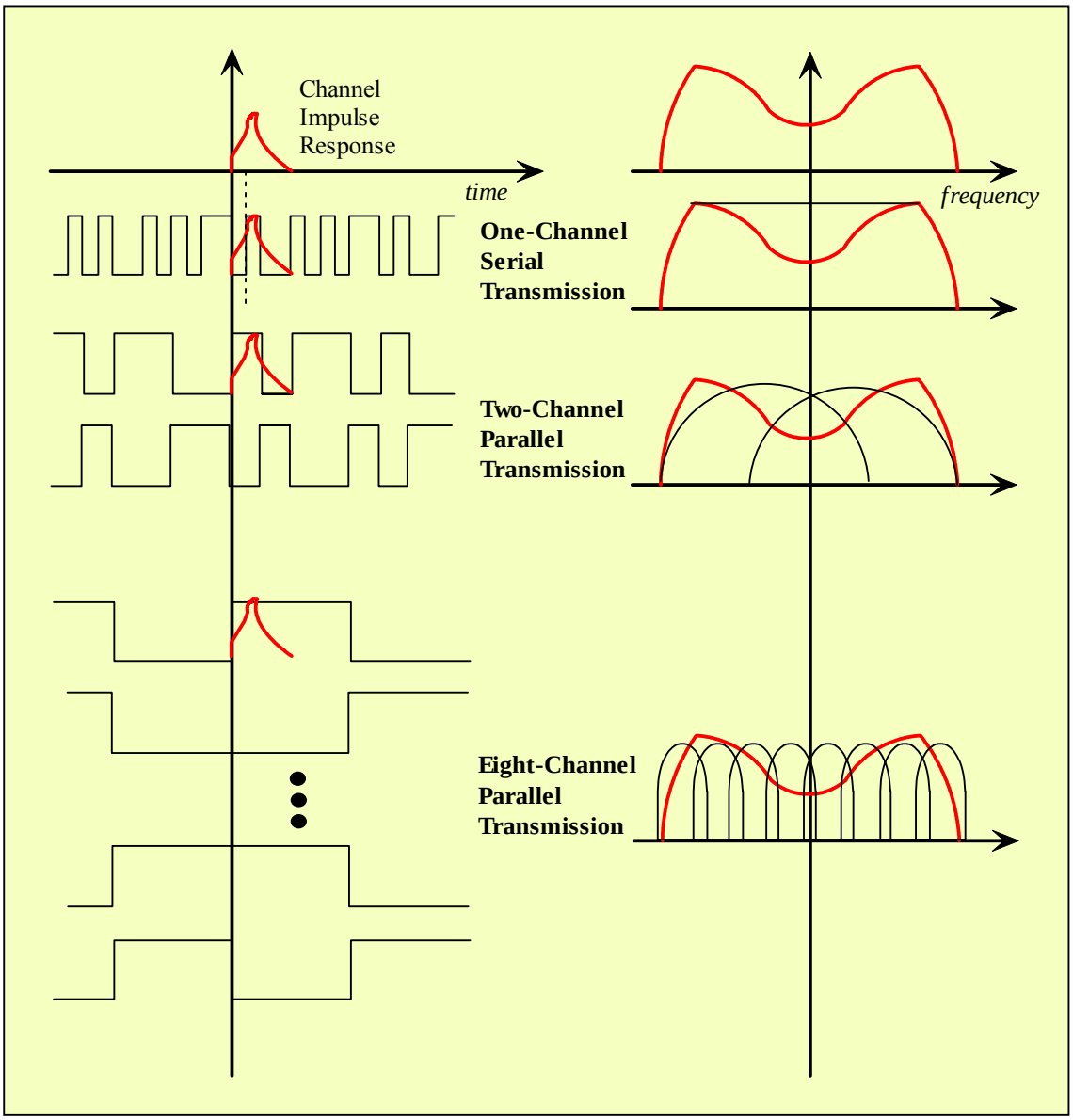

Figure 7. Channel Impulse Response in Time and Frequency Domain (After Ref. [14].)

The time waveform and frequency spectrum of one-channel serial data transmission were also illustrated. The delay spread of the channel is longer than one symbol period. As a result, both the waveform and the frequency spectrum are distorted. One way to equalize the distorted signal is by using adaptive equalization techniques that estimate

the channel impulse response and then multiplying the complex conjugate of the estimated impulse response by the received data signal at the receiver [13]. However, practical difficulties are associated with operating this equalization at high bit rates: several successive symbols must be stored to equalize the received data sequentially. Furthermore, the complexity of the equalizer grows with the square of the number of channel taps. We therefore look for other solutions.

Another way to combat the problems caused by the multipath fading environment and achieve broadband communications is by using parallel transmission [14]. In this technique, the transmitted high speed data is converted to slow parallel data in several subcarriers. These data are multiplexed using any of several multiplexing techniques to distinguish between the subcarriers.

The effect of the parallel transmission scheme is also illustrated in Figure 7, using two-channel and eight-channel data transmittion. Increasing the number of parallel transmission channels for a given overall data rate, the symbol period of each subcarrier is lengthened. Hence, the delay spread of the channel becomes shorter than one symbol period and the effect of ISI is minimized. From the frequency domain point of view, the multipath channel becomes flat over each subcarrier.

The approach to implementing a parallel communications system is done in different ways. In a classical parallel data system using conventional FDM technology (Figure 8), the total signal frequency bandwidth is partitioned into *N* non-overlapping sub-channels and are frequency division multiplexed for transmission.

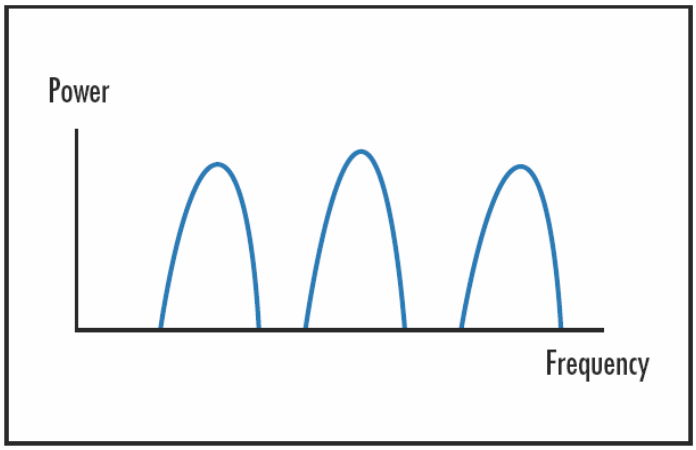

Figure 8. FDM with Subbands

At the receiving end, separation of the sub-channels is traditionally accomplished by a bank of bandpass filters. However, due to the roll-off effect of physically realizable filters, the actual bandwidth of each subchannel must be further widened. Sufficient guard-bands must be inserted in the frequency spectrum between adjacent sub-channels to permit effective filtering without in-band signal attenuation and adjacent band signal interference. Intuitively, this method does not offer the best possible spectrum efficiency since now the overall bandwidth is lengthened by multiple guard-bands that do not carry any useful information [15].

2. Orthogonal Frequency Division Multiplexing (OFDM)

OFDM can be thought of as a hybrid of multicarrier modulation (MCM) and frequency shift keying (FSK) modulation. MCM transmits data by dividing the stream into several parallel bit streams and modulating each of these data streams onto individual carriers or subcarriers. FSK modulation is a technique in which data are transmitted on one carrier from a set of orthogonal carriers in each symbol duration. To achieve orthogonality among the carriers, the frequency spacing between adjacent carriers must be an integer multiple of the inverse of the symbol duration. Figure 9 shows the frequency response of five orthogonal carriers 312.5 kHz apart.

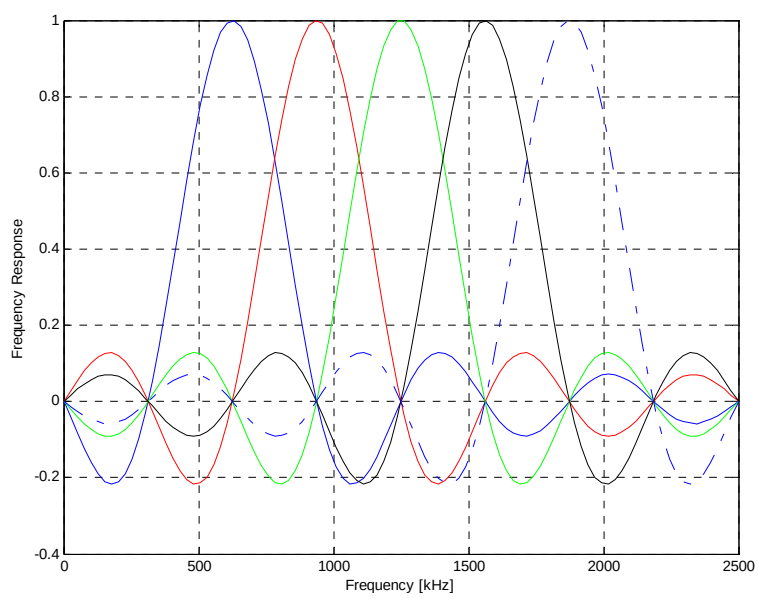

Figure 9. Overlapping Orthogonal Carriers

To avoid Inter-carrier interference (ICI) during detection, the spectral peak of each carrier must coincide with the zero crossing of all the other carriers. Hence, the difference between the center lobe and the first zero crossing represents the minimum required spacing and is equal to $1/T$ [16].

With OFDM, all the orthogonal subcarriers are transmitted simultaneously. In other words, the entire allocated bandwidth is occupied by the narrow orthogonal subcarriers. By transmitting several symbols in parallel, the symbol duration is lengthened, which reduces the effects of ISI caused by the dispersive multipath fading environment[17].

A simplified block diagram of OFDM is depicted in Figure 10.

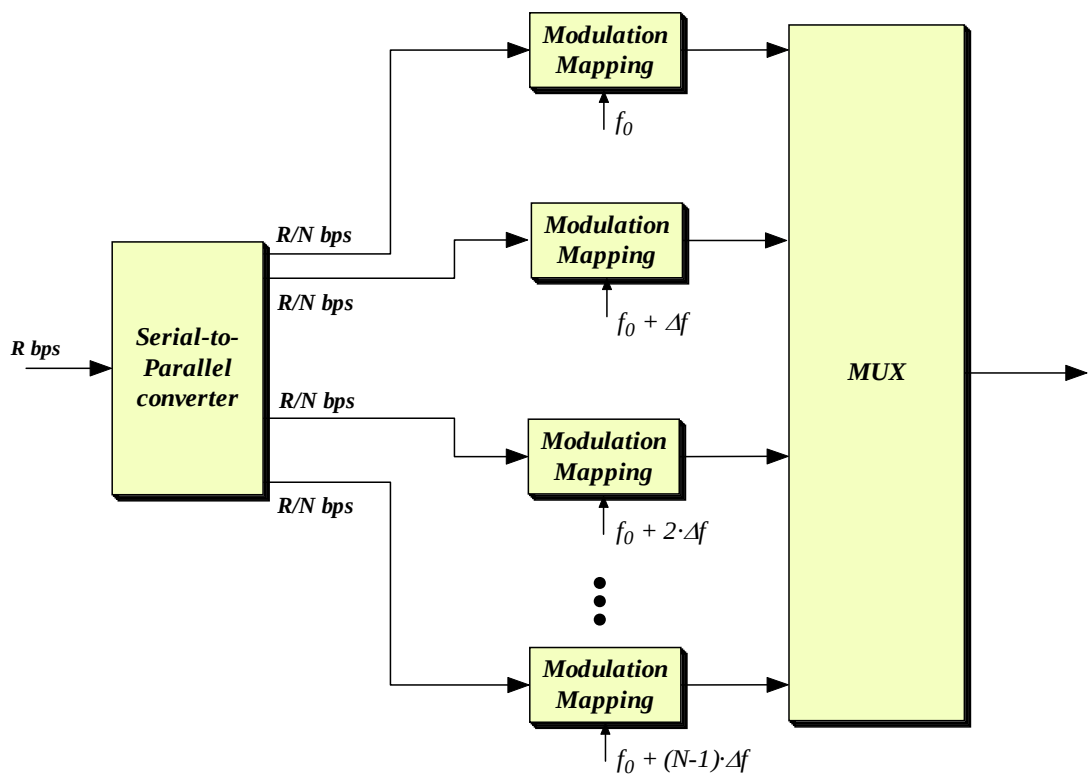

Figure 10. Orthogonal Frequency Division Multiplexing

The data stream operating at R bps is split into N substreams using a serial-to-parallel converter. Each substream has a data rate of R/N bps and is transmitted on a separate subcarrier, with a frequency spacing between adjacent subcarriers of Δf. The symbol period of each subcarrier is the inverse of the data rate, i.e.,. $T_s = N/R$.

The frequency spacing is determined by the available bandwidth *BW* as follows:

$$\Delta f = \frac{BW}{N}, \tag{2.23}$$

where *N* is the number of subcarriers and $\Delta f = i \cdot R/N = i/T_s$, $(i = 1, 2, 3, ...)$ must be an integer multiple of the bit rate of the subcarriers.

a. OFDM Implementation

An OFDM signal is constructed by assigning parallel bit streams to *N* sub-carriers, normalizing the signal energy, and extending the bit duration [9], i.e.,

$$s_{OFDM}(n) = \frac{A}{N}\sum_{i=0}^{N-1} x_i(n) \cdot e^{2\pi f_i n} \quad \text{for} \quad 0 \le n \le N, \tag{2.24}$$

where $s_{OFDM}(n)$ denotes the *n*-th bit of the resulted OFDM symbol and $x_i(n)$ is the *n*-th bit of the *i*-th data stream.

The Discrete Fourier Transform (DFT) and Inverse Discrete Fourier Transform (IDFT) are defined respectively as [18]:

$$\begin{aligned} X(k) &= \sum_{n=0}^{N-1} x(n) \cdot e^{-j2\pi kn/N} \\ x(n) &= \frac{1}{N}\sum_{k=0}^{N-1} X(k) \cdot e^{j2\pi kn/N}. \end{aligned} \tag{2.25}$$

It is clear that $s_{OFDM}(n)$ is merely the IDFT of $x_i(n)$ scaled by *A*. Thus, multiplexing (MUX) the subcarriers can be accomplished by using the Inverse Discrete Fourier Transform (IDFT) .The common way to implement the IDFT is by an inverse Fast Fourier Transform (IFFT) algorithm [19].

b. Cyclic Prefix

The orthogonality of subcarriers in OFDM can be maintained, and individual sub-channels can be completely separated by using the FFT circuit at the receiver when there are no ISI and ICI introduced by transmission channel distortion [14]. In practice, however, these conditions cannot be obtained. Because the spectra of an OFDM sig-

nal are not strictly bandlimited, the distortion, due to multipath fading, causes each subcarrier to spread the power into the adjacent subcarriers. To reduce the distortion, a simple solution is to increase the symbol duration or the number of carriers. However, this method may be difficult to implement in terms of carrier stability against Doppler frequency and FFT size.

One way to eliminate ISI is to create a cyclically extended guard interval (GI), where each OFDM symbol is preceded by a periodic extension of the signal itself [16]. The total symbol duration is

$$T_{total} = T_{gi} + T_s \ , \tag{2.26}$$

where T_{gi} is the guard interval. Figure 11 illustrates the concept of cyclic prefix.

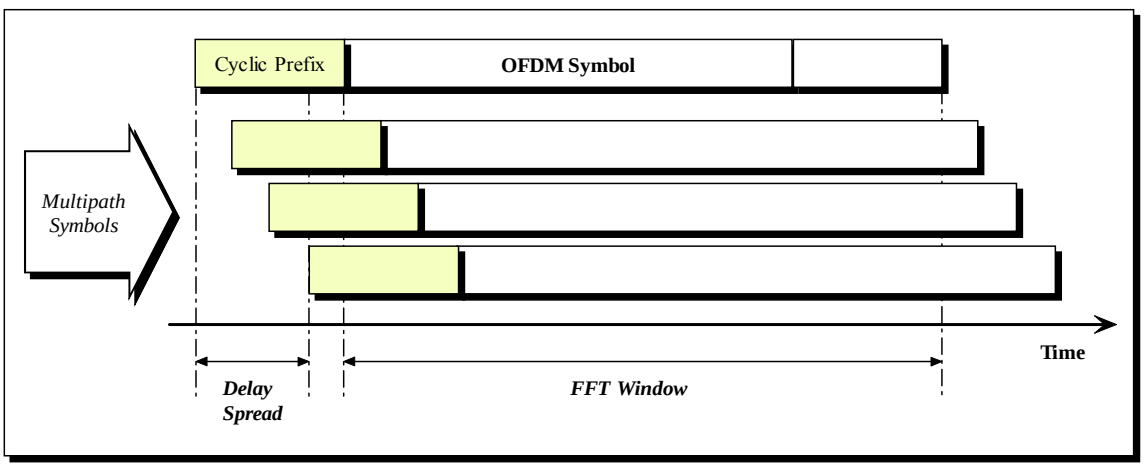

Figure 11. Cyclic Prefix (CP) in OFDM Symbol

Each symbol is made of two parts. The whole signal is also repeated at the start of the symbol and is called the *guard interval* or *cyclic prefix*. When the cyclic prefix is longer than the channel impulse response, or the multipath delay spread, the effect of ISI can be eliminated. However, the ICI still exists.

The length of the guard interval is application dependent. For instance, lower-order modulation techniques are more robust to ISI and ICI. As far as the OFDM system designer is concerned because the insertion of a cyclic prefix will reduce the data throughput, T_{gi} is usually selected to be one-fourth of the OFDM symbol period [19].

The received signal using vector notation is, $\mathbf{r}(n)$, given by

$$\mathbf{r}(n) = \mathbf{s}(n) \otimes \mathbf{h}(n) + \mathbf{w}(n), \tag{2.27}$$

where $\otimes$ denotes convolution, **h** is the channel impulse response vector, and **w** is the additive noise vector.

Because of the addition of the cyclic prefix, a portion of the transmitted signal becomes periodic with period N

$$s(n-m) = s(N+n-m) \quad \text{for} \quad n-m \le p, \tag{2.28}$$

where p is the length of the CP. If p is longer than the delay spread of the channel, the linear convolution in Equation (2.27) becomes a circular one [18]. Hence, in frequency domain, the baseband received signal is

$$\mathbf{R}(k) = \mathbf{S}(k) \cdot \mathbf{H}(k) + \mathbf{V}(k), \tag{2.29}$$

where **R, S** and **H** are the discrete Fourier transforms of **r, s** and **h,** respectively.

D. IEEE 802.11a OVERVIEW

The IEEE 802.11a is an Orthogonal Frequency Division Multiplexing (OFDM) system very similar to the Asymmetrical Digital Subscriber Loop (ADSL) Discrete Multi Tone (DMT) modems sending several subcarriers in parallel using the Inverse Fast Fourier Transform (IFFT) and receiving those subcarriers using the Fast Fourier Transform (FFT). In the IEEE 802.11a standard, the transmission medium is wireless and the operating frequency band is 5 GHz [19].

1. Specifications

The OFDM of the IEEE 802.11a standard system provides a Wireless LAN with data payload communication capabilities of 6, 9, 12, 18, 24, 36, 48 and 54 Mbps. The support of transmitting and receiving at data rates of 6, 12, and 24 Mbps is mandatory in the standard. Lists of key parameters for the system are shown in Table 3 and Table 4.

Data rate (Mbits/s)	Modulation	Coding rate (R)	Coded bits per subcarrier (N_{BPSC})	Coded bits per OFDM symbol (N_{CBPS})	Data bits per OFDM symbol (N_{DBPS})
6	BPSK	1/2	1	48	24
9	BPSK	3/4	1	48	36
12	QPSK	1/2	2	96	48
18	QPSK	3/4	2	96	72
24	16-QAM	1/2	4	192	96
36	16-QAM	3/4	4	192	144
48	64-QAM	2/3	6	288	192
54	64-QAM	3/4	6	288	216

Table 3. Rate-dependent Parameters of IEEE 802.11a (From Ref. [19].)

Parameter	Value
N_{SD}: Number of data subcarriers	48
N_{SP}: Number of pilot subcarriers	4
N_{ST}: Number of subcarriers, total	52 ($N_{SD} + N_{SP}$)
Δ_F: Subcarrier frequency spacing	0.3125 MHz (=20 MHz/64)
T_{FFT}: IFFT/FFT period	3.2 μs ($1/\Delta_F$)
$T_{PREAMBLE}$: PLCP preamble duration	16 μs ($T_{SHORT} + T_{LONG}$)
T_{SIGNAL}: Duration of the SIGNAL BPSK-OFDM symbol	4.0 μs ($T_{GI} + T_{FFT}$)
T_{GI}: GI duration	0.8 μs ($T_{FFT}/4$)
T_{GI2}: Training symbol GI duration	1.6 μs ($T_{FFT}/2$)
T_{SYM}: Symbol interval	4 μs ($T_{GI} + T_{FFT}$)
T_{SHORT}: Short training sequence duration	8 μs ($10 \times T_{FFT}/4$)
T_{LONG}: Long training sequence duration	8 μs ($T_{GI2} + 2 \times T_{FFT}$)

Table 4. Timing-related Parameters of IEEE 802.11a (From Ref. [19].)

The IEEE 802.11a standard system uses 52 subcarriers that are modulated using binary or quadrature phase-shift keying (BPSK/QPSK), 16 Quadrature Amplitude Modulation (QAM), or 64 QAM. The pilot tones are used at the receiver to estimate any residual phase error. Forward Error Correction (FEC) coding (convolutional coding) is used with a coding rate of 1/2, 2/3, or 3/4.

2. OFDM Physical Layer (PHY) Architecture

The primary purpose of the OFDM PHY is to transmit Media Access Control (MAC) Protocol Data Units (MPDUs) as directed by the 802.11 MAC layer. The OFDM PHY of the IEEE 802.11a standard is divided into two elements:

- The Physical Layer Convergence Protocol (PLCP) and
- The Physical Medium Dependent (PMD) sublayers.

The MAC layer of IEEE 802.11a standard communicates with the PLCP via specific primitives through a PHY service access point. When the MAC layer instructs, the PLCP prepares MPDUs for transmission. The PLCP also delivers incoming frames from the wireless medium to the MAC layer. The PLCP sublayer minimizes the dependence of the MAC layer on the PMD sublayer by mapping MPDU into Protocol Data Unit (PPDU), a frame format suitable for transmission by the PMD. Figure 12 illustrates this process [19].

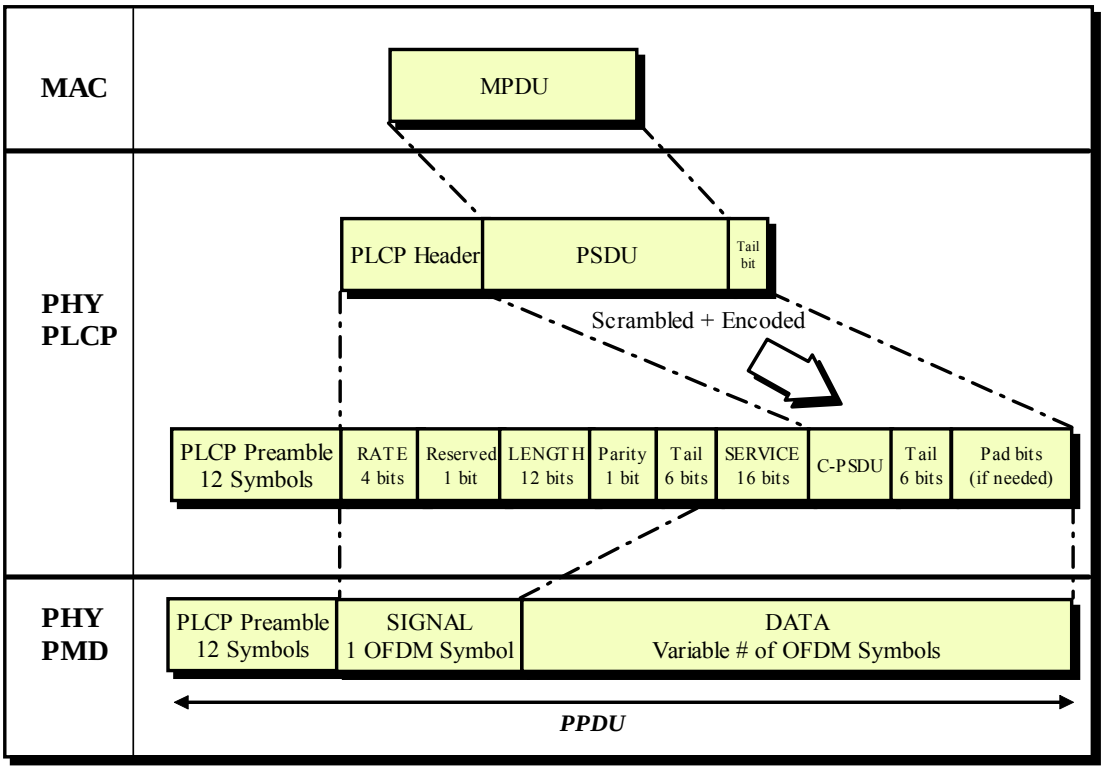

Figure 12. PPDU in IEEE 802.11a (After Ref. [19].)

Once PLCP preamble transmission is started, the PLCP header parameter, SERVICE and PSDU are scrambled and encoded by a convolutional encoder. Tail bits are added to flush the convolutional encoder. If the coded PSDU (C-PSDU) is not multiples of the OFDM symbol, bits are padded to make the C-PSDU length multiples of the OFDM symbol.

The PPDU is unique to the OFDM PHY and it includes [19]:

- PLCP Preamble. This field is used to acquire the incoming OFDM signal and train and synchronize the demodulator. The PLCP preamble consists of 12 symbols, 10 of which are short symbols and 2 long symbols. The short symbols are used to train the receiver's AGC and to estimate a coarse estimate of the carrier frequency and the channel. The long symbols are used to fine-tune the frequency and the channel estimates.
- SIGNAL. This is a 24-bit field, which contains information about the rate and length of the PSDU. The SIGNAL is transmitted using the lowest rate transmission mode to ensure reliable reception. The first 4 bits (R1-R4) are used to encode the rate. The fifth bit (R5) is reserved. The next 12 bits (R6-R17) are used for the length, which indicates the number of bytes in the PHY Service Data Unit (PSDU). The following bit (R18) is a parity check bit. The six tail-bits (R19-R24) are used to flush the convolutional encoder and terminate the code trellis in the decoder.
- DATA. This field contains 16 bits for the service field, the encoded PSDU, 6 tails bits and pad bits (if needed). The data portion of the packet is transmitted at the data rate indicated in the signal field.

Under the direction of the PLCP, the PMD actual transmits and receives the PHY entities between two stations through the wireless medium. To provide this service, the PMD interfaces directly with the air medium and modulates/demodulates the frame transmissions. The PLCP and PMD communicate using service primitives to govern the transmission and reception functions.

3. MAC Layer

The IEEE 802.11a uses the same MAC layer technology as 802.11b: Carrier Sense Multiple Access with Collision Avoidance (CSMA-CA). CSMA-CA is a basic protocol used to avoid signals colliding and canceling each other out. It works by requesting authorization to transmit for a specific amount of time prior to sending information. The sending device broadcasts a request to send (RTS) frame with information on the length of the signal. If the receiving device permits at that moment, it broadcasts a clear-to-send (CTS) frame. Once the CTS goes out, the sending machine transmits its information. Any other sending devices in the area that "hear" the CTS realize another device will be transmitting and allow that signal to go out uncontested [8].

E. SUMMARY

In this chapter, the very important issue of multipath fading in indoor wireless communications was addressed. The signal distortions and time dispersion caused by multipath fading can be accurately described by a channel model. The exponential channel waveform used by IEEE 802.11 Task Group *b* was selected to be the channel model in this thesis. Rayleigh fading and Additive White Gaussian Noise were also incorporated into the channel model options in order to reflect more realistic radio conditions.

The concept of orthogonal frequency division multiplexing (OFDM) was also described. The orthogonal nature of the OFDM sub-channels allows them to be overlapped, thereby increasing the spectral efficiency. We explained how OFDM eliminates ISI, a serious impairment in high-speed applications. Inter-carrier Interference (ICI) is mitigated by adding a cyclic prefix in the OFDM symbol. Finally, a brief overview of the IEEE 802.11a standard was provided.

Since OFDM is a frequency division multiplexing technique, it is essential to have accurate estimates of the frequency offset, caused by oscillator instability, at the receiver. The next chapter describes the very important issue of synchronization.

III. SYNCHRONIZATION

Synchronization is an essential task for any digital communication system for, without accurate synchronization algorithms, it is impossible to recover the transmitted data. Unlike broadcasting systems, WLAN systems typically have to use so called *single-shot* synchronization, i.e., the synchronization must be acquired during a very short time after the start of the packet [19]. This requirement comes from the packet-switched nature of WLAN systems and also from the high data rates used. To facilitate the single-shot synchronization, current WLAN standards include a preamble at the start of the packet. The length and the contents of the preamble have been carefully designed to provide enough information for a good synchronization performance while keeping the receiver training information overhead to a minimum.

The main assumption usually made when WLAN systems are designed is that the channel is *quasi-stationary*, i.e., the CIR does not change significantly during one data burst [16]. This assumption is justified by the quite short time duration of transmitted packets and by the fact that the transmitter and receiver move very slowly relative to each other. Under this assumption, most of the synchronization for WLAN receivers is done during the preamble and need not be changed during the packet.

A. IEEE 802.11a PREAMBLE

The PLCP preamble is carefully designed to be used for synchronization. It consists of ten short symbols and two long symbols, as illustrated in Figure 13. The short training symbols are denoted by t_1 to t_{10}, whereas T_1 and T_2 denote long training symbols. The total preamble length is $16\ \mu s$. The dashed boundaries in the figure denote repetitions due to periodicity of the IFFT. The training structure is followed by the SIGNAL field and DATA.

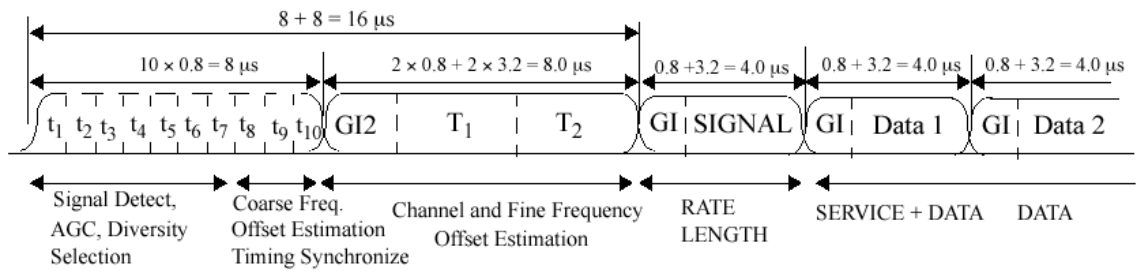

Figure 13. PLCP Preamble (From Ref. [19].)

A short OFDM training symbol consists of 12 subcarriers, which are modulated by the elements of the sequence S, given by [19]

$$\begin{aligned} S_{-26,26} = \sqrt{13/6} \times \{ & 0,0,1+j,0,0,0,-1-j,0,0,0,1+j,0,0,0,-1-j,0,0,0, \\ & -1-j,0,0,0,1+j,0,0,0,0,0,0,0,-1-j,0,0,0,-1-j, \\ & 0,0,0,1+j,0,0,0,1+j,0,0,0,1+\mathrm{j},0,0,0,1+\mathrm{j},0,0\}. \end{aligned} \tag{3.1}$$

The multiplication by a factor of $\sqrt{13/6}$ is to normalize the average power of the resulting OFDM symbol, which uses 12 out of 52 subcarriers. From Equation (3.1) we observe that only the indices that are multiples of 4 have nonzero amplitude. This fact results in a periodicity of $T_{FFT}/4 = 0.8$ µs ,which is clearly shown in Figure 14.

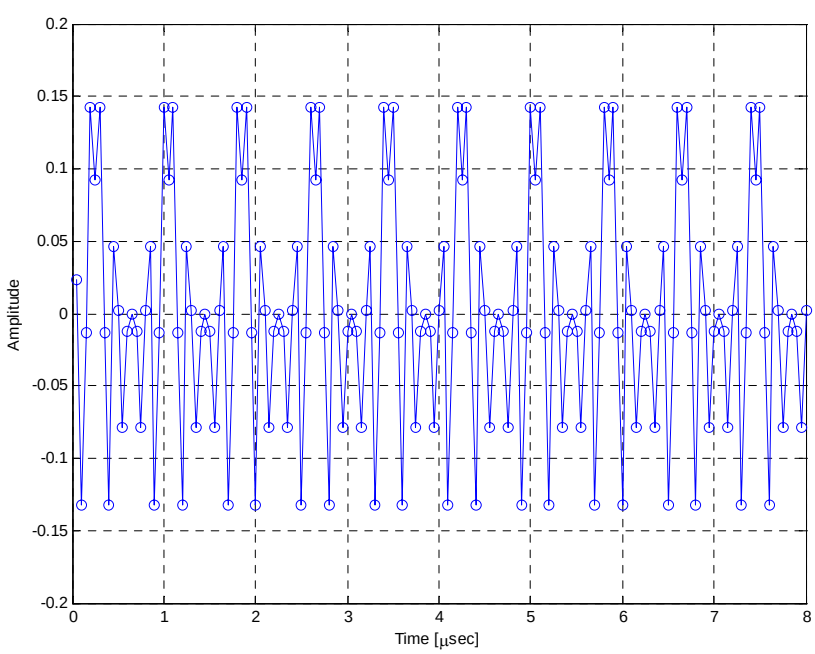

Figure 14. Short Training Sequence (Real Part.)

The interval T_{SHORT} is equal to ten $0.8\ \mu s$ periods, that is, $8\ \mu s$.

A long OFDM training symbol consists of 53 subcarriers, which are modulated by the elements of the following sequence [19]

$$L_{-26,26} = \{1,1,-1,-1,1,1,-1,1,-1,1,1,1,1,1,1,-1,-1,1,1,-1,1,-1,1,1,1,1,0, \\ 1,-1,-1,1,1,-1,1,-1,1,-1,-1,-1,-1,-1,1,1,-1,-1,1,-1,1,-1,1,1,1,1\}. \quad (3.2)$$

Two periods of the long sequence are transmitted for improved channel estimation accuracy, yielding

$$T_{LONG} = T_{GI2} + 2 \times T_{FFT} = 1.6 + 2 \times 3.2 = 8\ \mu s, \quad (3.3)$$

where T_{GI2} is the guard interval for the long training sequence.

The long training sequence in the time domain is depicted in Figure 15, where the first sample of each period is marked.

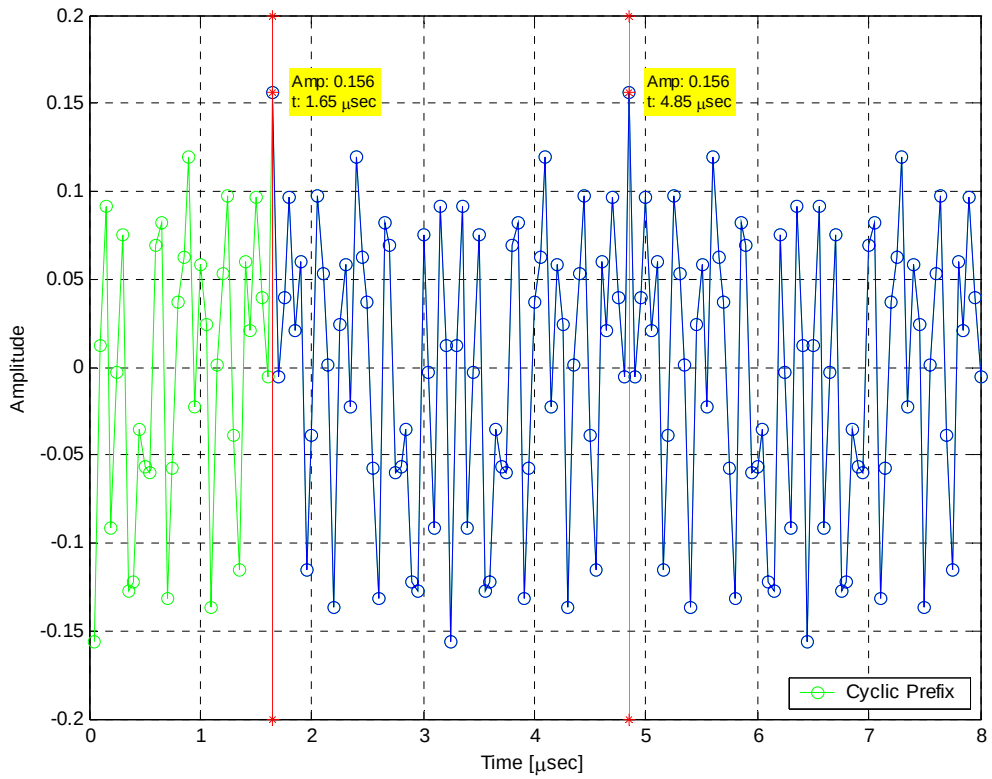

Figure 15. Long Training Sequence (Real Part.)

The time domain representation is derived by performing IFFT on the frequency domain representation of the long sequence and then cyclically extending the last 32 samples to obtain the cyclic prefix.

B. PACKET DETECTION

Packet detection is the task of estimating when the incoming data packet begins. Because this is the first synchronization algorithm that is performed, the rest of the synchronization process is dependent on good packet detection performance. IEEE 802.11a standard has set two different requirements for Clear Channel Assessment (CCA) [19]. The first is the detection probability when the preamble is available, and the second is the detection probability when the preamble is not available. The requirement for the first case is that the CCA algorithm shall indicate a *Busy* channel with >90% probability within $4\text{-}\mu\text{s}$ observation window, if a signal is received at $-82\ \text{dBm}$ level. For the second case, when the known preamble structure is not available, the requirement is relaxed by $20\ \text{dB}$. Thus a signal detection of $> 90\%$ within $4\text{-}\mu\text{s}$ observation for a received signal level of $-62\ \text{dBm}$ is required.

As in any general hypothesis test problem [4], the packet detection algorithm checks whether the decision variable m_n exceeds a predefined threshold λ:

$$\begin{aligned} m_n < \lambda &\Rightarrow \text{ Packet not present} \\ m_n > \lambda &\Rightarrow \text{ Packet present.} \end{aligned} \tag{3.4}$$

The performance of the algorithm can be summarized with two probabilities:

- Probability of detection P_d, defined as the probability of detecting the packet when it is truly present.
- Probability of a false alarm P_{fa}, defined as the probability of incorrectly deciding that the packet is present when actually it is not.

Setting the threshold lower increases P_d but also increases P_{fa}. Hence, the algorithm designer must settle for a balanced compromise between the two conflicting goals.

In general, a little higher P_{fa} can be tolerated to guarantee the high P_d. The reason is that, after a false alarm, the receiver will try to synchronize to nonexistent packet and will detect its error at the first data integrity check [16]. On the other hand, not detecting a packet always results in lost data.

1. Using the Preamble for Packet Detection

The preamble of IEEE 802.11a standard has been designed to help detect the starting edge of the packet. The following approach was presented in [20] for acquiring symbol timing, but the general method is applicable to packet detection. This method, also called *the Delay and Correlate Algorithm,* takes advantage of the periodicity of the short training symbols at the start of the preamble.

The signal flow structure of the delay and correlate algorithm is illustrated in Figure 16, where c_n, p_n are summations over some window of length L:

$$\begin{aligned} c_n &= \sum_{k=0}^{L-1} r_{n+k} r_{n+k+D}^* \\ p_n &= \sum_{k=0}^{L-1} r_{n+k+D} r_{n+k+D}^* = \sum_{k=0}^{L-1} \left| r_{n+k+D} \right|^2 . \end{aligned} \tag{3.5}$$

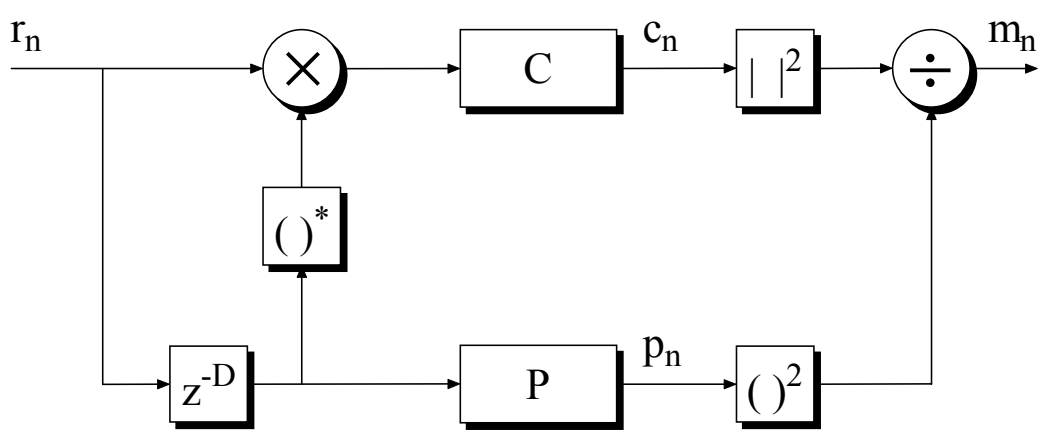

Figure 16. Block Diagram of Delay and Correlate Algorithm

The *C* block is a cross-correlation between the received signal and a delayed version of itself, hence the name "delay and correlate." The delay *D* is equal to the period of

the short training symbols (i.e., $D = 16$). The P block measures the received signal energy during the cross-correlation window, and it is used to normalize the decision statistic:

$$m_n = \frac{|c_n|}{p_n}. \tag{3.6}$$

Figure 17 shows an example of the decision statistic m_n using the short training sequence with 0-dB SNR. The packet was set to start at $n = 400$ and the delay was $D = 16$ samples, in order to satisfy the IEEE 802.11a requirements. The overall response is restricted between [0,1] and the step at the start of the packet is quite clear. The low level of m_n before the start of the packet is straight forward; when the received signal consists of only noise, the delayed cross-correlation is zero-mean random variable, since the noise samples are independent and thus uncorrelated. Once the start of the packet is received, the cross-correlation of the periodic short training symbols causes m_n to jump to the maximum value. This jump gives quite a good estimate of the start of the packet.

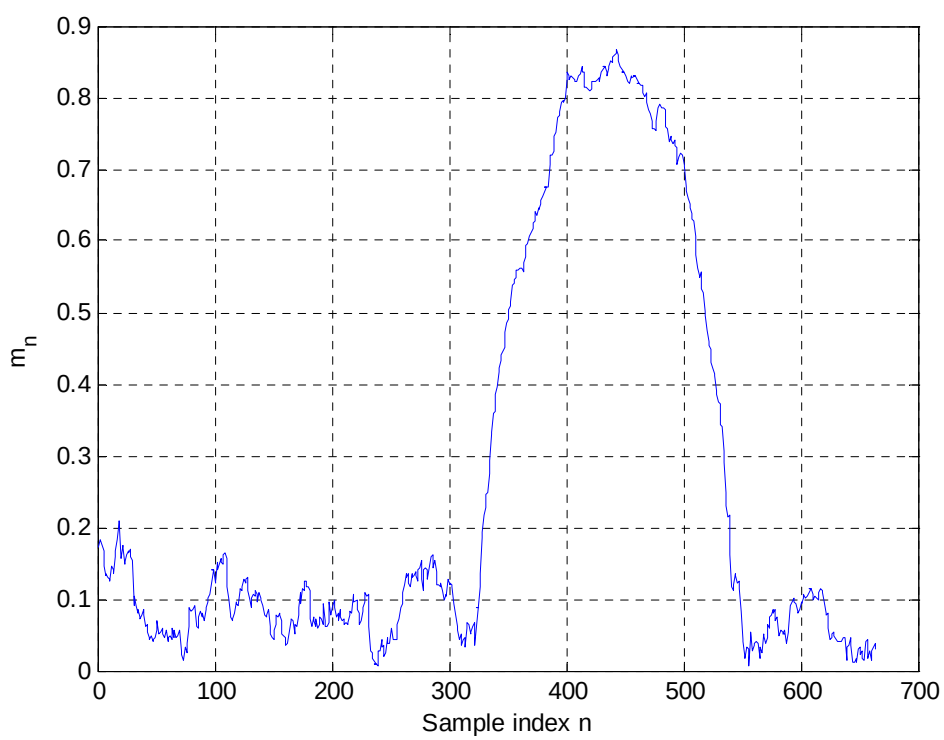

Figure 17. Packet Detection Using the Preamble (SNR = 0 dB.)

Following the previous discussion, a threshold value of 0.75 yields a high P_d. It must be noted that, in a higher SNR, the performance of the algorithm is improved.

2. Packet Detection When Preamble Is Not Available

The only possible approach to satisfy the CCA requirements when the preamble is not available is to measure the received signal energy [9]. The reason for this is the maximum allowed length of $4\ \mu s$ for the observation time, which is equal to one OFDM symbol length in the IEEE 802.11a system. Hence, there is no available signal structure that could be used to improve the detection probability. In other words, it cannot be guaranteed that a whole OFDM symbol is received, which will allow one to take advantage of the cyclic prefix properties. The response of this algorithm is illustrated in Figure 18. Intuitively, the jump of m_n at the 400-th sample gives a rough estimate of the start of the packet.

In this case, the decision variable m_n is the received signal energy accumulated over some window of length $L = 80$ samples:

$$m_n = \sum_{k=0}^{L-1} r_{n-k} r_{n-k}^* = \sum_{k=0}^{L-1} \left| r_{n-k} \right|^2 . \tag{3.7}$$

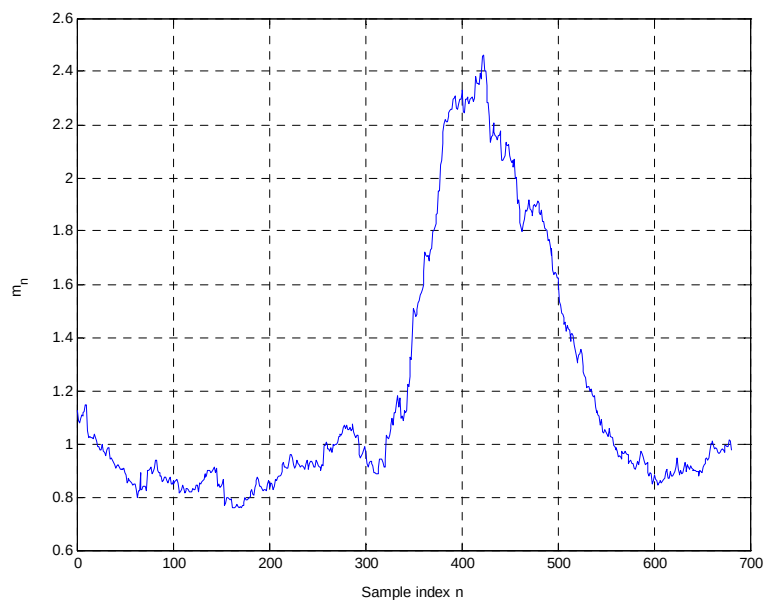

Figure 18. Packet Detection Algorithm Based on Received Signal Energy (SNR = 0 dB.)

This method suffers from a significant drawback: the threshold value depends on the received signal energy. The level of noise power is generally unknown and can change in situations where unwanted interferers go on and off in the same band as the desired system. When a wanted packet is incoming, the received signal strength depends on the power setting of the transmitter and on the total channel path loss. All these factors make it quite difficult to set a fixed threshold for the decision test.

C. FRAME/SYMBOL TIME SYNCHRONIZATION

Symbol timing refers to the task of defining the DFT window, i.e., the set of samples used to calculate the DFT window of each received OFDM symbol. After the packet detector has estimated the start of the packet, the symbol timing algorithm refines the estimate to sample-level precision [9]. The procedure is very similar to the delay and correlate algorithm; this time, however, a known reference signal is used instead of a delayed version of the received signal to perform the cross-correlation. The symbol timing estimate is the index n that corresponds to maximum absolute value of the cross-correlation:

$$m_n = \max_n \left| \sum_{k=0}^{L-1} r_{n+k} t_k^* \right|, \tag{3.8}$$

where the length L of the cross-correlation determines the performance of the algorithm. Larger values improve performance, but also increase the computation load.

The response of the symbol timing estimate is depicted in Figure 19. In this example, the first 64 samples (i.e., one period) of the long training sequence is used as the reference signal to compute the symbol timing estimate. Ten noise samples are added at the start of the received packet to emulate the packet detection algorithm. The simulation was run in an Additive White Gaussian Noise (AWGN) channel with $\mathrm{SNR} = 0$ dB. The start of the search is the 110th sample and the end of the search was the 210th sample of the packet.

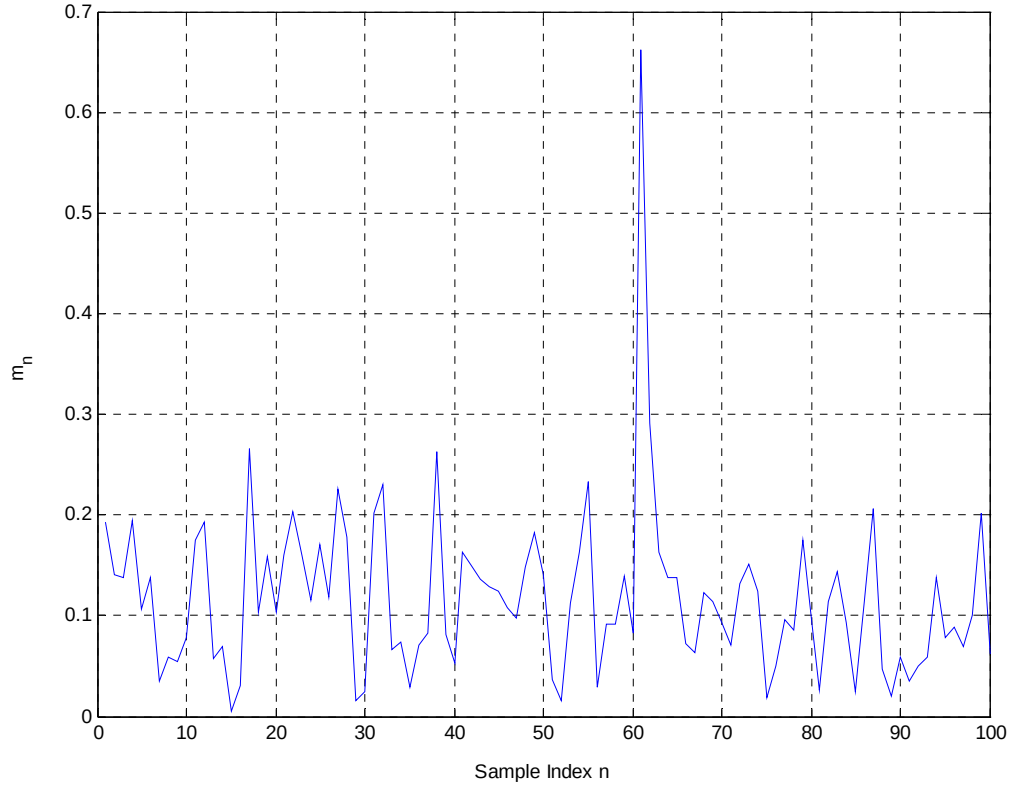

Figure 19. Response of the Symbol Timing Cross-correlator

The high peak at $n = 61$ clearly shows the correct symbol timing point. Indeed,

$$startSearchIndex + n - extraNoiseSamples = 110 + 61 - 10 = 161, \tag{3.9}$$

which is the first sample of the long training sequence in the preamble.

1. Symbol Timing in a Multipath Channel

The performance of the symbol timing algorithm has a direct influence on the effective multipath tolerance of an OFDM system. An OFDM receiver achieves maximum multipath-fading tolerance when the symbol timing is fixed to the first sample of an OFDM symbol. In practice, however, fixing the symbol timing point perfectly to the first sample of the DFT window is impossible [8]. Some jitter in the symbol timing estimate around the mean value will always exist. This effect is illustrated in Figure 20.

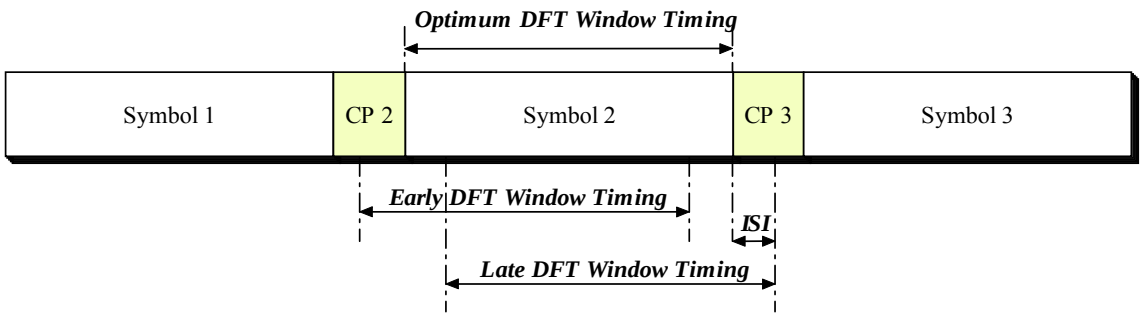

Figure 20. DFT Window Timing

The OFDM symbol has a guard interval, which is a cyclic extension of the original symbol. Thus no degradation occurs if the DFT window is set early but within the guard interval – the DFT window will contain samples from the CP and the last samples of the symbol are not used at all. It is possible that some ISI is caused if the channel impulse response is long enough to reach the first samples of the DFT window; however, the amount of this kind of ISI is negligible because the last channel taps are small.

In the case of late DFT window timing, the start of the DFT will be after the first sample of the symbol and the last samples are taken from the CP of the next symbol. Hence, the ISI is created by the samples of the next symbol. Additionally, the circular convolution property required for the orthogonality of the subcarriers is no longer satisfied and the ICI is generated. The end result of a late symbol timing estimate is a significant performance loss.

Fortunately, a simple solution to this problem exists [9]. The symbol timing estimate can be shifted slightly left (i.e., early) since early DFT window timing does not cause significant problems. The optimal amount of the shift depends on the OFDM system parameters and the performance of the frame synchronization algorithm. For a IEEE 802.11a system, 4 to 6 samples are typical values. The downside of the early shift of the DFT window timing is reduced multipath tolerance of the OFDM system. The shift shortens the effective guard interval because some samples of the CP are always used for the DFT window. However, as was mentioned earlier, the last taps of the CIR are quite small and the performance degradation is not serious.

D. FREQUENCY SYNCHRONIZATION

One of the main impairments of the OFDM is its sensitivity to carrier frequency offset. Performance degradation of the coherent OFDM modem due to a frequency offset between transmitter and receiver, including channel phase noise was analyzed in [21, 22]. The degradation is caused by two main factors:

- Amplitude reduction of the desired subcarrier, and
- Intercarrier Interference.

The amplitude loss happens because the desired subcarrier is no longer sampled at the peak of the sinc-function of the DFT. Neighboring carriers cause interference due to the loss of orthogonality. Therefore, OFDM signals are more sensitive to frequency offset than single carrier modulation signals

In [21], the channel is modeled by a time-varying phase $\theta(t)$ caused by either a carrier offset between the receiver and transmitter carrier, or the phase noise of these carriers. In the first case, $\theta(t)$ is deterministic and equals $2\pi t\Delta F + \theta_0$, where ΔF is the carrier offset. In the second case, $\theta(t)$ is modeled as a Wiener process [10] for which $E\left[\theta(t)\right] = 0$ and $E\left[\theta(t+t_0) - \theta(t_0)\right]^2 = 4\pi\beta|t|$, where β denotes the one-sided 3-dB linewidth of the Lorentzian power spectral density (psd) of the local oscillator (LO).

Based on this model, for a fixed total symbol rate R, with $R = N/T$ for OFDM and $R = 1/T$ for SC the degradation $\Lambda[\text{dB}]$ of SNR was approximated by [21]:

- Carrier Offset Case

$$\Lambda[\text{dB}] \cong \begin{cases} \dfrac{10}{\ln 10}\dfrac{1}{3}\left(\pi N \dfrac{\Delta F}{R}\right)^2 \dfrac{E_b}{N_0} & \text{OFDM} \\ \dfrac{10}{\ln 10}\dfrac{1}{3}\left(\pi \dfrac{\Delta F}{R}\right)^2 & \text{SC}\,. \end{cases} \tag{3.10}$$

For both OFDM and SC, the degradation is proportional to the square of the frequency offset. For OFDM, the degradation is also proportional to the E_b/N_0, and with the square of the number of subcarriers.

- Phase Noise Case

$$\Lambda[\text{dB}] \cong \begin{cases} \dfrac{10}{\ln 10}\dfrac{11}{60}\left(4\pi N\dfrac{\beta}{R}\right)\dfrac{E_b}{N_0} & \text{OFDM} \\ \dfrac{10}{\ln 10}\dfrac{1}{60}\left(4\pi\dfrac{\beta}{R}\right)\dfrac{E_b}{N_0} & \text{SC} \end{cases} . \tag{3.11}$$

For both OFDM and SC, the degradation is proportional with E_b/N_0, and the linewidth β. For OFDM, the degradation is also proportional with the number of subcarriers.

Now, in the AWGN channel at $\text{BER} = 10^{-6}$ the E_b/N_0 is 10.5, 14.4, and 18.8 dB for BPSK/QPSK, 16-QAM, and 64-QAM respectively, as depicted in Figure 21.

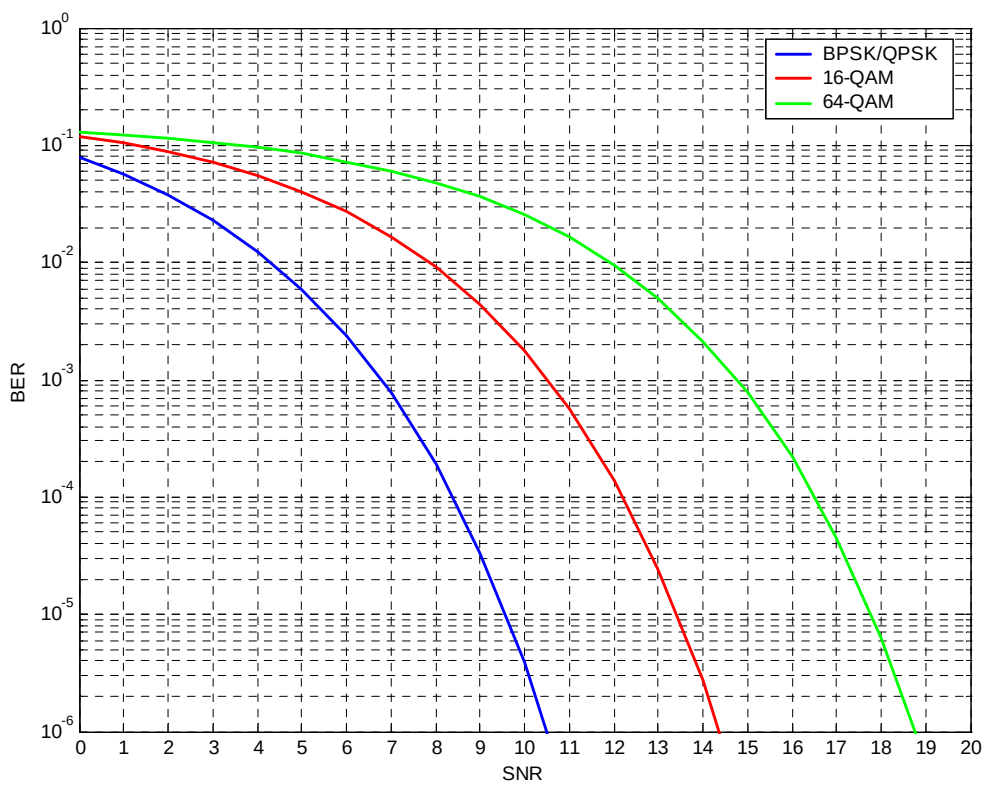

Figure 21. Performance of BPSK/QPSK, 16-QAM and 64-QAM in AWGN

The probability of bit error in AWGN is given by [14]

$$P_b = \begin{cases} \frac{1}{2}\operatorname{erfc}\left(\sqrt{\frac{E_b}{N_0}}\right) & \text{BPSK/QPSK} \\ \frac{3}{8}\operatorname{erfc}\left(\sqrt{\frac{2}{5}\frac{E_b}{N_0}}\right) - \frac{9}{24}\operatorname{erfc}\left(\sqrt{\frac{2}{5}\frac{E_b}{N_0}}\right)^2 & \text{16-QAM} \\ \frac{7}{24}\operatorname{erfc}\left(\sqrt{\frac{1}{7}\frac{E_b}{N_0}}\right) - \frac{49}{384}\operatorname{erfc}\left(\sqrt{\frac{1}{7}\frac{E_b}{N_0}}\right)^2 & \text{64-QAM .} \end{cases} \tag{3.12}$$

Figure 22 illustrates the degradation in IEEE 802.11a performance versus the frequency offset, while the SNR degradation versus the phase noise linewidth is depicted in Figure 23. Both ΔF and β are normalized to subcarrier frequency spacing f_{sc}.

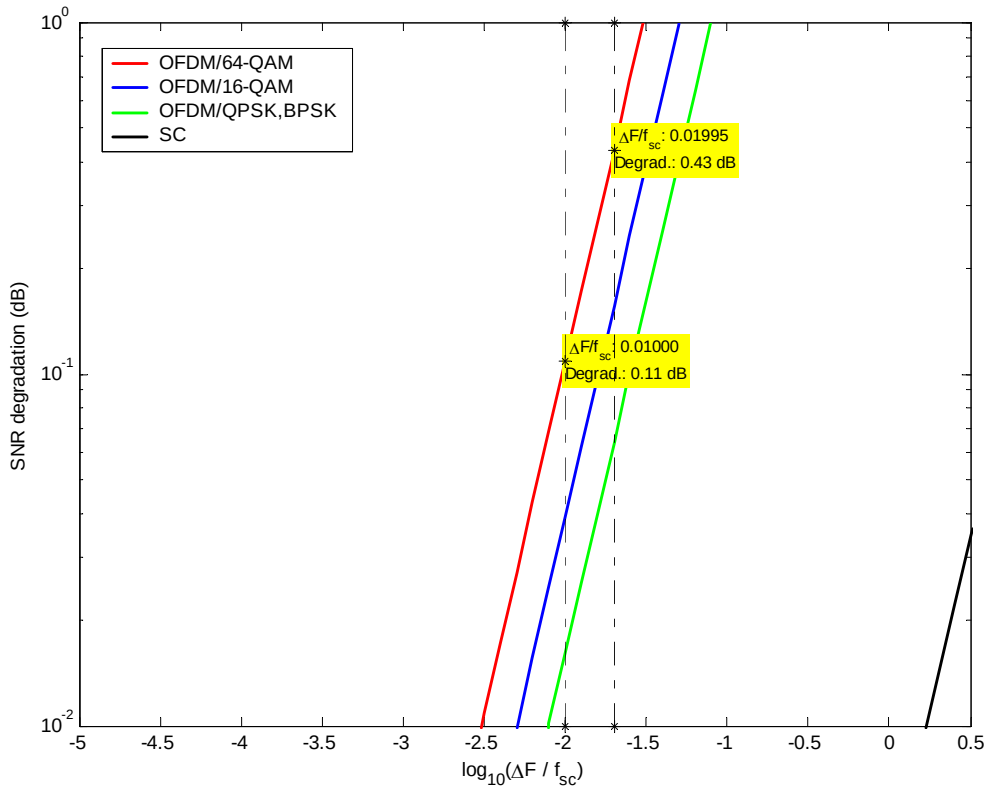

Figure 22. Distortion as Function of Relative Frequency-offset

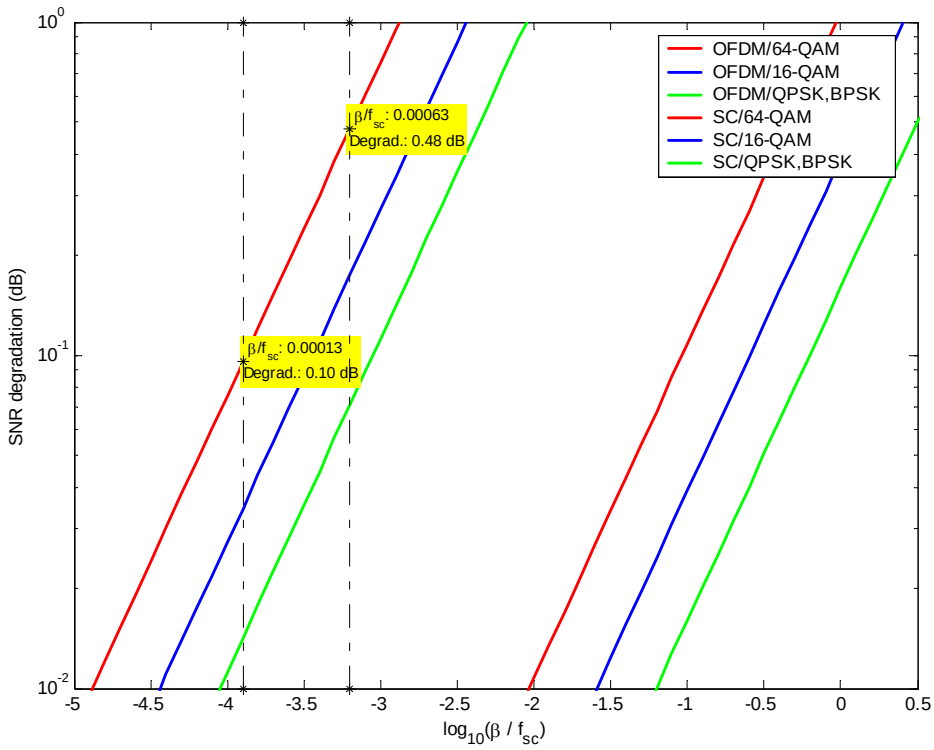

Figure 23. Distortion as Function of Oscillator Linewidth

We observe that for a fixed total symbol rate, the SNR degradation of OFDM due to frequency offset is N^2 times more sensitive that SC and the SNR degradation due to phase noise is N times more sensitive than SC [21]. The higher sensitivity of OFDM as compared to SC is caused by the N times longer duration of an OFDM symbol and by the ICI due to a loss of orthogonality. To keep the SNR degradation in IEEE 802.11a under 0.5 dB, the relative frequency offset must be below 0.02 for OFDM/64-QAM. This translates to an offset of 6 kHz $(0.02 \times 312.5 \text{ kHz})$. For OFDM/QPSK, the relative frequency offset is $\Delta F / f_{sc} = 0.056$ and the frequency offset can be relaxed to 17.5 kHz.

In the case of phase noise, to keep the SNR degradation under 0.5 dB, the relative linewidth must be below 0.0006 for OFDM/64-QAM. This translates to a linewidth of 187.5 Hz $(0.0006 \times 312.5\text{kHz})$ of the 5.3 GHz carrier. For OFDM/QPSK, the normalized linewidth is $\beta / f_{sc} = 0.05$ and the linewidth is relaxed to 1.6 kHz.

1. Maximum-Likelihood (ML) Estimation of Frequency-Offset

This method has been presented in several papers in slightly varying forms [20, 23]. The training information required is at least two consecutive repeated symbols. The IEEE 802.11a preamble satisfies this requirement for both the short and long training sequence.

Let the transmitted baseband signal be s_n, then the complex baseband model of the passband signal y_n is

$$y_n = s_n e^{j2\pi f_{tx} n T_s}, \tag{3.13}$$

where f_{tx} is the transmitter carrier frequency and T_s is the sampling interval. After the receiver down-converts the signal with a carrier frequency f_{rx}, the received complex baseband signal r_n is

$$\begin{aligned} r_n &= s_n e^{j2\pi f_{tx} n T_s} e^{-j2\pi f_{rx} n T_s} \\ &= s_n e^{j2\pi (f_{tx} - f_{rx}) n T_s} \\ &= s_n e^{j2\pi \Delta f n T_s}, \end{aligned} \tag{3.14}$$

where $\Delta f = f_{tx} = f_{rx}$ is the carrier frequency offset and noise was ignored for convenience.

Let D denote the delay between the identical samples of the two repeated symbols. Then the frequency offset estimator is developed as follows [22]:

- Compute the cross-correlation of the two consecutive symbols

$$\begin{aligned} c &= \sum_{n=0}^{L-1} r_n r_{n+D}^* \\ &= \sum_{n=0}^{L-1} s_n e^{j2\pi \Delta f n T_s} \left(s_{n+D} e^{j2\pi \Delta f (n+D) T_s} \right)^* \\ &= \sum_{n=0}^{L-1} s_n s_{n+D}^* e^{j2\pi \Delta f n T_s} e^{-j2\pi \Delta f (n+D) T_s} \\ &= e^{-j2\pi \Delta f \cdot D T_s} \sum_{n=0}^{L-1} \left| s_n \right|^2. \end{aligned} \tag{3.15}$$

- Form the frequency offset estimator as

$$\hat{\Delta f} = -\frac{1}{2\pi D T_s}\text{angle}(c). \tag{3.16}$$

The ML estimation of frequency offset can also be derived after the DFT processing (i.e., in frequency domain). Following the analysis in [22], the received signal during two repeated symbols is (ignoring noise for convenience),

$$r_n = \frac{1}{N}\left[\sum_{k=-K}^{K} X_k H_k e^{\frac{j2\pi n(k+f_\Delta)}{N}}\right] \quad n = 0,1,...,2N-1, \tag{3.17}$$

where X_k are the transmitted data symbols, H_k is the channel frequency response for subcarrier *k*, *K* is the total number of subcarriers, and $f_\Delta = \Delta f / f_{sc}$ is the relative frequency offset to the subcarrier spacing. The DFT of the first symbol and for the *k*-th subcarrier is

$$R_{1,k} = \sum_{n=0}^{N-1} r_n e^{-\frac{j2\pi kn}{N}} \quad k = 0,1,...,N-1. \tag{3.18}$$

The DFT of the second symbol is

$$\begin{aligned} R_{2,k} &= \sum_{n=N}^{2N-1} r_n e^{-\frac{j2\pi kn}{N}} \\ &= \sum_{n=0}^{N-1} r_{n+N} e^{-\frac{j2\pi kn}{N}} \quad \text{k=0,1,...,N-1.} \end{aligned} \tag{3.19}$$

From Equation (3.17) the received signal r_{n+N} is

$$\begin{aligned} r_{n+N} &= \frac{1}{N}\left[\sum_{k=-K}^{K} X_k H_k e^{\frac{j2\pi (n+N)(k+f_\Delta)}{N}}\right] \\ &= \frac{1}{N}\left[\sum_{k=-K}^{K} X_k H_k e^{\frac{j2\pi n(k+f_\Delta)}{N}} e^{j2\pi(k+f_\Delta)}\right] \\ &= \frac{1}{N}\left[\sum_{k=-K}^{K} X_k H_k e^{\frac{j2\pi n(k+f_\Delta)}{N}}\right] e^{j2\pi f_\Delta} \\ &= r_n e^{j2\pi f_\Delta} \quad n = 0,1,...,2N-1. \end{aligned} \tag{3.20}$$

Equation (3.20) implies that $R_{2,k} = R_{1,k} e^{j2\pi f_\Delta}$. Hence every subcarrier experiences the same shift that is proportional to the frequency offset. Cross-correlating these subcarriers we get:

$$\begin{aligned} C &= \sum_{k=-K}^{K} R_{1,k} R_{2,k}^* \\ &= \sum_{k=-K}^{K} R_{1,k} \left(R_{1,k} e^{j2\pi f_\Delta} \right)^* \\ &= e^{-j2\pi f_\Delta} \sum_{k=-K}^{K} R_{1,k} R_{1,k}^* \\ &= e^{-j2\pi f_\Delta} \sum_{k=-K}^{K} \left| R_{1,k} \right|^2 . \end{aligned} \tag{3.21}$$

Thus the frequency offset estimator is

$$\hat{f}_\Delta = -\frac{1}{2\pi} \text{angle}(C) \Leftrightarrow \hat{\Delta f} = -\frac{f_{sc}}{2\pi} \text{angle}(C), \tag{3.22}$$

which is quite similar in form to the time domain version of the ML estimation.

2. Properties of the Frequency-offset Estimation Algorithm

An important feature of the previous method is its operating range, i.e., the maximum value of the frequency offset that can be estimated [9]. The $\text{angle}(c)$ is of the form $-2\pi \Delta f D T_s$, which is unambiguously defined only in the range $[-\pi, \pi)$. Thus, the absolute value of the frequency offset estimate must obey

$$\left| \hat{\Delta f} \right| \le \frac{\pi}{2\pi D T_s} = \frac{1}{2 D T_s}, \tag{3.23}$$

otherwise the estimate will be incorrect. Now, if the delay D is equal to the number of subcarriers, N, then

$$\left| \hat{\Delta f} \right| \le \frac{1}{2 N T_s} = \frac{f_{sc}}{2} \Rightarrow \frac{\left| \hat{\Delta f} \right|}{f_{sc}} \le \frac{1}{2}, \tag{3.24}$$

where the frequency offset is normalized with the subcarrier spacing f_{sc}. Hence, in this case the relative frequency error can be at most 0.5.

As an example, we computed the value of this limit for both the short and long training sequences of the IEEE 802.11a system. For the short training symbols, the delay is $D = 16$. Thus, the maximum frequency offset can be estimated as

$$\Delta f_{\max,short} = \frac{1}{2 \times 16 \times 50 \times 10^{-9}} = 625 \text{ kHz.} \tag{3.25}$$

For the long training symbols, the delay is $D = 64$ and therefore

$$\Delta f_{\max,long} = \frac{1}{2 \times 64 \times 50 \times 10^{-9}} = 156.25 \text{ kHz.} \tag{3.26}$$

The results should be compared with the maximum possible frequency error in an IEEE 802.11a system. The carrier frequency is roughly 5.3 GHz, and a maximum oscillator error of 20 ppm is specified [19]. If the transmitter and receiver clocks have the maximum allowed error, but with opposite signs, the observed error will be 40 ppm. This amounts to a frequency error of $\Delta f = 40 \times 10^{-6} \times 5.3 \times 10^{9} = 212 \text{ kHz}$. We observe that the maximum possible frequency error can be resolved only when the short training sequence is used. In other words, the frequency offset estimate would be unreliable if only the long training sequence were used.

For this reason, [19] suggests a two-step frequency estimation process with a coarse frequency estimate performed from the short training sequence and a fine frequency synchronization from the long training sequence.

E. COMBINED FRAME AND FREQUENCY ESTIMATION

In [20], a rapid synchronization method was presented using a training sequence of two identical symbols. This method resembles the delay and correlate algorithm introduced in the packet detection section. The main difference in this method is that the window length L must equal the delay D, i.e.,

$$\begin{aligned} c_n &= \sum_{k=0}^{D-1} r_{n+k} r_{n+k+D}^{*} \\ p_n &= \sum_{k=0}^{D-1} \left| r_{n+k+D} \right|^2, \end{aligned} \tag{3.27}$$

where D is one symbol length. In hardware implementation, the above summations can be implemented with the iterative formulas:

$$\begin{aligned} c_{n+1} &= c_n + (r_{n+D} r_{n+2D}^*) - (r_{n-1} r_{n+D-1}^*) \\ p_{n+1} &= p_n + |r_{n+2D}|^2 - |r_{n+D-1}|^2 . \end{aligned} \tag{3.28}$$

Thus the number of complex multiplications is reduced to one per received sample. The same algorithm can be used to compute the frequency offset estimate

$$\hat{\Delta f} = -\frac{1}{2\pi D T_s} \text{angle}(c_{n_0}), \tag{3.29}$$

where c_{n_0} is the cross-correlation value corresponding to the symbol timing estimate n_0.

It can be shown [23] that in an AWGN channel the estimator $\hat{\Delta f}$ is a maximum-likelihood estimate of the frequency offset. Additionally, under the same AWGN assumption and at a high SNR, the variance $\sigma^2_{\Delta f}$ of the estimator is proportional to [20]

$$\sigma^2_{\hat{\Delta f}} \propto \frac{1}{D \cdot \text{SNR}}, \tag{3.30}$$

where D denotes the window length. Hence, the more samples in the sum, the better the quality of the estimator will be.

This algorithm can be applied to a IEEE 802.11a system for rapid synchronization using only the short training sequence. Recall that the short training sequence consists of ten identical symbols, 16 samples each. Hence the delay D can take the following values

$$D = 16 \cdot k, \quad \text{for } k = 1, 2, ..., 5. \tag{3.31}$$

The symbol timing estimate is illustrated in Figure 24, using an 80-sample delay in an AWGN channel of 10-dB SNR. The simulation was run setting the frequency offset to 100 kHz. Also, 400 noise samples were added at the start of the packet to simulate the packed detection algorithm.

Recall that the decision statistic m_n is given by

$$m_n = \frac{|c_n|^2}{p_n^2}, \tag{3.32}$$

where c_n is the delayed cross-correlation and p_n is the received power of the second half-symbol.

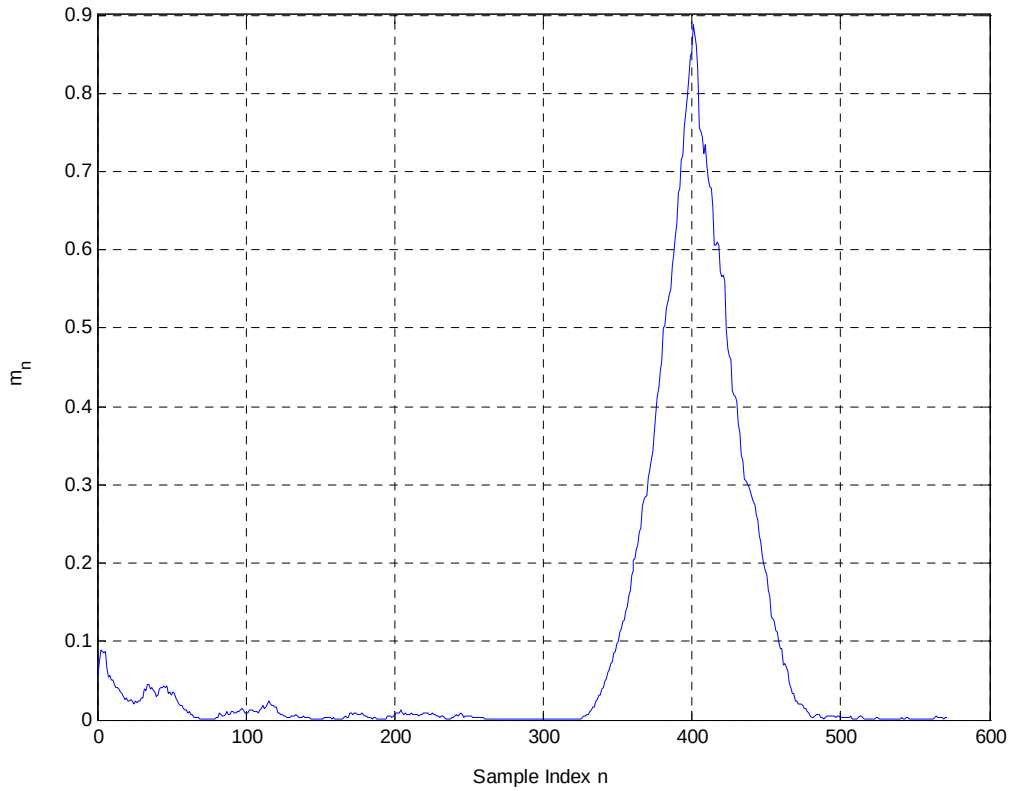

Figure 24. Symbol Timing Estimate in AWGN, $\text{SNR} = 10$ dB

We observe that the high peak at $n = 401$ clearly shows the correct symbol timing point. At that point, the frequency offset was estimated to be $\hat{\Delta f} = 99.88$ kHz. The performance of the symbol timing / frequency offset estimation algorithm is dramatically improved at higher SNR.

Figure 25 shows the probability density function (PDF) of the symbol timing estimate.

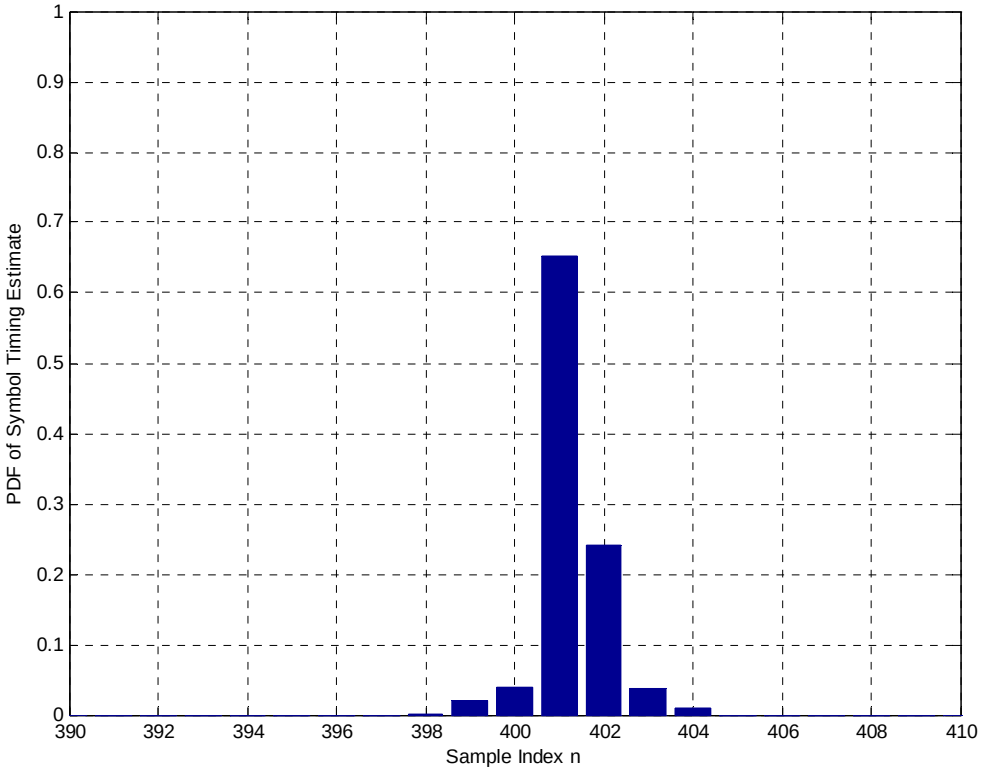

Figure 25. PDF of Symbol-timing Estimate in AWGN, $\text{SNR} = 10$ dB

The simulation was run 50000 times using $D = 80$, $\Delta f = 100$ kHz, $\text{SNR} = 10$ dB. The channel was AWGN and 400 noise samples were added at the start of the packet to test the packet detection performance of the algorithm.

Figure 26 illustrates the performance of the timing estimate under a fading channel. The RMS delay spread was set to 50 ns, and the rest of the parameters were kept the same.

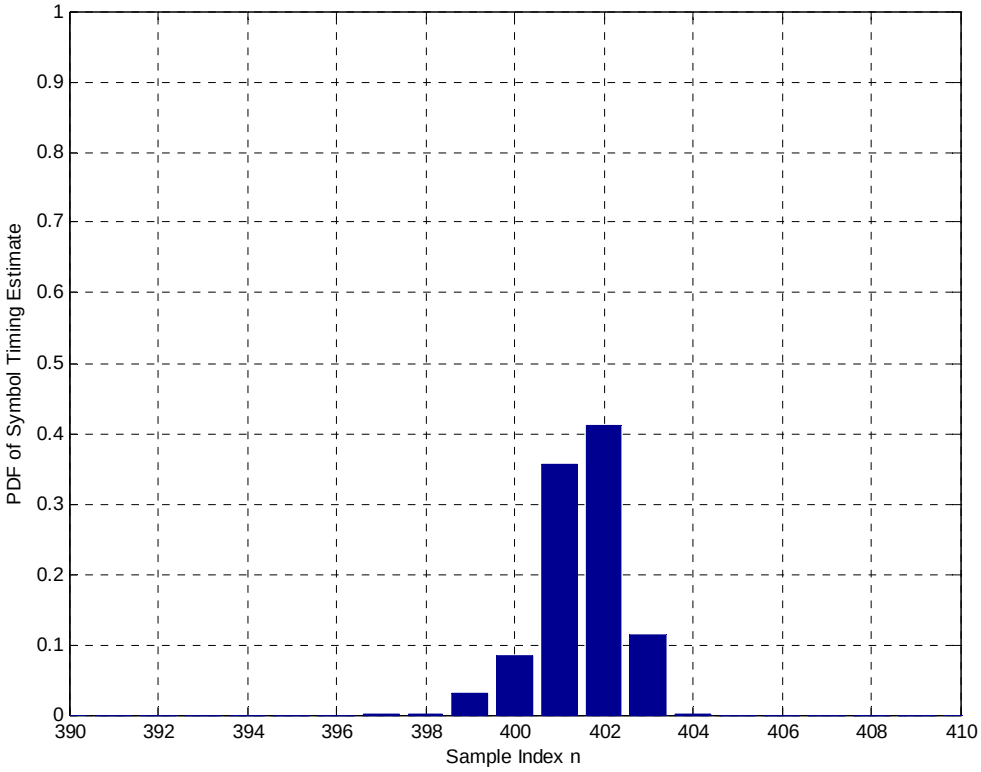

Figure 26. PDF of Symbol-timing Estimate in 50 ns Delay Spread, SNR = 10 dB

The symbol timing algorithm estimated the correct symbol more than 90% of the time, with one-sample precision. Comparing Figure 25 with Figure 26, we conclude that the performance of the timing algorithm is not really affected by multipath fading. Additionally, the higher the SNR is, the more accurate the algorithm becomes. In a lower SNR, we can shift the DFT time window four to six samples earlier in order to avoid ISI in a multipath environment.

The estimation of the carrier frequency offset was quite accurate as well. The PDF of the frequency offset estimate in AWGN and 50-ns multipath fading is shown in Figure 27 and Figure 28, respectively.

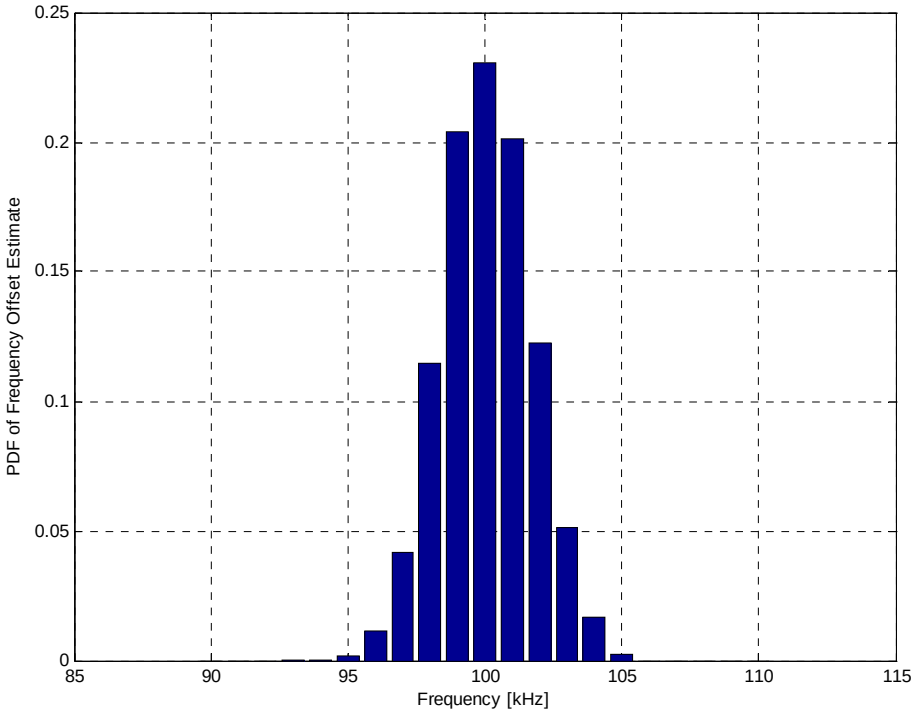

Figure 27. PDF of Frequency-offset Estimate in AWGN, $\mathrm{SNR} = 10$ dB

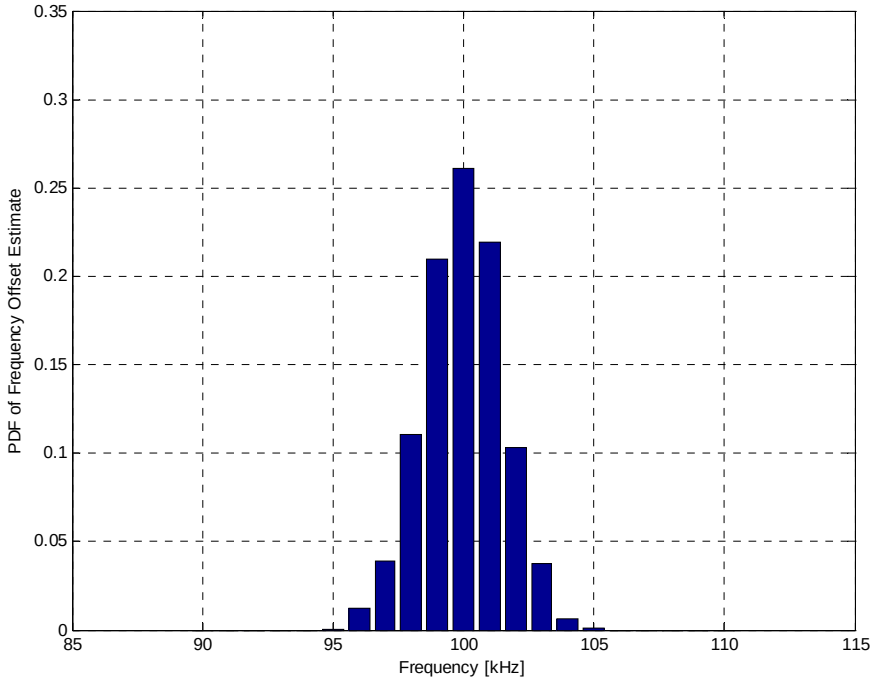

Figure 28. PDF of Frequency-offset Estimate in 50 ns Delay Spread, $\mathrm{SNR} = 10$ dB

The PDF of the algorithm is bell-shaped, centered at 100 kHz with a dispersion of 3 kHz. This translates to a relative frequency offset of $3\text{ kHz}/312.5\text{ kHz} \approx 0.01$. In other words, the algorithm successfully corrected the frequency offset with a relative residual error of 1%. Hence, the SNR degradation is negligible. Again, we observe that multipath fading does not really affect the performance of the algorithm.

An additional benefit of this approach is that, at the peak point of m_n, the value of p_n contains the sum of signal energy *S* and noise energy *N* and the c_n value is equal to signal energy *S*. Thus the value of m_n at the peak point can be used to estimate the received SNR. The SNR estimator is developed as follows:

$$\begin{aligned} &\sqrt{m_n} = \frac{|c_n|}{p_n} = \frac{S}{S+N} \Rightarrow \\ &S\left(1-\sqrt{m_n}\right) = N\sqrt{m_n} \Rightarrow \\ &SNR = \frac{\sqrt{m_n}}{1-\sqrt{m_n}}. \end{aligned} \tag{3.33}$$

It must be noted that the estimator works well for the SNR below 20 dB [20]. Above this level, m_n is so close to 1 that an accurate estimate of the SNR can not be determined, but only that the SNR is above 20 dB. Hence, this estimate can be used to set a threshold so that very weak signals will not be decoded. The SNR estimate can also be used as a feedback to the transmitter to indicate what data rate can be supported, so that an appropriate constellation and code rate can be chosen. In the case of a fading channel, all the signal energy goes into the c_n term, assuming that the channel taps do not exceed the cyclic prefix.

The PDF of the estimated SNR in a multipath fading channel with 50-ns rms delay spread is illustrated in Figure 29.

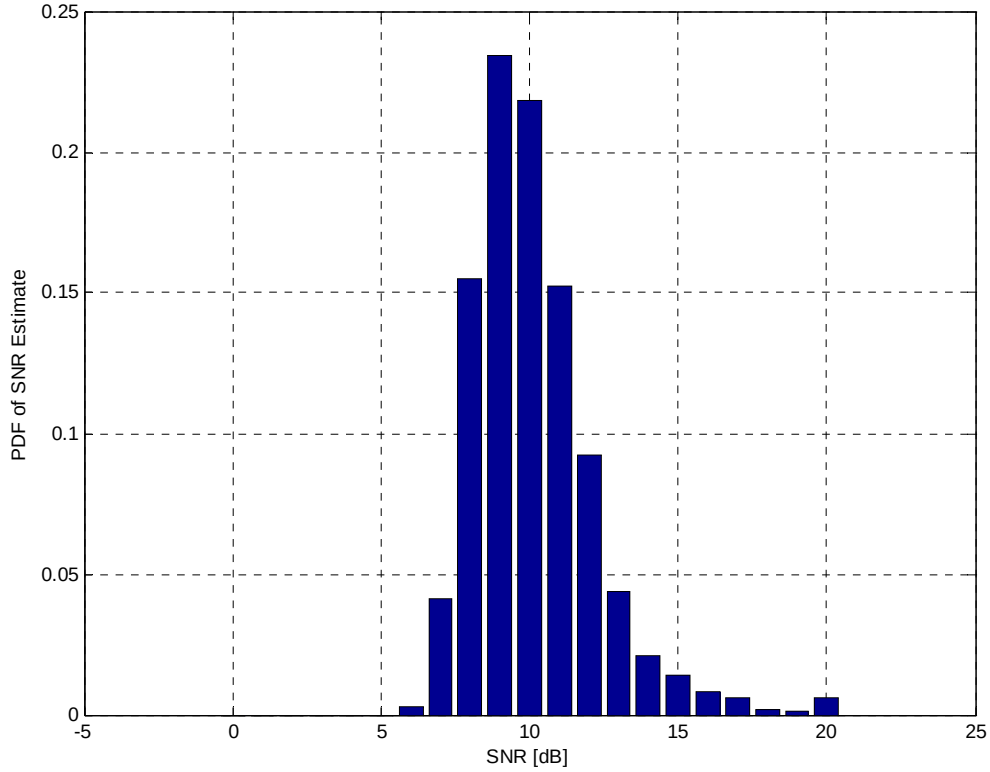

Figure 29. PDF of SNR Estimate in 50nsec Delay Spread, $\mathrm{SNR} = 10$ dB

As previously discussed, the IEEE 802.11a standard requires that the CCA algorithm shall indicate a *Busy* channel within $4\text{-}\mu\mathrm{s}$ observation window, i.e., within 80 samples. Additionally, the maximum allowed frequency error is defined as 212 kHz. Using this algorithm with $D = 80$, the observation window becomes $8\ \mu\mathrm{s}$ while the maximum estimated frequency error is 125 kHz. Hence, neither of the requirements are satisfied.

To address these issues, a two-step approach is proposed in this thesis; the packet detection algorithm operates using $D = 32$ samples. When the threshold value is exceeded, then a coarse frequency synchronization is performed and the algorithm starts computing the fine symbol timing estimate, using $D = 80$ samples. When the maximum value of the estimate is reached, the DFT timing window is defined by the corresponding sample index and a fine-frequency synchronization is performed. This proposal is illustrated in Figure 30.

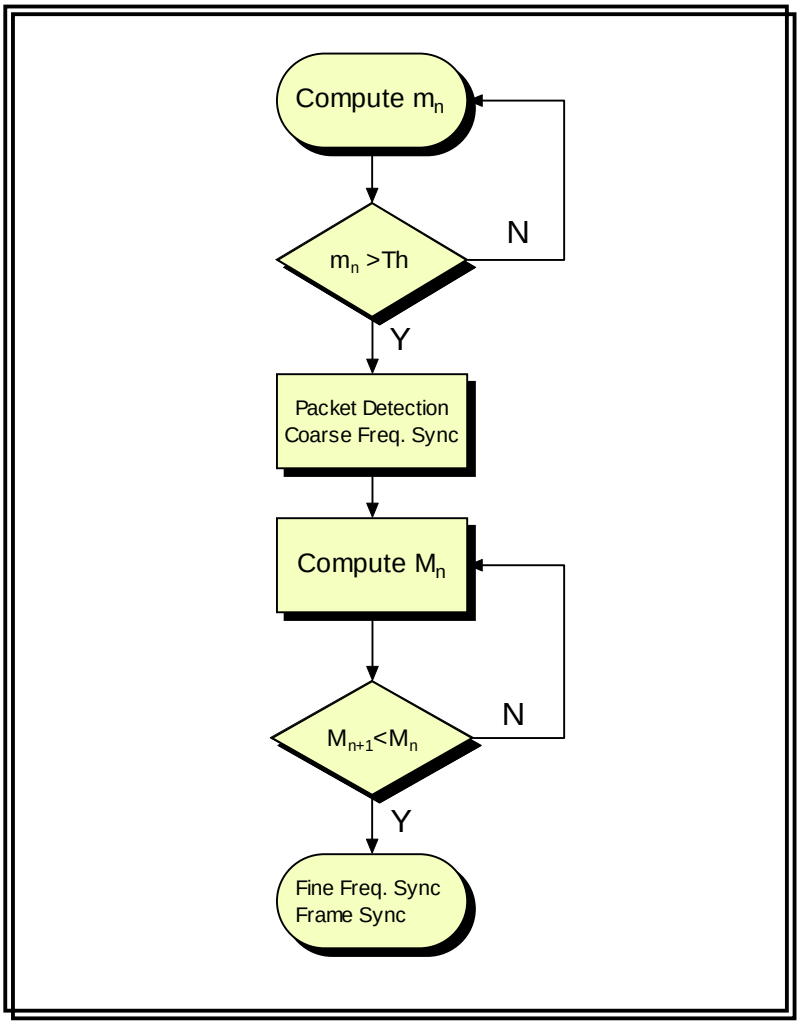

Figure 30. Flow Chart of the Proposed Synchronization Algorithm

Whether the coarse frequency synchronization step is needed or not is a designer issue; if the transmitter's oscillator is precise enough, this step can be omitted.

F. SAMPLING CLOCK ERROR

The oscillators used to generate the Digital-to-Analog Converter (DAC) and Analog-to-Digital Converter (ADC) sampling instants at the transmitter and the receiver will never have exactly the same period. Hence the sampling instants slowly shift relative to each other. This sampling clock error has two main effects:

- Slow shift in the symbol timing point, which rotates the subcarriers, and

- An SNR loss due to ICI generated by the slightly incorrect sampling instants, which causes loss of orthogonality of the subcarriers.

In [24] the normalized sampling error is defined as

$$\Delta t = \frac{T_{tx} - T_{rx}}{T_{tx}}, \tag{3.34}$$

where T_{tx} and T_{rx} are the transmitter and receiver sampling periods, respectively. The overall effect, after DFT, on the received subcarriers $R_{l,k}$ is shown [24] as

$$R_{l,k} = e^{j2\pi k\Delta t l \frac{T_{OFDM}}{T_{FFT}}} X_{l,k} \sin c(\pi k \Delta t) + W_{l,k} + N_{\Delta t}(l,k), \tag{3.35}$$

where l is the OFDM symbol index, k is the subcarrier index, T_{OFDM} and T_{FFT} are the duration of the total OFDM symbol and the useful data portion, $W_{l,k}$ is additive white noise and $N_{\Delta t}(l,k)$ is the additional interference due to the sampling frequency offset.

The power of the last term can be approximated by [24]

$$P_{\Delta t} \approx \frac{\pi^2}{3}\left(k\Delta t\right)^2. \tag{3.36}$$

Thus the SNR loss grows as the square of the product of the offset Δt and the subcarrier index k. This means that the outermost subcarriers are most severely affected. WLAN OFDM systems typically have a relatively small number of subcarriers and quite small Δt, thus $k\Delta t \ll 1$, so the SNR degradation caused by sampling frequency offset can be neglected.

Equation (3.35) shows a more significant problem caused by the offset, namely the factor

$$e^{j2\pi k\Delta t l \frac{T_{OFDM}}{T_{FFT}}}. \tag{3.37}$$

This term shows the amount of rotation angle experienced by the different subcarriers as the OFDM signal is received. The angle depends on both the OFDM symbol in-

dex l and the subcarrier index k. Thus the angle is largest for the outermost subcarriers and increases with consecutive OFDM symbols.

G. CARRIER PHASE TRACKING

Frequency estimation is not a perfect process, so there is always some residual frequency error. The SNR loss due to ICI can be neglected if the frequency estimator has been designed to reduce the frequency error below the specified limit for the used modulation. The most significant problem caused by the residual frequency error, just like a sampling error, is constellation rotation. The analysis of the post DFT frequency offset ML estimator also showed that the constellation rotation is the same for all subcarriers. To illustrate the effect in a IEEE 802.11a system, Figure 31 shows how much a QPSK constellation rotates during 11 OFDM symbols with a 3-kHz frequency error in an AWGN channel with $\mathrm{SNR} = 20$ dB.

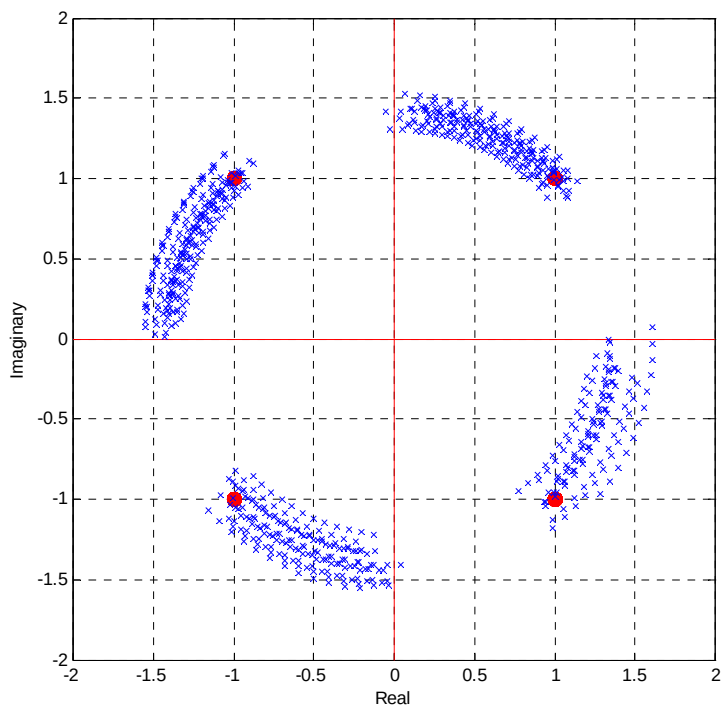

Figure 31. Constellation Rotation with 3-kHz Frequency Error

This error corresponds to only 1% of the subcarrier spacing, thus the SNR degradation is negligible. Figure 31 shows that after only 11 symbols, the constellation points have rotated over the decision boundaries shown as solid red lines. Hence, even with ideal channel conditions (AWGN only with high SNR), correct demodulation is no longer possible. This effect forces the receiver to track the carrier phase while the data symbols are received.

The simplest method for this is data-aided carrier phase tracking. IEEE 802.11a includes four predefined subcarriers among the transmitted data, commonly referred to as *pilot* subcarriers. The main purpose of the pilot subcarriers is to help the receiver track the carrier phase. After the DFT of the *l*-th received OFDM symbol, the pilot subcarriers $R_{l,k}$ are equal to the product of the channel transfer function H_k and the known pilot symbol $P_{l,k}$, rotated by the residual frequency offset [9]

$$R_{l,k} = H_k P_{l,k} e^{j2\pi n f_\Delta}, \tag{3.38}$$

where f_Δ is the relative frequency error, normalized to subcarrier spacing f_{sc}. Assuming an estimate $\hat{H}_k$ of the channel transfer function is available, the phase estimate is

$$\begin{aligned} \hat{\Phi}_l &= \text{angle}\left[\sum_{k=1}^{N_p} R_{l,k}\left(\hat{H}_k P_{l,k}\right)^*\right] \\ &= \text{angle}\left[\sum_{k=1}^{N_p} H_k P_{l,k} e^{j2\pi n f_\Delta}\left(\hat{H}_k P_{l,k}\right)^*\right], \end{aligned} \tag{3.39}$$

where N_p denotes the number of pilot subcarriers in one OFDM symbol. If we assume that the channel estimate is perfectly accurate, we calculate the estimated phase rotation

$$\begin{aligned} \hat{\Phi}_l &= \text{angle}\left[\sum_{k=1}^{N_p} \left|H_k\right|^2 \left|P_{l,k}\right|^2 e^{j2\pi n f_\Delta}\right] \\ &= \text{angle}\left[e^{j2\pi n f_\Delta} \sum_{k=1}^{N_p} \left|H_k\right|^2\right], \end{aligned} \tag{3.40}$$

where the amplitudes of the pilot subcarriers have been selected to be equal to one [19]. In this case, no phase ambiguity exists, because the pilot data are known; thus the phase

is automatically resolved correctly. It should be noted that in practice the channel transfer function estimate is not perfectly accurate. Hence channel estimation errors contribute to the noise in the phase rotation estimate.

H. CHANNEL ESTIMATION

Channel estimation is the task of estimating the transfer function of the channel. As we mentioned earlier in Chapter II, WLAN systems generally assume that the channel is *quasi-stationary,* that is, the channel does not change during one data packet. Under this assumption, the CIR was modeled as

$$h(\tau) = \sum_n \alpha_n e^{-j2\pi f_c \tau_n} \delta(\tau - \tau_n). \tag{3.41}$$

Then, the channel transfer function (CTF) is the DFT of the channel impulse response

$$H_k = DFT\{h_n\}. \tag{3.42}$$

Thus the channel estimation process generates the $\hat{H}_k$ and the estimate of the channel's transfer function for each subcarrier.

Channel estimation is mandatory for IEEE 802.11a and generally for any OFDM system that employs coherent modulation schemes [16]; otherwise, correct demodulation would not be possible. Furthermore, channel estimation can also improve OFDM systems with noncoherent modulation schemes, although the $\hat{H}_k$ is not needed for demodulation in this case. The improvement can be achieved when a Forward Error Correction (FEC) code is used in the system. Further discussion about this case is provided in Chapter IV.

1. Frequency Domain Approach

The long training sequence of the IEEE 802.11a system facilitates an easy and efficient estimate of the channel transfer function for all the subcarriers.

After the DFT processing, the received long training symbols $R_{l,k}$ are a product of the training symbols $X_{l,k}$ and the channel $H_{l,k}$ plus additive white Gaussian noise $W_{l,k}$:

$$R_{l,k} = H_{l,k} X_{l,k} + W_{l,k} \quad l = 1,2, \quad k = 0,1,...,K-1, \tag{3.43}$$

where K is the number of subcarriers. Thus the channel estimates $\hat{H}_{l,k}$ are obtained by a simple division of the received symbols $R_{l,k}$ and the long training symbols $X_{l,k}$ [25], i.e.,

$$\hat{H}_{l,k} = \frac{R_{l,k}}{X_{l,k}} = H_{l,k} + \frac{W_{l,k}}{X_{l,k}}. \tag{3.44}$$

The AWGN samples $W_{l,k}$ are independent zero-mean random variables and the magnitude of the long training symbols is one. Hence, the second term in Equation (3.44) is a zero-mean random variable with the same variance as the individual noise samples

The contents of the two long training symbols (64 samples each) are identical, so averaging them can improve the quality of channel estimate. Moreover, because the DFT is a linear operation, the average can be computed before the DFT. Then only one DFT operation is needed to calculate the channel estimate. This technique is simple to implement; however it fails to take into account the correlation in the channel estimates.

2. Time Domain Approach

The channel estimation can also be performed using the time domain approach, as described in [9]. In this case, the channel impulse response (CIR) is estimated.

The received time domain signal during the two training symbols is

$$r_{l,n} = h \otimes x_n + w_{l,n}, \tag{3.45}$$

where $\otimes$ denotes circular convolution, x_n is the transmitted signal, h is the CIR and $w_{l,n}$ is AWGN.

The circular convolution can be expressed as a matrix vector multiplication [26] :

$$\mathbf{r} = \mathbf{X}\mathbf{h} + \mathbf{w}, \tag{3.46}$$

where

$$\mathbf{X}=\begin{bmatrix} x_1 & x_{64} & \cdots & x_{64-L+2} \\ x_2 & x_1 & \cdots & x_{64-L+3} \\ \vdots & & \ddots & \vdots \\ x_{63} & x_{62} & \cdots & x_{64-L} \\ x_{64} & x_{63} & \cdots & x_{64-L+1} \end{bmatrix},\quad \mathbf{h}=\begin{bmatrix} h_1 \\ h_2 \\ \vdots \\ h_{L-1} \\ h_L \end{bmatrix},\quad \mathbf{w}=\begin{bmatrix} w_1 & w_2 & \cdots & w_{64} \end{bmatrix}^T. \tag{3.47}$$

The CIR estimate can then be formed as

$$\begin{aligned} \hat{h} &= \frac{1}{2}X^{\dagger}\left(r_{1,n}+r_{2,n}\right) \\ &= \frac{1}{2}X^{\dagger}\left(Xh+w_{1,n}+Xh+w_{2,n}\right) \\ &= X^{\dagger}Xh+\frac{1}{2}X^{\dagger}(w_{1,n}+w_{2,n}) \\ &= h+\frac{1}{2}X^{\dagger}(w_{1,n}+w_{2,n}), \end{aligned} \tag{3.48}$$

where $X^{\dagger}$ denotes Moore-Penrose [27] generalized inverse of *X*. The channel transfer function (CTF) is then computed by

$$\hat{H}_k = \mathrm{DFT}\left\{\hat{h}\right\}. \tag{3.49}$$

3. Simulation and Results

An OFDM-based IEEE 802.11a system was simulated in a $K=16$ taps delay spread channel having an exponential power delay profile. The parameters of the OFDM are as per the IEEE 802.11a standard with a bandwidth of 20 MHz divided into $K=64$ subcarriers yielding a sub-carrier frequency spacing $f_{sc}=312.5\text{ kHz}$. To make the sub-channels orthogonal, the OFDM symbol duration is $1/f_{sc}=3.2\ \mu\text{s}$. An additional 0 0.8 μs is used as guard interval, i.e., CP of $L=16$. The channel estimation was done using the frequency domain and the time domain approaches.

Figure 32 illustrates the performance of each algorithm in terms of the Normalized Mean Square Error (NMSE) given by:

$$\text{NMSE} = \frac{\sum_{k=0}^{K-1} \left| \hat{H}_{n,k} - H_{n,k} \right|^2}{\sum_{k=0}^{K-1} \left| H_{n,k} \right|^2} \tag{3.50}$$

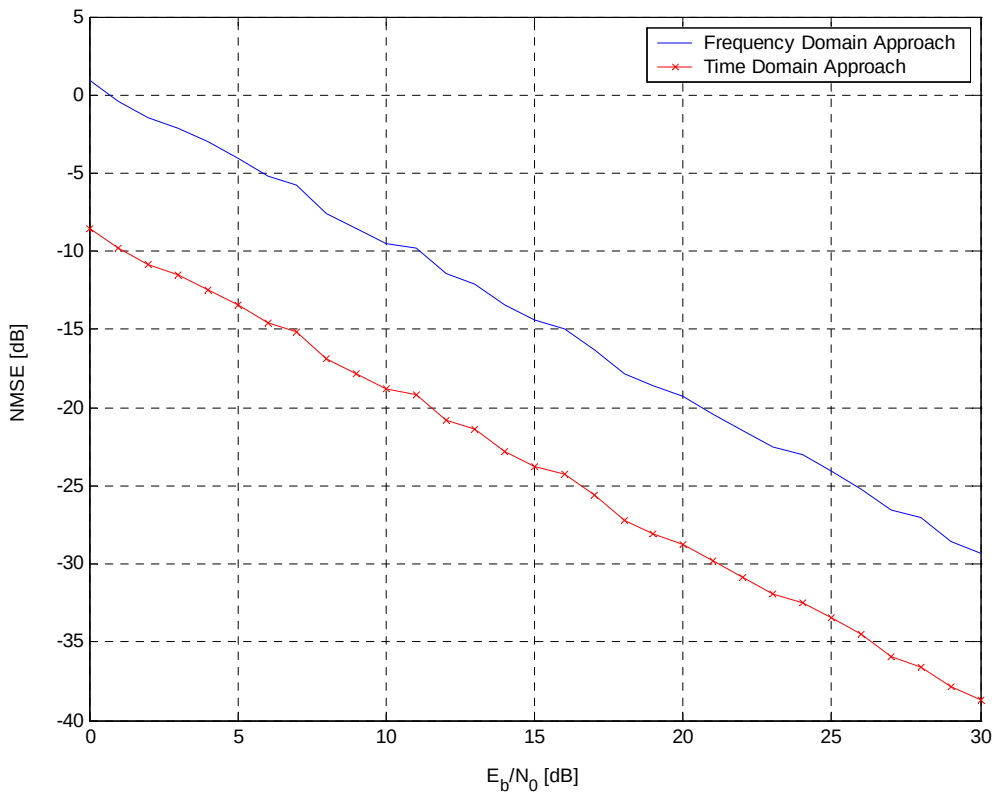

Figure 32. Performance Comparison of Channel Estimation Algorithms

The NMSE of the time-domain method is 5.0 dB better than the frequency-domain method. The rationale is that the frequency domain-estimator has to simultaneously estimate all the subcarriers, whereas the time-domain method estimates only the taps of the CIR. For example, in the IEEE 802.11a system the number of subcarriers used is 52, and the maximum length of the channel can be assumed to be less than the CP length, i.e., less than 16 taps. In the time-domain algorithm, windowing only the required first 16 channel-estimates helps zero-out the noise from the rest samples, and thus results in better performance. The drawback of the time-domain approach is that additional computations are required. This is the usual engineering trade-off; better performance usually implies higher costs in one form or another.

I. EQUALIZATION

Let the transmitted OFDM signal be s_n. Then the received signal r_n is

$$r_l = h_m \otimes s_n + w_l \qquad l = m + n - 1, \tag{3.51}$$

where h_m is the channel's impulse response, w_l is complex additive white Gaussian noise and $\otimes$ denotes circular convolution. The length m of the CIR was assumed to be less than the length of the cyclic prefix. Thus, the equivalent received signal in the frequency domain can be written as

$$R_k = H_k S_k + W_k, \tag{3.52}$$

where the convolution property of the DFT transform was applied. If an estimate of the channel's transfer function $\hat{H}_k$ is available at the receiver, then the equalized signal is obtained by a simple division in the frequency domain, i.e.,

$$R_{k,eq} = \frac{R_k}{\hat{H}_k} = \frac{H_k}{\hat{H}_k} S_k + \frac{W_k}{\hat{H}_k}. \tag{3.53}$$

In practical systems, the equalizer does not perfectly invert the effects of the channel and there is always some residual error. Additionally, the division by the channel estimates enhances the noise amplitude in some samples [13].

Hence, equalization in OFDM systems is subject to the same impairments as the single carrier system. Yet, the complexity of the equalizer for the OFDM system is substantially less than for the single-carrier system. The reason is that OFDM systems employ a bank of single-tap equalizers while single carrier systems employ multi-tap equalizers. Furthermore, the complexity of the equalizer grows as the square of the number of taps.

J. SUMMARY

The very important issue of synchronization in the receiver was covered in this chapter. Under the quasi-stationary channel assumption, most of the synchronization is performed during the preamble and need not be changed during the packet. The short training sequence is used for packet detection, symbol-time synchronization, and carrier

frequency-offset correction. The long training sequence is used for channel estimation. We demonstrated various synchronization and channel-estimation algorithms, simulating their performance in AWGN and multipath fading channels. Finally a brief discussion for phase tracking was provided, which is a mandatory step for OFDM systems employing coherent modulation schemes. In IEEE 802.11a systems, four pilot subcarriers are included in each OFDM symbol for pilot-phase tracking.

In the next chapter, we discuss the encoding process of a PLCP PPDU frame for the OFDM PHY and evaluate the performance of the IEEE 802.11a system in various operating modes.

THIS PAGE INTENTIONALLY LEFT BLANK

IV. PERFORMANCE OF IEEE 802.11A

A. OVERVIEW OF THE PPDU ENCODING PROCESS

The OFDM of the IEEE 802.11a standard system provides a Wireless LAN with data payload communication capabilities of 6, 9, 12, 18, 24, 36, 48 and 54 Mbps. The support of transmitting and receiving at data rates of 6, 12, and 24 Mbps is mandatory in the standard. The system uses 52 subcarriers that are modulated using binary or quadrature phase shift keying (BPSK/QPSK), 16-Quadrature Amplitude Modulation (QAM), or 64-QAM. Forward Error Correction (FEC) coding (convolutional coding) is used with a coding rate of 1/2, 2/3, or 3/4 [19]. A simplified block diagram of the IEEE 802.11a baseband transducer is illustrated in Figure 33.

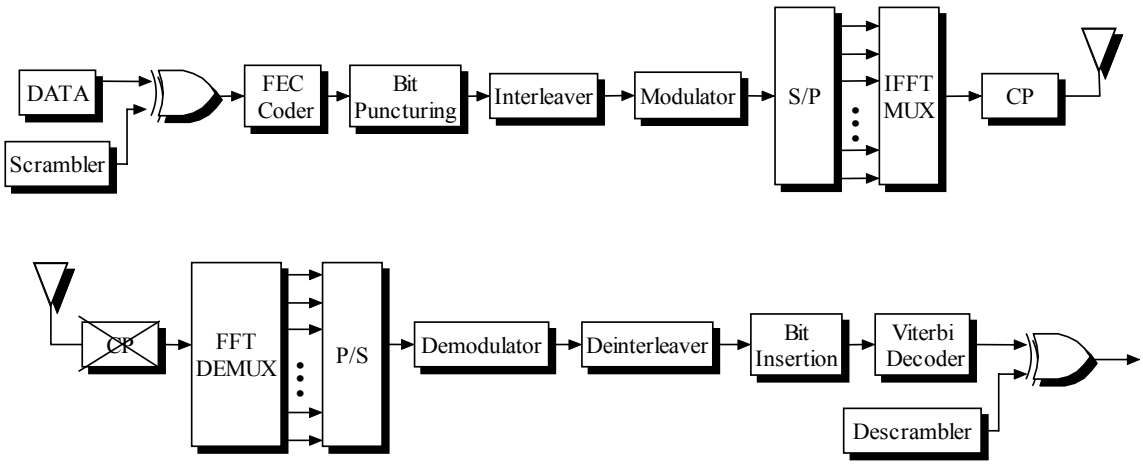

Figure 33. Simplified Block Diagram of the IEEE 802.11a Transceiver (After Ref. [19].)

At the transmitter, a length-127 pseudo-random sequence is used to scramble the data. (The purpose of the scrambler is to prevent a long sequence of ones or zeros.) The scrambled data is encoded with a $R = 1/2$ convolutional encoder. The other coding rates are achieved by puncturing the output of the FEC coder. Next, the coded bits are interleaved to prevent error bursts from being fed into the Viterbi decoder. The interleaved bits are divided into groups of q bits, where $q = \log_2(M)$ is defined by the modulation alphabet. Each bit-group is converted into a complex number according to the modulation encoding tables [19]. The complex numbers are fed into a serial-to-parallel converter (S/P) to form groups of 48 complex numbers. In each group, the complex numbers are

mapped into OFDM subcarriers. Four subcarriers are inserted as pilots, thus the number of used subcarriers per OFDM symbol is 52. Each OFDM symbol is converted to the time domain using Inverse Fast Fourier Transform (IFFT). A cyclic prefix (CP) is added to the Fourier-transformed waveform to eliminate ISI. Finally, the resulted periodic waveform is truncated to a single OFDM symbol length by applying time domain windowing and all the OFDM symbols are appended, one after another.

The receiver performs the inverse operations of the transmitter in reverse order.

B. SIMULATION TOOL OVERVIEW

In order to evaluate the performance of the IEEE 802.11a Physical layer under various operational modes, a simulation tool was necessary. For that reason, we built a Graphical User Interface (GUI) in Matlab. A snapshot of the GUI is illustrated in Figure 34.

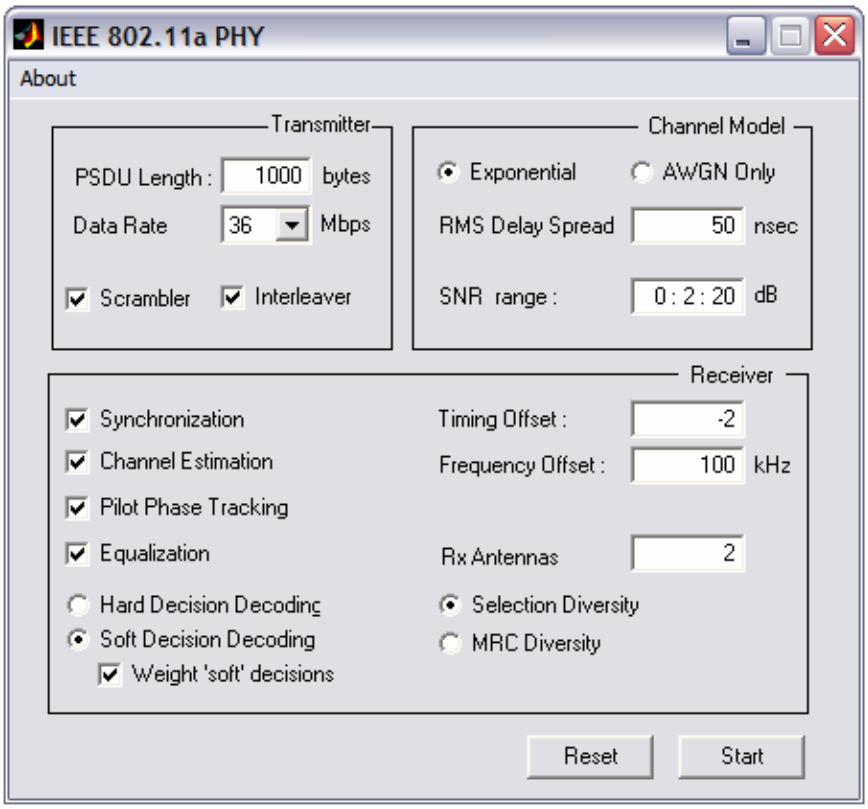

Figure 34. Snapshot of Graphical User Interface

The user selects the operational mode and the performance of the IEEE 802.11a is evaluated by Monte-Carlo simulation. A typical number for PSDU length is 1000 bytes. The number of simulated PPDU frames changes dynamically in order to get accurate results, with a minimum of 50 packets. It needs to be stated that [19] defines the simulated length of the packet to be at least 16 OFDM symbols long and the test to be performed over at least 20 packets.

A block diagram of the main function of the simulation is depicted in Figure 35.

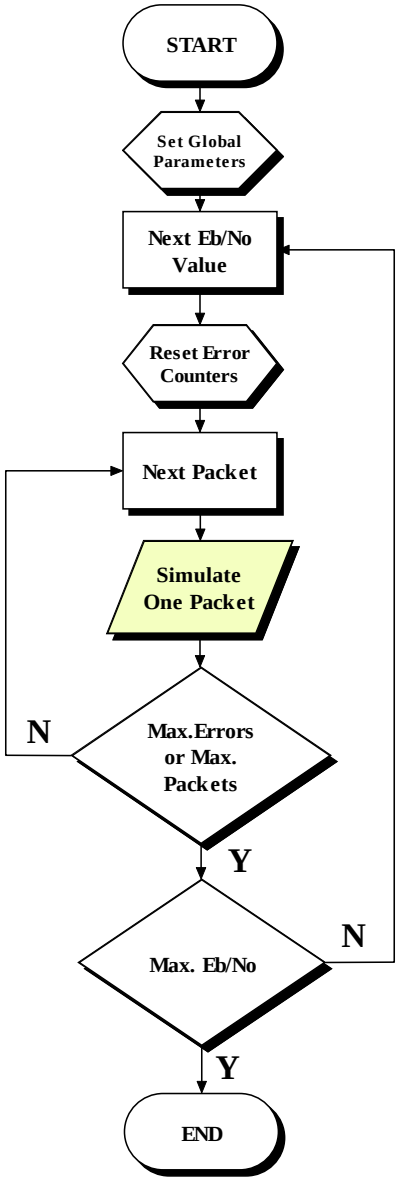

Figure 35. Block Diagram of the Main Function

For speed optimization purposes, the user application data and the system parameters are stored as global structures. The PREAMBLE and the SIGNAL field are also included in these structures, since these fields are defined explicitly by the user and system parameters. Then the simulation runs iteratively for one packet until the predefined number of errors or the maximum packets are reached. The outer loop iterates for the desired E_b/N_0 range.

A modular design approach was adopted in this software. Hence, for the simulation of one packet, three parent functions are involved:

- *transmitter.m*
- *channel.m*
- *receiver.m*

Each parent function consists of child sub-functions, according to the block diagram of Figure 33. The Matlab code is not included in the thesis. For those interested, please contact the author (msegkos@hotmail.com) or Dr. T. Ha.

C. TRANSMITTER

The PSDU is generated by a pseudo-random bit generator. Then the PSDU is appended to the SERVICE field, and the resultant bit string is extended with *tail* and *pad* bits [19] to form the DATA part of the packet.

1. PLCP DATA Scrambler

The DATA field is scrambled with a length-127 frame-synchronous scrambler. The frame synchronous scrambler uses the following generator polynomial [19]:

$$S(x) = x^7 + x^4 + 1. \tag{4.1}$$

The purpose of the scrambler is to prevent a long sequence of ones or zeros. This helps with the timing synchronization at the receiver. Besides that, the remaining functions in the transceiver are unaffected by the scrambling operation. The 127 maximal length sequence generator is illustrated in Figure 36.

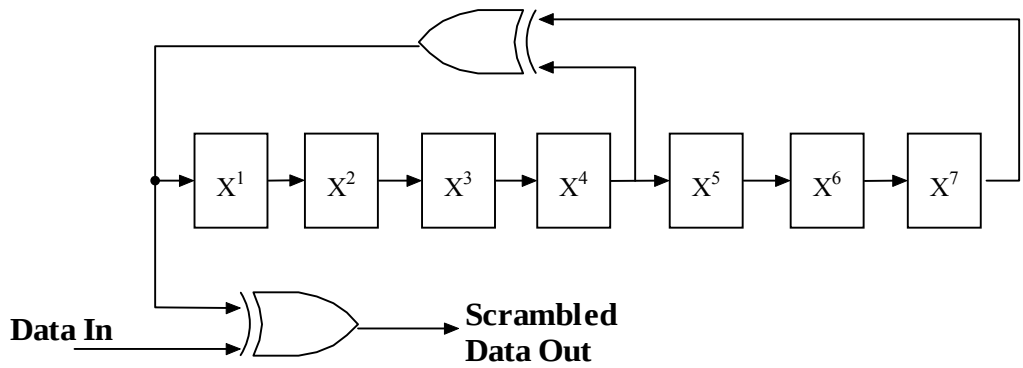

Figure 36. Frame Synchronous Scrambler/Descrambler (After Ref. [19].)

The seven least significant bits of the DATA are be set to zero prior to scrambling to enable estimation of the initial state of the descrambler at the receiver.

2. Convolutional Encoder

The scrambled data sequence is encoded with the industry's standard $[133_8\ 171_8]$ generator polynomials [19], of rate $R = 1/2$ and constraint length $K = 7$, as depicted in Figure 37.

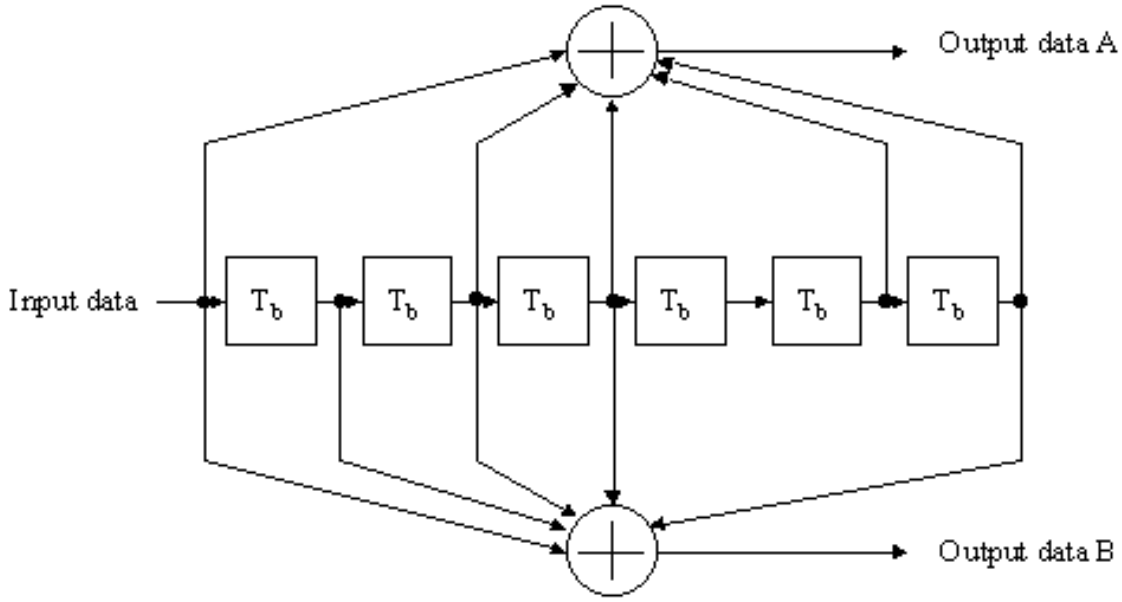

Figure 37. Convolutional Encoder of IEEE 802.11a (From Ref. [19].)

3. Bit Puncturing

The coding rate of the convolutional encoder is $R = 1/2$. Higher rates are achieved by puncturing the output of this encoder. Puncturing involves deleting coded bits from the output data sequence. The bits that are not transmitted are defined by a *puncturing pattern.* Figure 38 shows the two different puncturing patterns of IEEE 802.11a for the coding rates $R = 2/3$ and $R = 3/4$ respectively.

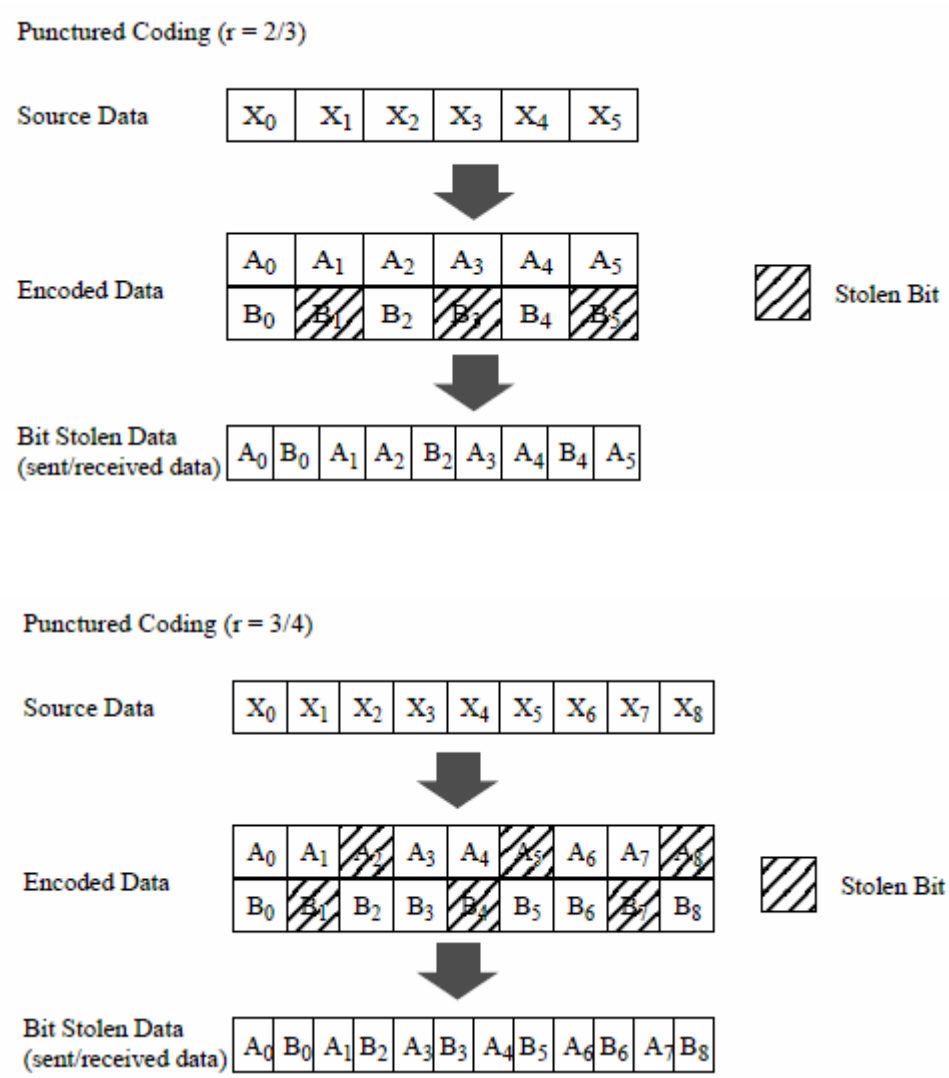

Figure 38. Bit Puncturing Pattern in the IEEE 802.11a (After Ref. [19].)

The puncturing pattern for the rate $2/3$ code has a period of 4 bits, and the fourth bit is omitted. Thus the puncturing rate is $3/4$ and the overall code rate is $1/2 \cdot 4/3 = 2/3$.

The puncturing pattern for the rate $3/4$ code has a period of six bits, and bits 3 and 4 are punctured from each period. Hence the puncturing rate is $2/3$ and the overall coding rate is equal to $1/2 \cdot 3/2 = 3/4$.

The increase in the coding rate decreases the free distance of the code, but usually the resulting free distance is very close to the optimum one that is achieved by specifically designing a convolutional code for the punctured rate [28]. Table 5 illustrates the free distances and the asymptotic coding gains of the three code rates used in the IEEE 802.11a. The optimum rate $3/4$ and $2/3$ codes are also illustrated.

Code Rates	Punctured Free Distance	Punctured Coding Gain	Optimum Free Distance	Optimum Coding Gain
1/2	–	–	10	7.0 dB
2/3	6	6.0 dB	7	6.7 dB
3/4	5	5.7 dB	6	6.5 dB

Table 5. Free Distances of the Codes Used in IEEE 802.11a (After Ref. [28].)

The performance loss when using punctured codes instead of the optimum ones is very small. The table does not show the punctured free distance and coding gain values for rate $1/2$, as it is naturally the optimum code.

Similarly, depuncturing in the receiver is done by inserting dummy bits into the locations that were punctured in the transmitter. The values of the dummy bits depend on whether the system uses hard or soft decision decoding. When the Viterbi algorithm is used for decoding, the zero-valued dummy bit does not have any effect on the outcome of the decoder.

4. Interleaver

All encoded data bits are interleaved by a block interleaver. Block interleaving operates on one block of bits at a time. The number of bits in the block is called *inter-*

leaving depth which defines the delay introduced by interleaving [28]. The interleaving depth in the IEEE 802.11a standard has been selected to be equal to the number of bits in a single OFDM symbol, N_{CBPS}. The interleaver is defined by a two-step permutation [19]. The first permutation ensures that neighboring coded bits are mapped into nonadjacent subcarriers. The second ensures that adjacent coded bits are mapped alternately onto more and less significant bits of the constellation and, hence, long runs of low significant bits are avoided.

The performance effect of interleaving in IEEE 802.11a is a consequence of frequency diversity. WLAN systems are wideband applications, therefore usually experience frequency selective fading. This is an essential requirement to be able to exploit frequency diversity [16]. The interleaving depth is only one symbol because the channel is assumed to be quasi-stationary, i.e., the channel does not change during the transmitted packet. When the channel is in a deep fade, it will remain so for the duration of the packet. Hence, no additional diversity gain can be achieved by interleaving in time. Additionally, increasing the interleaving depth increases the delay of baseband processing. It has to be noted that the maximum possible delay is constraied by the IEEE 802.11 MAC protocol. The acknowledgement packet Short Inter-Frame Spacing (SIFS) timing requirement is equal to $16\ \mu s$, therefore after the packet ends, the processing has to be completed in less time [9].

The performance of the IEEE 802.11a 12-Mbps mode with and without interleaving is illustrated in Figure 39. The channel model was exponential with rms delay spread 75 ns. Figure 40 also shows the Packet Error Rate (PER) in the same operational mode. The effect of interleaving is more striking for Packet Error Rate: at $\mathrm{PER} = 10^{-2}$, the gain from interleaver is approximately 5 dB. Additionally, the slope of the curve is steeper with interleaving; this is a consequence of the frequency diversity gain achieved.

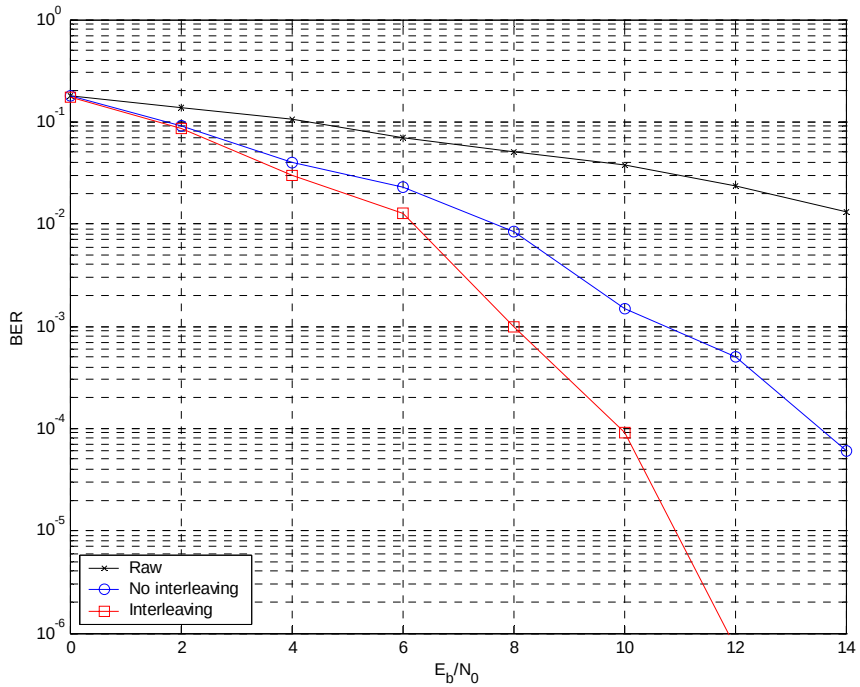

Figure 39. Bit Error Rate of IEEE 802.11a 12-Mbps Mode with and without Interleaving in 75-ns RMS Delay Spread Fading Channel

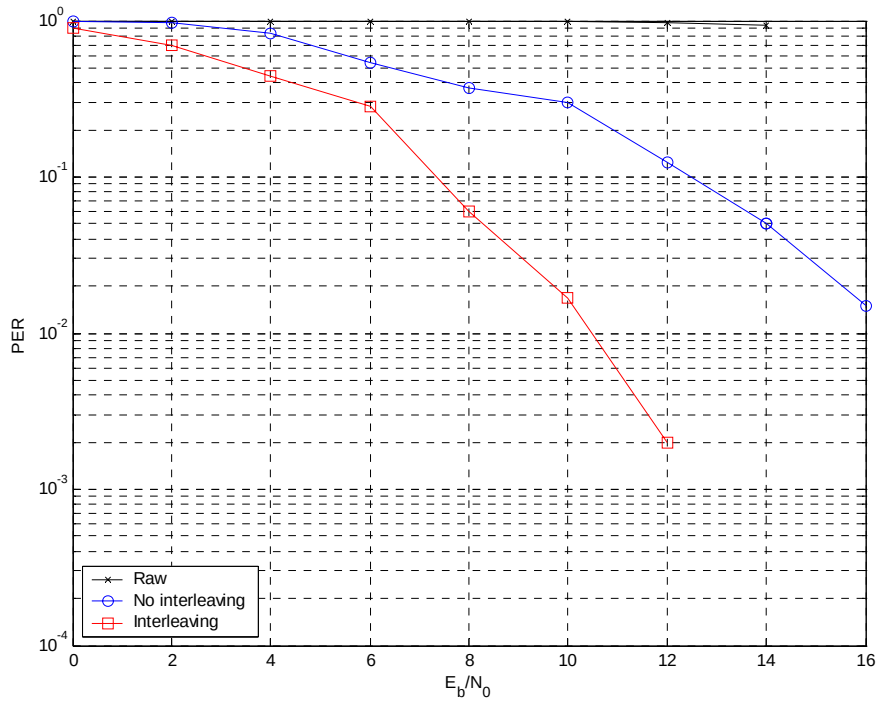

Figure 40. Packet Error Rate of IEEE 802.11a 12-Mbps Mode with and without Interleaving in 75-ns RMS Delay Spread Fading Channel

5. Modulation Mapping

The encoded and interleaved binary serial input data is divided into groups of q bits, where q is the number of bits per symbol. These groups are converted into complex numbers representing BPSK, QPSK, 16-QAM, or 64-QAM constellation points. The conversion is performed according to Gray-coded constellation mappings, as defined in [19]. Figure 41 illustrates the constellation mapping for 64-QAM. We observe that adjacent symbols differ only by one bit.

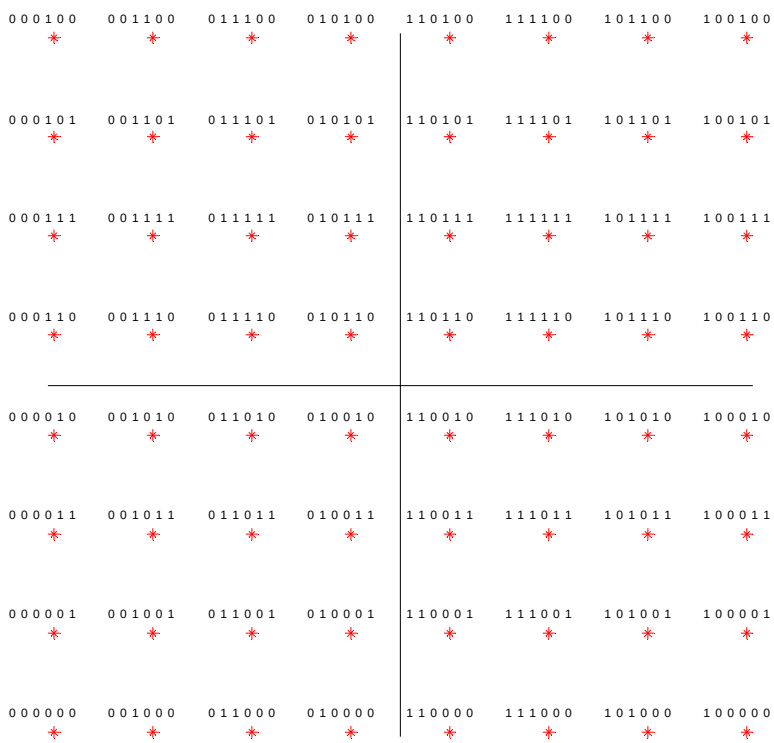

Figure 41. 64-QAM Constellation Bit Encoding

For 64-QAM, $b_0 b_1 b_2$ determines the I value, and $b_3 b_4 b_5$ determines the Q value. The output values $I + jQ$ are normalized by a normalization factor, as defined in [19].

The normalization factor K_{mod} depends on the base modulation mode, as depicted in Table 6.

Modulation	K_{MOD}
BPSK	1
QPSK	$1/\sqrt{2}$
16-QAM	$1/\sqrt{10}$
64-QAM	$1/\sqrt{42}$

Table 6. Modulation-dependent Normalization Factor K_{MOD}

6. OFDM Multiplexing

The common way to implement the Inverse Discrete Fourier Transform (IDFT) is by an Inverse Fast Fourier Transform (IFFT) algorithm. The mapping is illustrated in Figure 42.

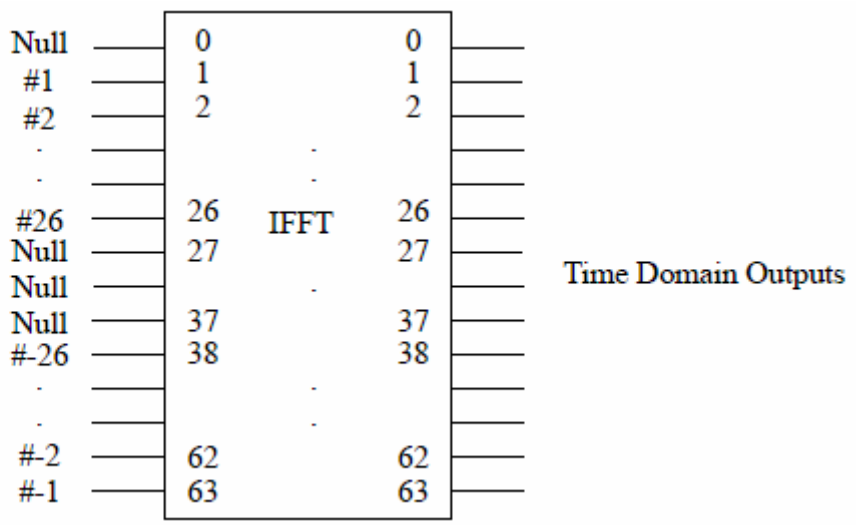

Figure 42. Inputs and Outputs of IFFT (From Ref.[19].)

The coefficients 1 to 26 are mapped to the same numbered IFFT inputs, while the coefficients –26 to –1 are mapped to IFFT inputs 38 to 63. The rest of the inputs, 27 to 37 and the 0 (dc) input, are set to zero.

In each OFDM symbol, four of the subcarriers are dedicated to pilot signals in order to make coherent detection robust against frequency offset and phase noise, as dis-

cussed in Chapter III. The pilot signals are mapped to subcarriers –21, –7, 7 and 21. The polarity of the pilots is controlled by a pseudo-binary sequence to prevent the generation of spectral lines. This sequence can be generated by the scrambler, when the *all ones* initial state is used, and by replacing all *bit 1's* with –1 and all *bit 0's* with 1. The first element multiplies the pilot subcarriers of the SIGNAL symbol, while the rest of the elements are used for the DATA symbols.

After performing an IFFT, the output is cyclically extended to the desired length to form the guard interval. Then the SIGNAL symbol and the DATA symbols are appended to the PLCP PREAMBLE to form the packet. An example of the transmitted packet is illustrated in Figure 43.

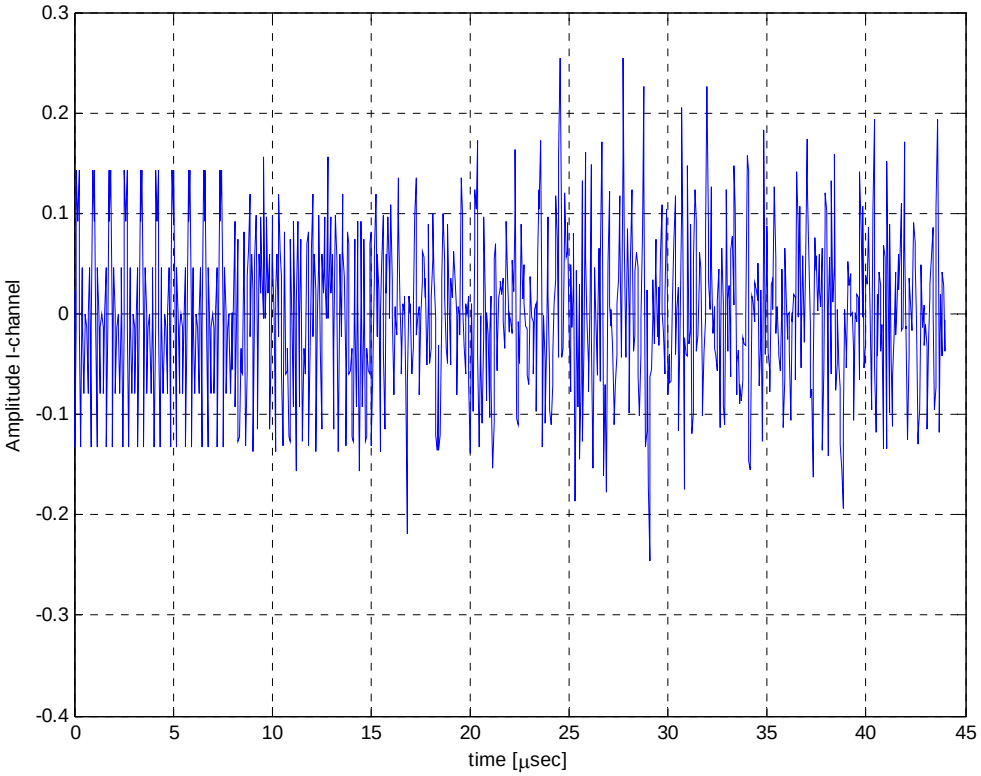

Figure 43. Time Domain Representation of the Transmitted Packet

The periodic nature of the preamble is obvious. The packet length was 100 bytes and the data rate was 36 Mbps. The SIGNAL field starts at $t = 16\ \mu s$, while the DATA field starts at $t = 20\ \mu s$.

The power spectrum of the transmitted baseband packet is depicted in Figure 44.

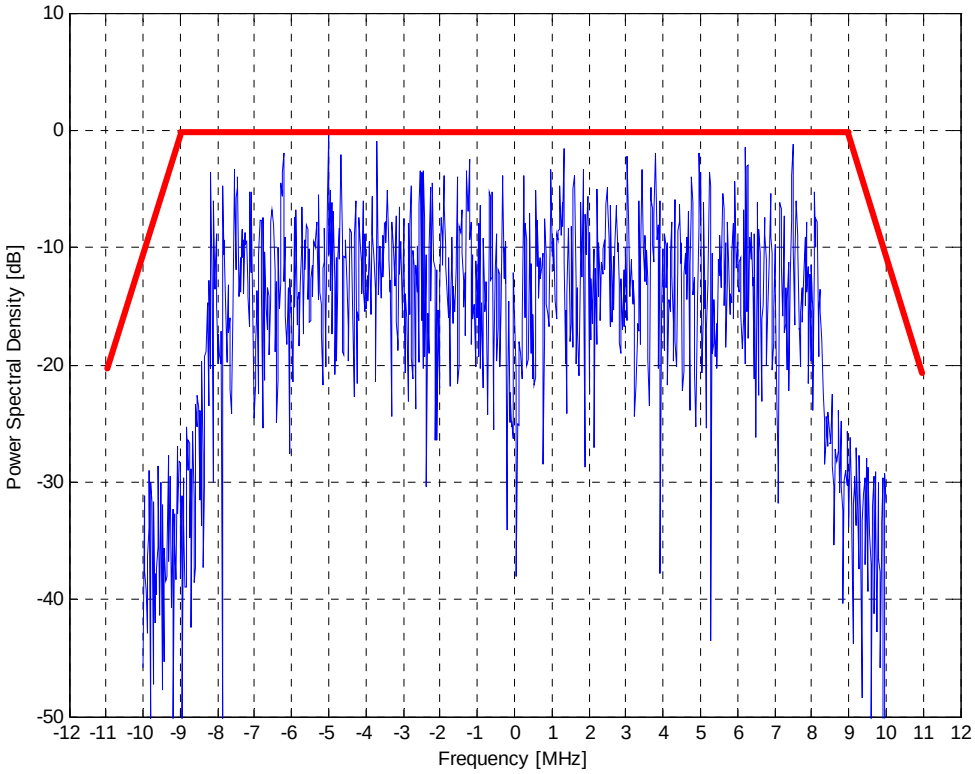

Figure 44. PSD of the Transmitted Packet

The transmit spectrum mask, as defined in [19], is indicated by the red line. In particular, the average energy of the constellations in each of the spectral lines $-16...-1$ and $+1...+16$ must deviate no more than ± 2 dB from their average energy. The average energy of the constellations in each of the spectral lines $-26...-17$ and $+17...+26$ must deviate no more than the $+2/-4$ dB from their average energy. We observe that the transmitted spectrum has a 0-dB bandwidth that does not exceed 18 MHz.

D. RECEIVER

The functional block-diagram of the receiver is depicted in Figure 45, in which the extra blocks are yellow colored..

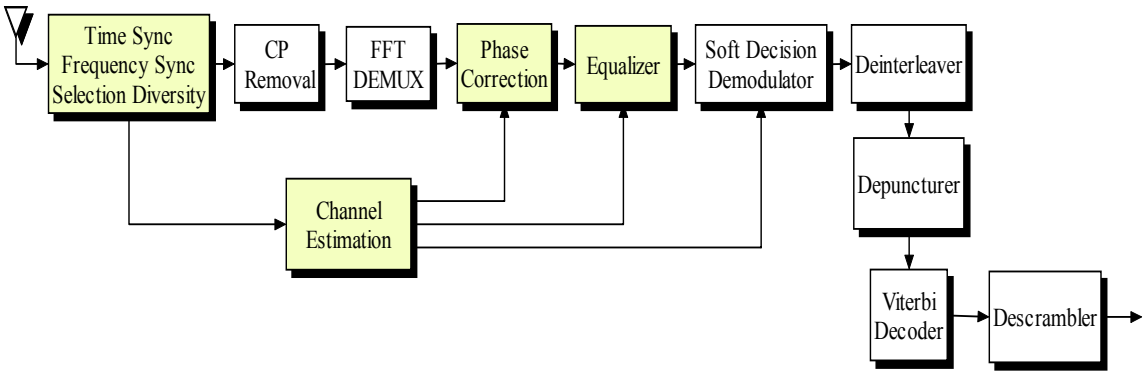

Figure 45. Baseband Receiver Functional Block Diagram

Before any receiver algorithms can be employed, the timing must first be recovered; that is, the system clock at the receiver must become synchronized with the transmitter's clock, while taking into account the propagation delay across the channel. Since OFDM is a frequency domain modulation technique, it is essential to have accurate estimates of the frequency offset, caused by oscillator instability, at the receiver. The accuracy of the channel estimation algorithm is also crucial to the overall system's performance. The phase correction algorithm uses the pilot subcarriers to correct the rotation of the OFDM symbols. This rotation was introduced by the residual frequency offset of the carriers.

The equalization is a necessary step to recover the distorted signal, due to multipath fading. Then the signal is demodulated using a *soft decision* demodulator, that is, the demodulated bits retain additional information about the reliability of the decision. To include this extra information, the soft bits have different values: a large absolute value for the first bit and a small value for the second bit. In our simulation, the sign of the soft decision indicates a 0 or 1 bit. The absolute value of each soft decision is the distance to the decision boundary. This additional information can greatly improve the performance of channel coding schemes [28].

A hard decision demodulator can also be used. This modulation type is essentially a maximum-likelihood decision in the constellation point that is closest to the received symbol [7]. The hard decisions are the bits assigned to that constellation point.

The demodulated soft decision bits are fed to the deinterleaver, which performs the opposite operation of interleaving. Dummy bits, also known as *erasures,* are inserted into the locations that were punctured in the transmitter. The values of the erasures depend on whether the system uses hard or soft decisions, as described in [28]. A hard decision system inserts randomly one and zero bits into the punctured locations. A soft decision receiver should insert a soft decision value of zero. For the usual case of decoding with the Viterbi algorithm, the zero-valued dummy bit does not have any effect on the outcome of the decoder.

The bit string with the erasures is fed into the Viterbi decoder, which is a maximum-likelihood symbol estimator [29]. The Viterbi algorithm can easily be implemented using either hard or soft decision demodulation. When the soft decision decoding is used, the channel frequency response estimates can enhance the performance of the Viterbi algorithm, as described in [9]. In particular, the path metrics p_n in the Viterbi algorithm are weighted by the squared channel amplitudes as follows:

$$p_n = \left|\hat{H}_k\right|^2 \left|\hat{b}_n - b_n\right|^2, \tag{4.2}$$

where $\hat{H}_k$ is the channel estimate of the *k* subcarrier, and $\left|\hat{b}_n - b_n\right|^2$ is the squared Euclidean distance between the soft decision $\hat{b}_n$ and the reference value b_n.

The performance effect of this weighting is significant in a fading channel. The reason is diversity; when the subcarrier is faded, its amplitude is small and therefore the path metric is scaled down to almost zero. In other words, the bits that were transmitted on deep faded subcarriers have very little impact on the decision of the Viterbi decoder.

Finally, the decoded bits are scrambled with the same 127-bit sequence, frame-synchronous scrambler used at the transmitter. The seven least-significant bits of the SERVICE field are used to estimate the initial state of the scrambler.

E. PERFORMANCE OF IEEE 802.11a IN AWGN

IEEE 802.11a provides eight different data rates from 6 Mbps to 54 Mbps with increasingly higher SNR required as the data rate increases. Figure 46 illustrates the effect of the additive white Gaussian noise to the constellation of the data subcarriers at the demodulator. The channel was AWGN with $\text{SNR} = 18$ dB. The selected data rate was 54 Mbps, that is 64-QAM modulation with $R = 3/4$ coding rate.

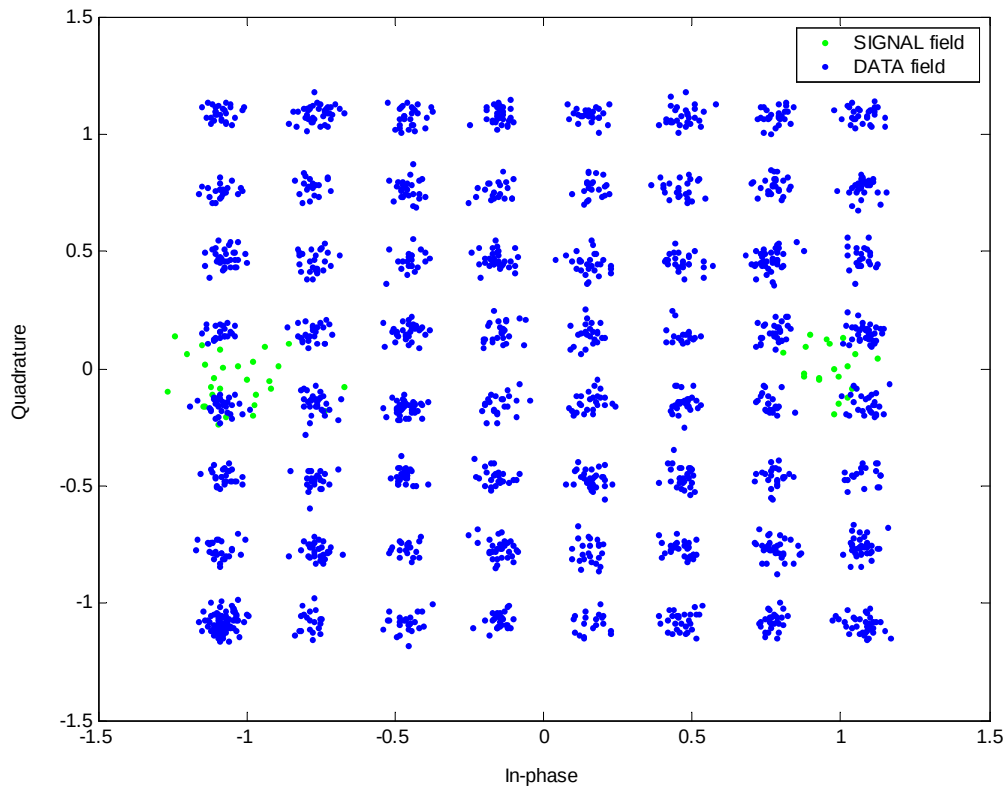

Figure 46. Subcarrier Constellation at the Demodulator $(\text{SNR} = 18 \text{ dB}, \text{ AWGN})$

The green dots indicate the constellation distortion of the SIGNAL symbol which is BPSK modulated. The blue dots indicate the DATA symbols.

In lower SNR the distortion increases and, when the symbols cross the decision boundaries, the correct demodulation is no longer possible. Thus, channel coding has to be used in order to increase performance. Figure 47 illustrates the impact of channel cod-

ing on the performance of IEEE 802.11a 54 Mbps mode when hard decision decoding (HDD) and soft decision decoding (SDD) is used.

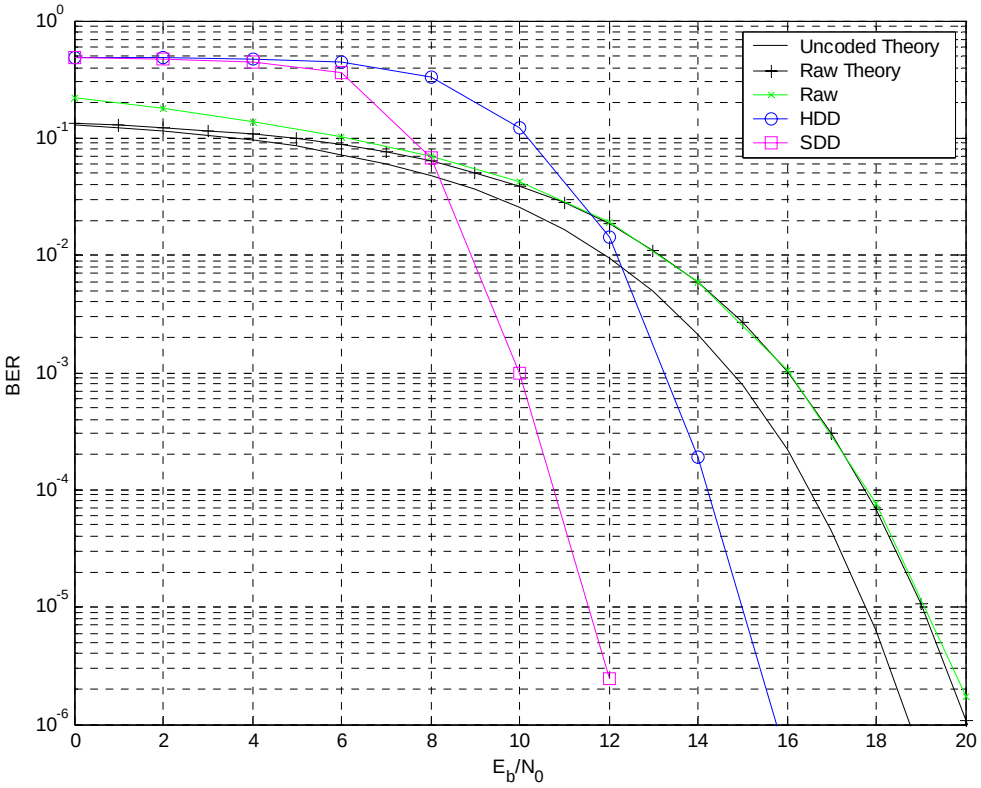

Figure 47. Coding Gain in BER of IEEE 802.11a 54-Mbps Mode, in AWGN

The coding gain is approximately 3 dB for HDD and 6 dB for SDD at 10^{-6} BER. It has to be noted that the raw (channel) BER is worse than uncoded BER by a factor of *R*, that is, $10\log_{10}(3/4) = 1.25$ dB

Figure 48 shows the coding gain in Packet Error Rate (PER) for the same configuration. IEEE 802.11a is a packet-oriented network, therefore a PER is the most commonly used measure of its performance.

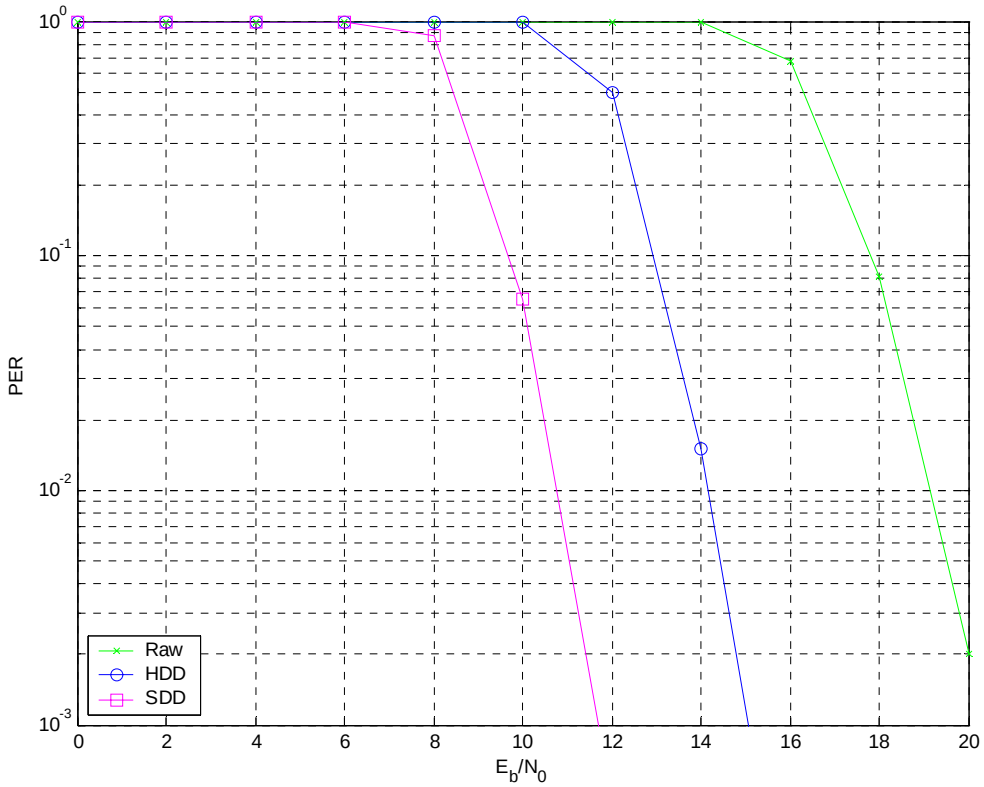

Figure 48. Coding Gain in PER of IEEE 802.11a 54-Mbps Mode, in AWGN

We observe that the effect of channel coding is most striking for PER. At 1% PER, the gain is 4 dB for HDD and nearly 7.5 dB for SDD. The reason is because even one bit in error causes a packet error in an uncoded system.

The previous examples of channel coding options show another important parameter of channel coding, namely the *coding rate.* Coding rate is the ratio of input bits to output bits from the encoder. This ratio is always less than one. To illustrate the effect of coding rate in the performance of channel coding, the BER and PER of IEEE 802.11a 48 Mbps mode was simulated in AWGN channel. This mode uses the same modulation, namely 64-QAM, but a different coding rate. The results are depicted in Figure 49 and Figure 50 respectively.

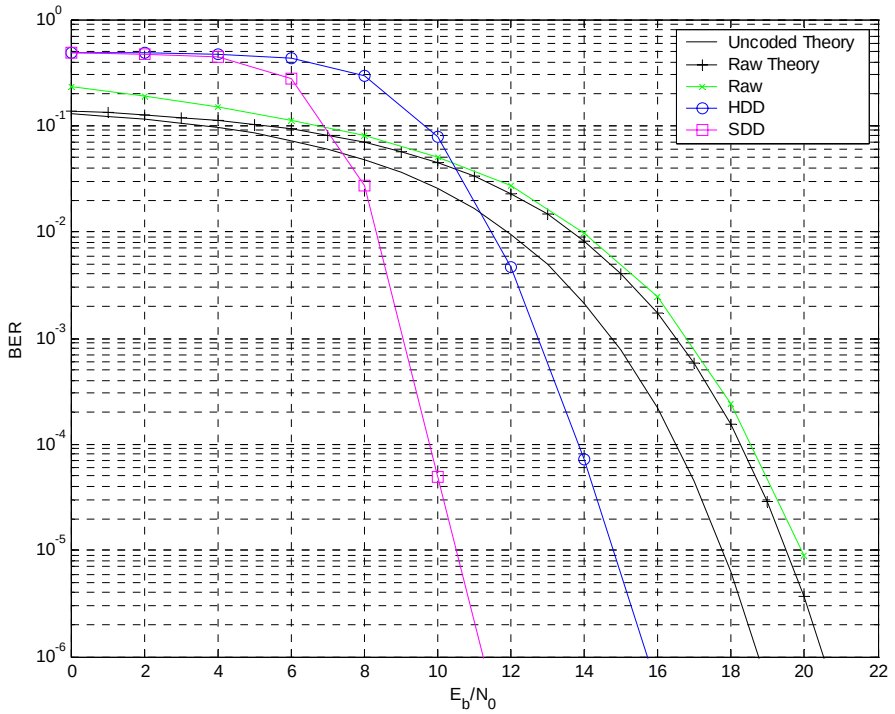

Figure 49. Coding Gain in BER of IEEE 802.11a 48-Mbps Mode, in AWGN

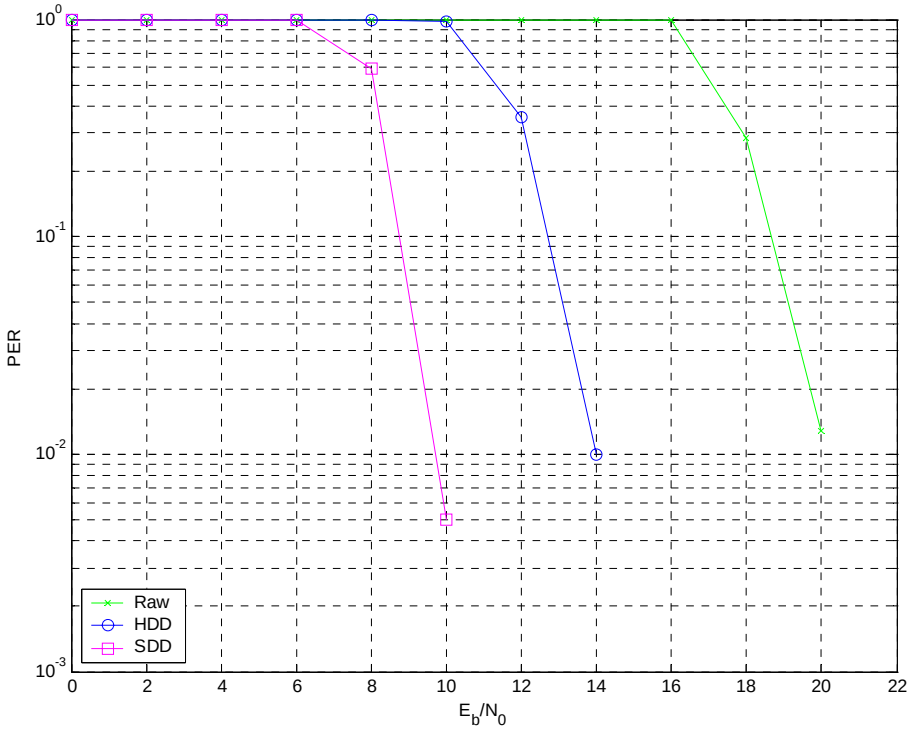

Figure 50. Coding Gain in PER of IEEE 802.11a 48-Mbps Mode, in AWGN

The coding rate for 48Mbps mode is $2/3$. This translates to 1.76 dB difference in uncoded and raw BER. Recall that for $R = 3/4$ the difference was 1.24 dB. However, the coding gain is roughly the same for HDD and increased by 0.5 dB for SDD.

Figure 51 illustrates the simulated BER for all operational modes of IEEE 802.11a in AWGN, when soft decision decoding is used.

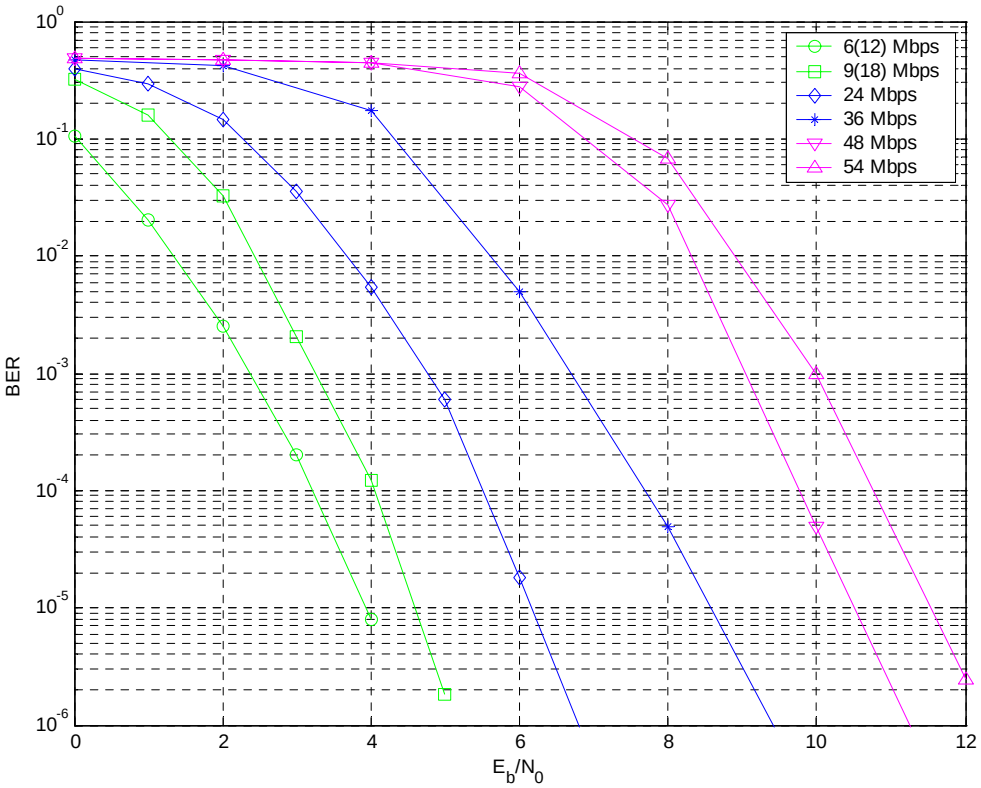

Figure 51. Performance Comparison of all IEEE 802.11a modes in AWGN and SDD

The 6-Mbps and 9-Mbps modes have the same performance as 12-Mbps and 18-Mbps modes, respectively, since BPSK and QPSK have the same performance in AWGN.

At $\text{BER} = 10^{-6}$, the highest data rate mode, that is 54 Mbps, requires 8 dB more than the lowest and most robust data rate mode of 6 Mbps.

Another way to interpret the SNR increase is to look at how the range of system changes with respect to the data rate used. As previously mentioned in Chapter II, the range depends on the path loss the transmitted signal experiences, as it travels through the channel medium. This relationship was shown to be

$$L_p \propto \frac{1}{d^c}. \tag{4.3}$$

As described in [5], the value of the path loss coefficient is dependent on the environment. The basic case is free space, where $c = 2$; in an indoor environment, a value of $c = 3$ can be used. Thus, every doubling of range decreases the signal power to:

- $1/4$ (or 6 dB) for free space and
- $1/8$ (or 9 dB) for indoor environment.

This implies that the range difference from 6 to 54 Mbps is about 2, when soft decision decoding is used at the receiver.

F. PERFORMANCE OF IEEE 802.11a IN MULTIPATH FADING

The theoretical performance of IEEE 802.11a under various types of multipath fading is well researched in previous theses, Ref. [30], for example. The general method relies on treating the energy per bit E_b as a random variable (e.g., Rayleigh, Ricean, Nakagami), computing the probability of error for one subcarrier as a function of E_b, and averaging all independent subcarriers. However, these approaches make an optimistic assumption about the number of independent subcarriers in the OFDM symbol. In [30], the coherence bandwidth B_c was defined as

$$B_c = \frac{1}{50\sigma_\tau}, \tag{4.4}$$

where σ_τ is the rms delay. Thus, using the typical values of σ_τ for small to large buildings, the range of values for coherence bandwidth becomes

$$167 \text{ kHz} \le B_c \le 667 \text{ kHz}. \tag{4.5}$$

Since the subcarrier spacing for IEEE 802.11a is 312.5 kHz, this implies B_c contains one to two subcarriers, that is, at least 24 subcarriers are independent.

In most applications however, the coherence bandwidth is defined as [5]

$$B_c = \frac{1}{5\sigma_\tau}, \tag{4.6}$$

which implies

$$1.67 \text{ MHz} \le B_c \le 6.67 \text{ MHz}, \tag{4.7}$$

thus the range of independent subcarriers is restricted from two to eight.

To illustrate the effect of fading, a simulation was run under perfect synchronization, using the exponential channel model with 50-ns rms delay spread. Figure 52 shows the constellation of the received data subcarriers for the 54-Mbps mode with 20-dB SNR.

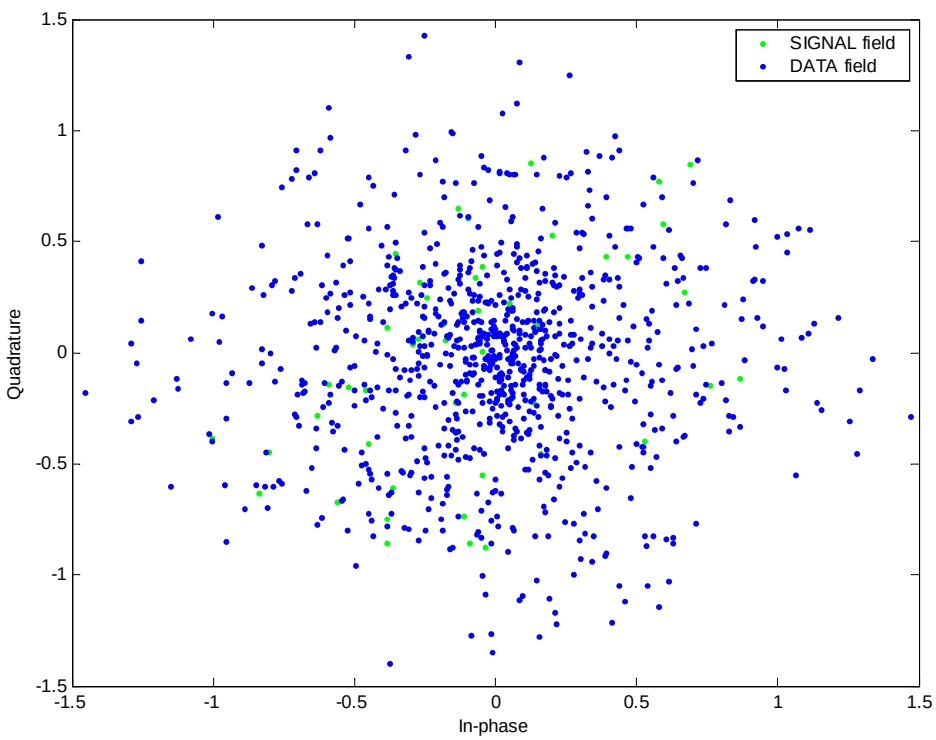

Figure 52. Subcarrier Constellation of IEEE 802.11a 54-Mbps mode at the Demodulator ($\text{SNR} = 20$ dB, 50-ns RMS Delay Spread.)

We observe that the signal constellation is severely distorted and thus a correct demodulation is no longer possible.

Intuitively, even with channel coding and perfect time and frequency synchronization, the bit error rate will be very high. Thus the signal must be equalized to mitigate the distortion caused by the channel. Figure 53 illustrates the constellation of data subcarriers after equalization has been applied at the receiver.

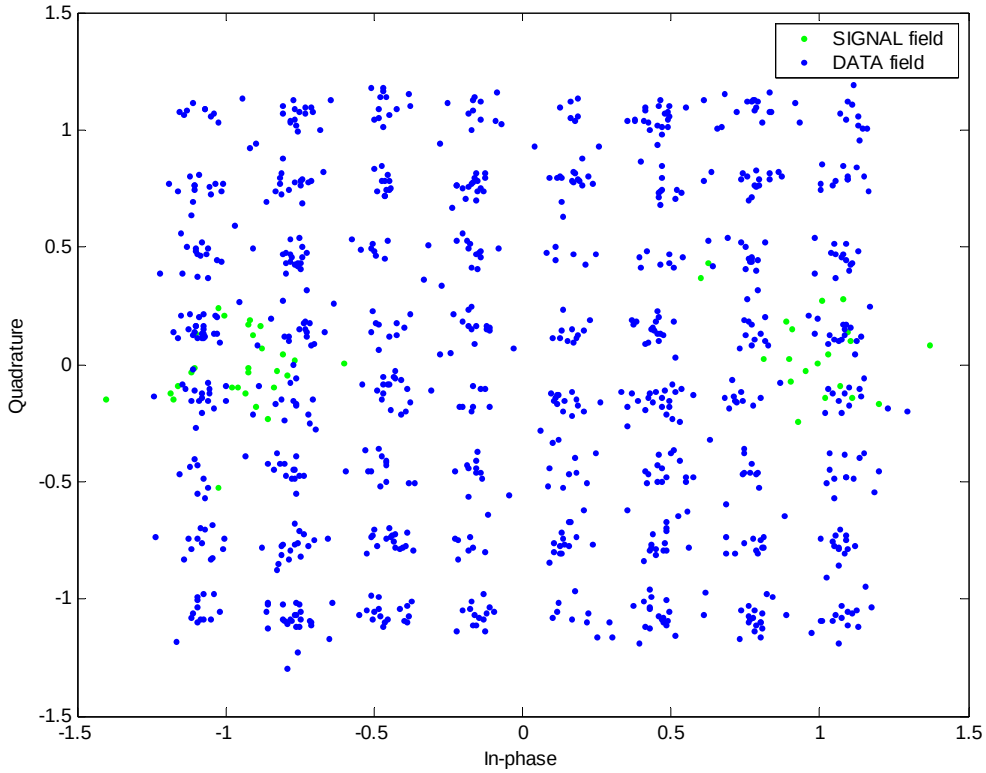

Figure 53. Equalized Subcarrier Constellation of IEEE 802.11a 54-Mbps Mode at the Demodulator ($SNR = 20$ dB, 50-ns RMS Delay Spread.)

Now we can recognize the familiar 64-QAM constellation; however, as a side-effect of equalization, some noise was amplified.

Further performance improvement can be accomplished if the soft decision bits at the output of the demodulator are weighted by the channel squared amplitudes, as we discussed earlier.

The performance of IEEE 802.11a 6-Mbps mode under a Rayleigh fading channel of 50-ns RMS delay spread is depicted in Figure 54.

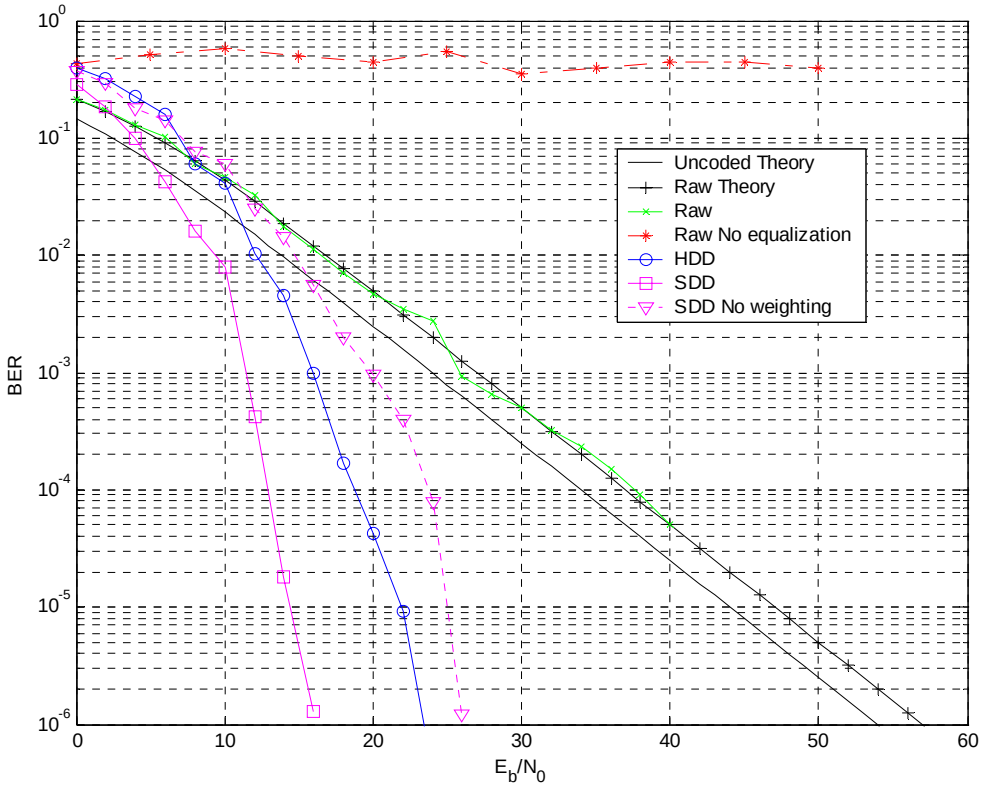

Figure 54. BER of IEEE 802.11a 6-Mbps Mode in Rayleigh Fading, 50-ns RMS Delay

We see that without equalization, even with the most robust data rate the signal cannot be recovered. We also observe that, at 10^{-6} BER, with hard decision decoding we have a coding gain of about 30 dB and with soft decision decoding the coding gain becomes 35 dB. Additionally, the performance of SDD without channel weighting is 10 dB worse than weighted soft decisions and even worse than HDD. The reason is because the equalization amplified some noise samples, leading to incorrect decisions at the Viterbi decoder.

Figure 55 illustrates the coding gain for BPSK/QPSK modulation and coding rates $1/2$ and $3/4$, in an exponential-decaying fading channel with 50-ns rms delay spread.

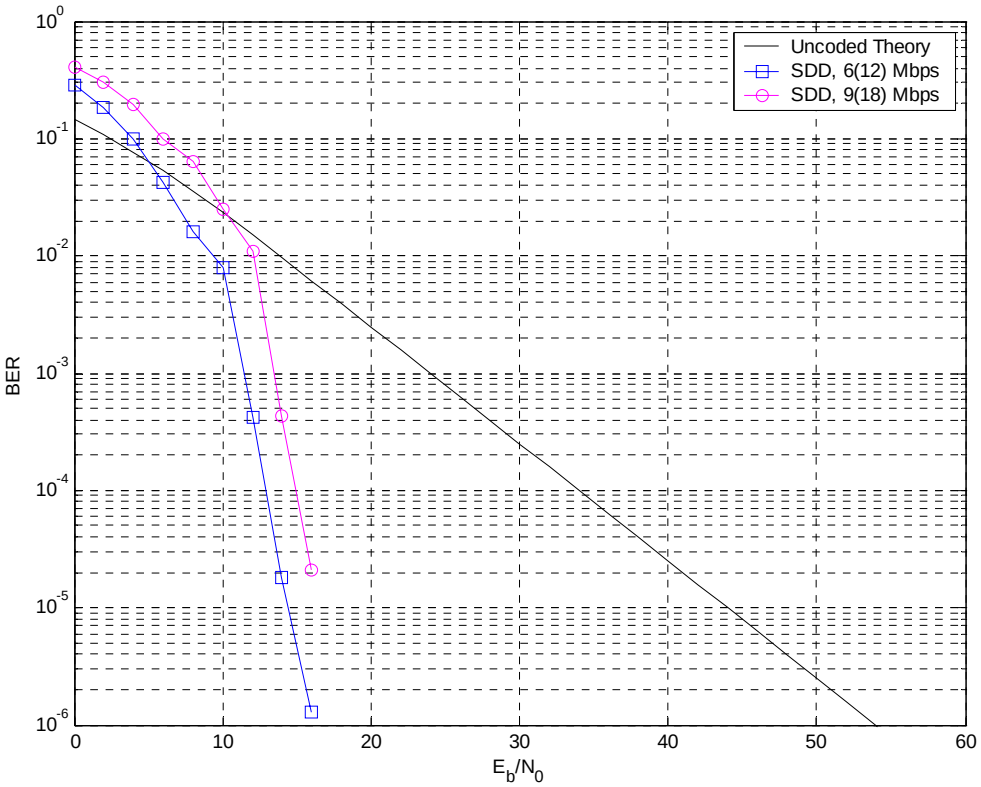

Figure 55. Performance of IEEE 802.11a BPSK/QPSK Modulation in an Exponential-decaying Channel, 50-ns rms Delay Spread

The performance of QPSK is identical to BPSK, as long as the coding rate is the same. In other words, the performance at 6 Mbps and 9 Mbps is identical to the performance at 12 Mbps and 18 Mbps, respectively.

From the above figure we observe that the performance of 9 (18) Mbps is 2 dB worse than 6 (12) Mbps. This is an expected outcome since the coding rate is increased from $1/2$ to $3/4$, the Hamming distance is decreased and thus the performance of the Viterbi decoder goes down. The coding gain at $\text{BER} = 10^{-6}$ is 36 to 38 dB.

The performance of IEEE 802.11a 16-QAM modulation for both available coding rates and weighted soft decision demodulation is shown in Figure 56. The channel characteristics were kept the same, that is, exponential-decaying channel with 50-ns rms delay spread.

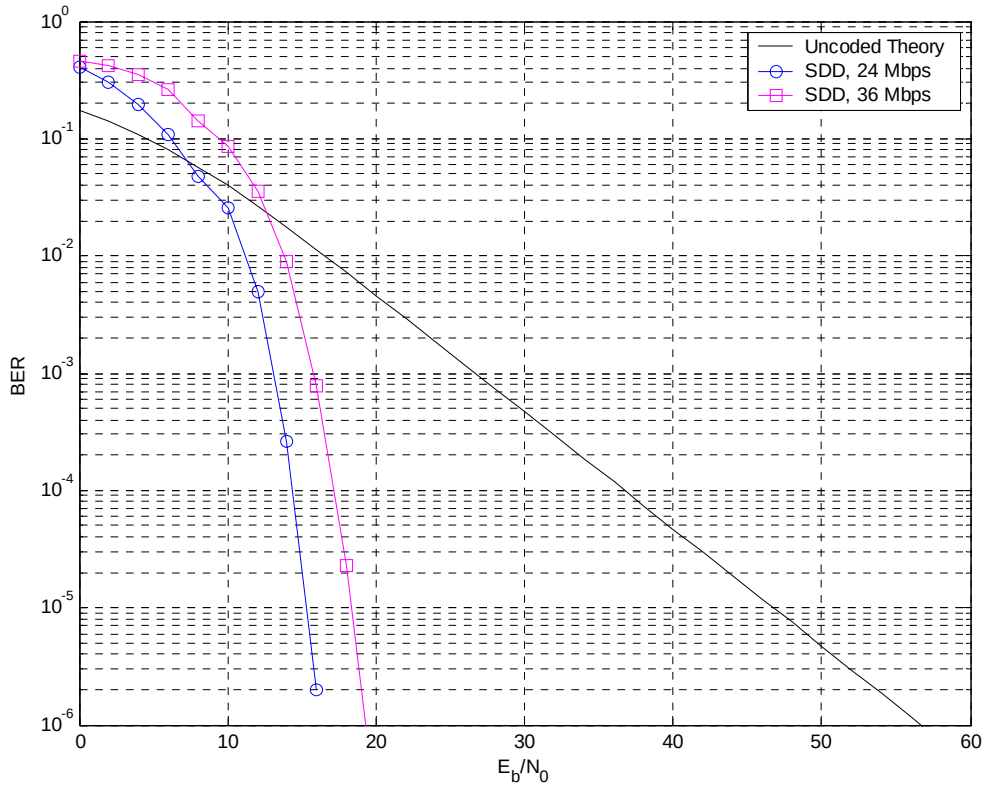

Figure 56. Performance of IEEE 802.11a 16-QAM Modulation in an Exponential-decaying Channel, 50 ns RMS Delay Spread

We observe that the coding gain is even higher than in BPSK/QPSK modulation. In particular, at $\text{BER} = 10^{-6}$, the coding gain for 24 Mbps is roughly 40 dB, while for 36 Mbps the coding gain is 38 dB. The performance difference between 24 Mbps and 36 Mbps is again 2 dB, due to the different coding rates used.

Finally, in Figure 57 the performance of IEEE 802.11a 64-QAM modulation is depicted, for both available coding rates and weighted SDD. Additionally, the PER for all operational modes and SDD is illustrated in Figure 58

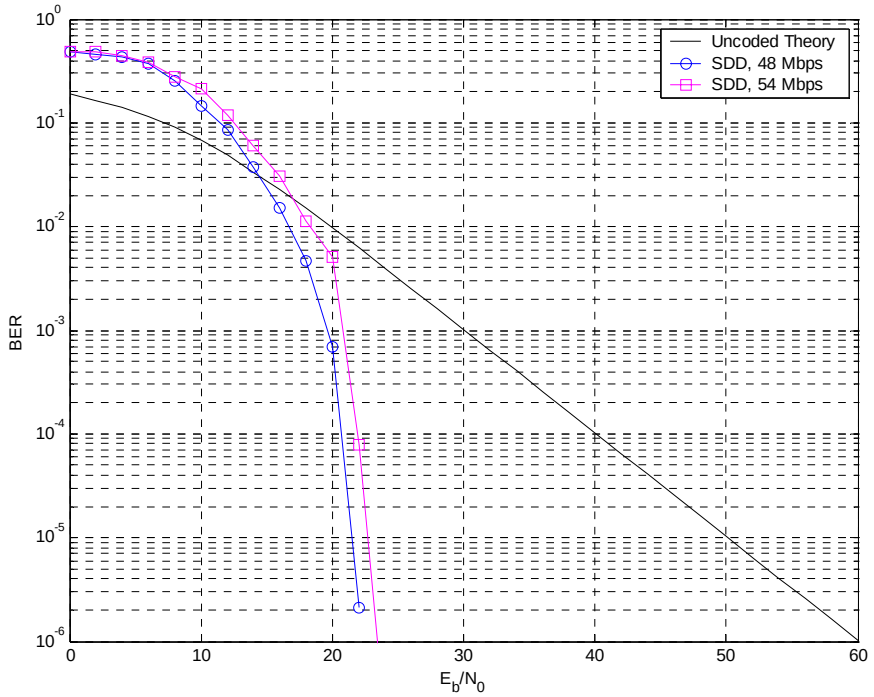

Figure 57. Performance of IEEE 802.11a 64-QAM Modulation in an Exponential-decaying Channel, 50 ns RMS Delay Spread

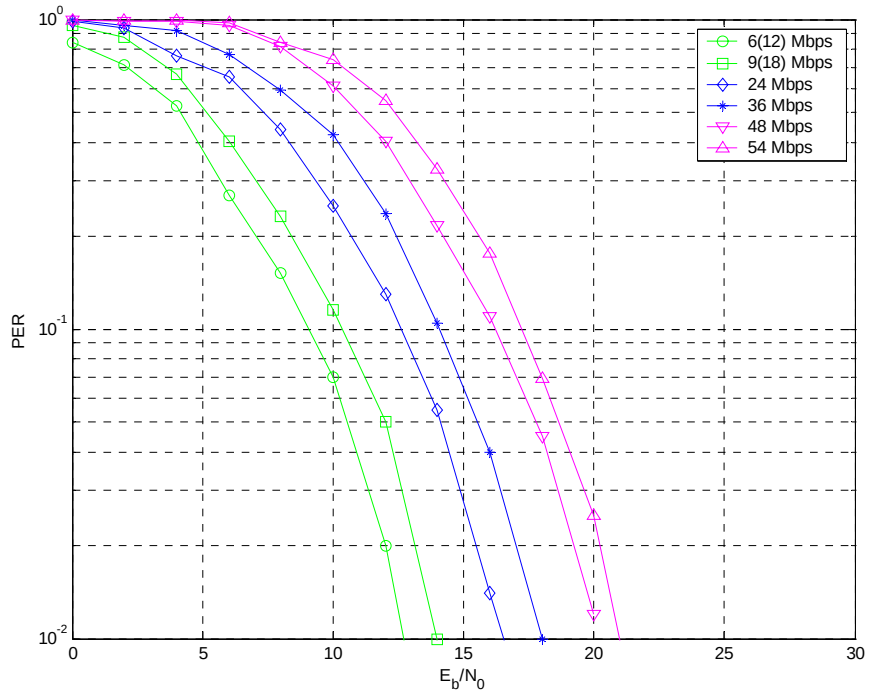

Figure 58. Packet Error Rate of IEEE 802.11a Using Weighted SDD in an Exponential-decaying Channel, 50 ns RMS Delay Spread

For 64-QAM modulation, the coding gain is 38 dB for 48 Mbps and 37.5 dB for 54 Mbps. The performance difference between the two modes is roughly 0.5 dB because the change in the coding rate is less, i.e., from $2/3$ to $3/4$.

By observing the Packet Error Rate curves, we conclude that the data throughput decreases as the data rate increases. The difference between the lowest data rate (6 Mbps) and the highest data rate (54 Mbps) is nearly 8 dB.

G. SPACE DIVERSITY

We saw that the performance of the OFDM system is dramatically improved when we employ any kind of frequency diversity. Unfortunately, for most wireless LANs, time diversity cannot be deployed, since the channel is assumed to be quasi-stationary, that is, the channel remains constant during a burst and is allowed to randomly change from burst to burst.

However, space diversity can be employed. Recent studies [31] suggest that there is tremendous capacity potential for wireless communication systems using *antenna diversity*. *Space* or *antenna diversity* is defined by multiple independent channels between the transmitter and the receiver [7]; hence, antenna diversity occurs when the independent paths are spatial in nature. That is, there is sufficient spacing between the antenna elements at the transmitter and/or receiver such that there is no or very little correlation among their respective signals. The antenna diversity can be used to either improve the link performance of a signal or increase the data throughput. In general, antenna diversity can be divided into three main categories:

- Single-input Multiple-output (SIMO) or receiver diversity.
- Multiple-input Single-output (MISO) or transmitter diversity, and
- Multiple-input Multiple-output (MIMO) or transceiver diversity.

The two latest cases are the key technology areas of the future OFDM WLAN which are beyond the scope of this thesis.

For the SIMO case, using multiple antennas at the receiver is fairly easily exploited. In essence, multiple copies of the transmitted stream are received, which can be efficiently combined using appropriate signal processing techniques. As the number of antennas increases, the effective channel approaches an additive white Gaussian noise channel [7]. The two most popular diversity techniques are *selection diversity* and *maximal ratio combining* (MRC).

1. Selection Diversity

The simplest receive diversity is selection diversity. Because of its simplicity, the current IEEE 802.11 WLAN products employ selection diversity at the mobile terminal (MT) and access point (AP) [8]. Given L receive antennas, selection diversity measures the power from each receive antenna and selects the antenna with the largest SNR in each symbol interval. The impact of selection diversity on the data throughput is illustrated in Figure 59.

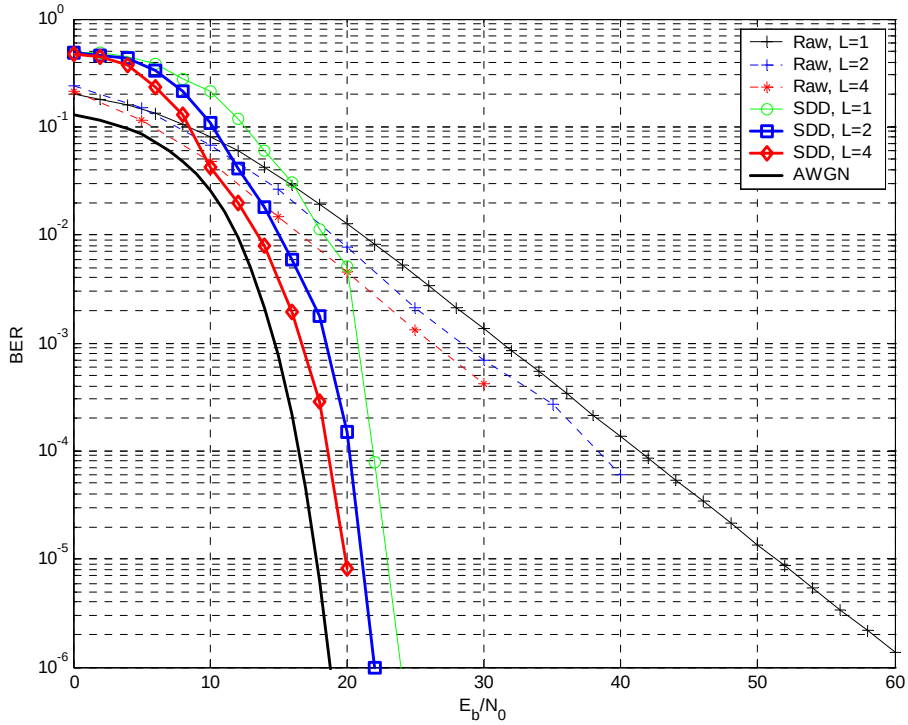

Figure 59. Performance of IEEE 802.11a 54-Mbps Mode, Employing Selection Diversity in an Exponential-decaying Channel, 50-ns RMS Delay Spread

It is clearly evident that error rate performance improves with an increasing number of receive antennas. At $\text{BER} = 10^{-6}$, the improvement in data throughput is between 2–3 dB for two receive antennas and 3–4 dB for four receive antennas. The downside of this performance improvement is that each path for the receive antennas must be independent of the others.

Another attractive feature of selection diversity is that it does not require any additional RF receiver chain [9]. In other words, all the receive antennas share a single RF receiver chain, which keeps the cost down for MT equipment. However, the simple observation that it disregards the information from all antennas but one leads us to conclude that is not an optimum combining technique.

2. Maximal Ratio Combining

In maximal ratio combining (MRC), the signals at the output of the L receive antennas are combined so as to maximize the instantaneous SNR. The coefficients that yield the maximum SNR are computed using straightforward optimization theory [7]. Let the receive signal per antenna be denoted as

$$r_l = h_l s + v_l, \tag{4.8}$$

where s is the transmitted signal, h_l is the channel's impulse response per receive antenna and v_l are i.i.d. complex Gaussian noise samples. Then, maximal ratio combining entails using the linear combination prior to detection [7] :

$$y = \sum_{l=1}^{L} w_l^* r_l = \sum_{l=1}^{L} w_l^* h_l s + \sum_{l=1}^{L} w_l^* v_l. \tag{4.9}$$

Since the DFT is a linear operation, Equation (4.9) can be implemented in a frequency domain as:

$$Y = \frac{\sum_{l=1}^{L} \hat{H}_{k,l}^{*} R_k}{\sum_{l=1}^{L} \left| \hat{H}_k \right|^2}, \tag{4.10}$$

where $\hat{H}_{k,l}$ are the channel frequency response estimates for the l antenna and R_k are the received data subcarriers. Equation (4.10) implies that the MRC also performs equalization. Thus, when MRC diversity is employed no further equalization is needed.

The performance improvement is much more significant for MRC than for selection diversity, as depicted in Figure 60.

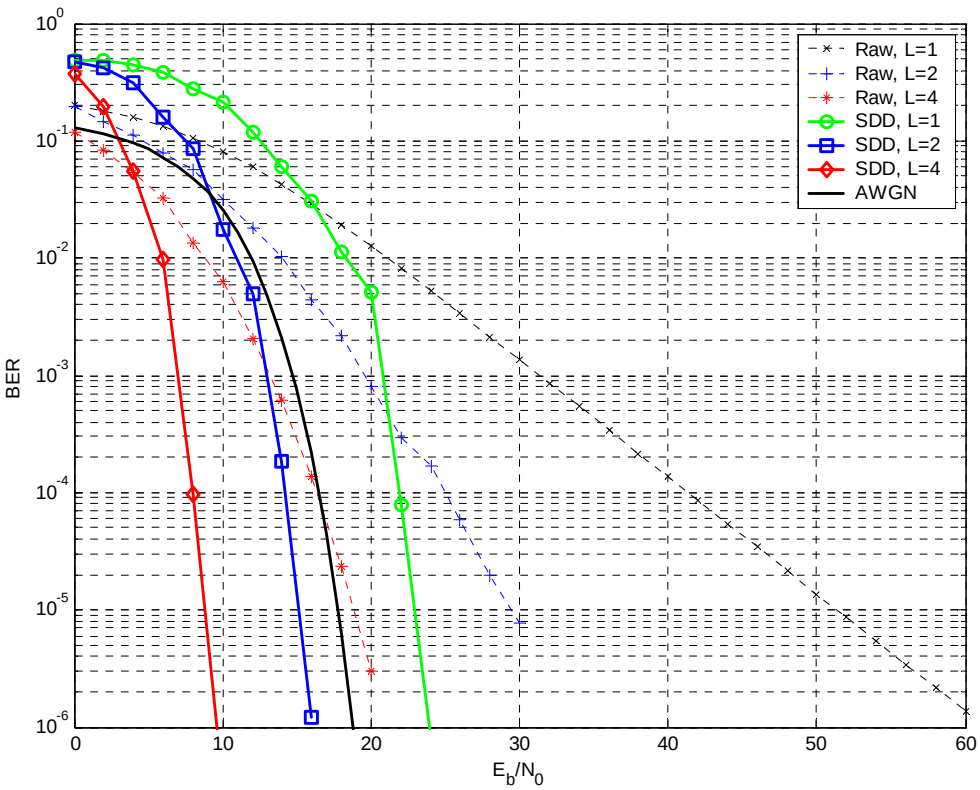

Figure 60. Performance of IEEE 802.11a 54-Mbps Mode, Employing MRC Diversity in an Exponential-decaying Channel, 50-ns RMS Delay Spread

For example, at a BER of 10^{-6}, MRC with two receive antennas provides nearly 10 dB of improvement, while for selection diversity, it was found to be 2 to 3 dB. For four receive antennas, the improvement is nearly 15 dB!

In summary, the potential gain using MRC can be tremendous. This is not surprising since it is the optimum solution. The caveat to MRC is that perfect channel knowl-

edge was assumed, which is not true in general. As we discussed in Chapter III, the accuracy of the channel estimation depends on the operating SNR.

H. SUMMARY

In this chapter, the performance of IEEE 802.11a was evaluated under many operational modes. A description of the simulation tool was given, along with the encoding process of a single PPDU frame. The system was evaluated in AWGN where it was shown that the channel coding results to a 3-dB improvement for hard decision decoding and to a 5.5-dB improvement for soft decision decoding. System evaluation was also performed in multipath fading, using the exponential channel model. It was shown that even with perfect synchronization, channel coding is not enough to recover the signal. Additional signal processing is needed, such as equalization. The huge impact of diversity on the data throughput was emphasized; frequency diversity is achieved either by using a block interleaver or by weighting the soft decisions with the channel estimates. Space diversity is achieved by using multiple antennas in such a way that the received signals are uncorrelated to each other.

The performance of all these techniques relies on accurate channel estimation. Under the assumption of a known channel, at a BER of 10^{-6}, the coding gain can be 36–40 dB for all IEEE 802.11a modes, in a fading channel of 50-ns rms delay spread. Furthermore, if antenna diversity is used, the data throughput can be dramatically improved. For instance, using four receive antennas and maximal ratio combining, the gain is 15 dB more than using only one antenna. In other words, even with the highest data rate of IEEE 802.11a, bit error rates in the order of 10^{-6} can be achieved using an SNR as low as 10 dB!

V. CONCLUSIONS AND FUTURE WORK

A simulation toolbox and a new rapid synchronization scheme were presented in this thesis. They have a general scope of applicability much larger than the special case of the IEEE 802.11a physical layer, which was used as a test-bed to evaluate the performance of the various algorithms. The same techniques can be applied to any OFDM based communication system. The main conclusions are summarized per chapter together with a suggestion for future work.

A. CONCLUSIONS

Chapter II addresses the very important issue of multipath fading in indoor wireless communications. The signal distortions and time dispersion caused by multipath fading can be accurately described by a channel model. The exponential channel waveform adopted by IEEE 802.11 Task Group b was selected to be the channel model in this thesis. The concept of orthogonal frequency division multiplexing (OFDM) was also presented. The orthogonal nature of the OFDM subchannels allows them to be overlapped, thereby increasing the spectral efficiency. The inter-symbol interference (ISI) is eliminated by adding a cyclic prefix in the OFDM symbol.

Chapter III provided a detailed discussion about many of the popular synchronization algorithms used in OFDM networks. Specifically, timing synchronization, frequency synchronization, pilot phase tracking, channel estimation and equalization were covered. A new rapid time and frequency synchronization scheme was suggested using only the short training sequence. The channel estimation can be done using either the long training sequence or the known pilot subcarrier pattern. In the latter case, the long training sequence can be skipped, thus reducing the overhead by $8\ \mu s$. Nevertheless, from the designers' perspective, the accuracy of the channel estimation algorithm should always be the number one priority, especially with OFDM systems employing coherent modulation schemes.

Finally, Chapter IV presented performance evaluations of several operational modes of the IEEE 802.11a physical specification. A brief demonstration of the simula-

tion toolbox built in Matlab was given, together with a step-by-step description of the encoding process of a single PPDU packet. The main functional parts of the simulation software were analyzed, such as the transmitter, the receiver, and the channel model. The IEEE 802.11a system was evaluated under additive white Gaussian noise, where it was found that the coding gain can be 3 to 5.5 dB for hard and soft decision decoding respectively. An evaluation was also performed under multipath fading channel conditions. This showed that the channel coding alone cannot recover the signal and thus additional signal processing is required at the receiver. This processing involves equalization and any kind of diversity. Frequency diversity can be achieved by data interleaving or by weighting the soft decisions with the channel estimates. Space diversity can be achieved by multiple antennas with uncorrelated signals. Frequency diversity can achieve a performance gain of 36 to 40 dB, for all operational modes of IEEE 802.11a. If combined with antenna diversity, such as maximal ratio combining, the performance gain can be tremendous and data throughputs near Shannon limits can be achieved.

B. FUTURE WORK

There are many areas in which follow-on research is recommended. For instance, using the simulation toolbox and slightly modifying the channel functional block, the performance of the IEEE 802.11a can be evaluated in various channel conditions such as any type of jamming or multi-user interference. Or, the new IEEE 802.11g can be evaluated, using most of the functional blocks of this software. It has to be noted that the functions are speed optimized; especially the most demanding Viterbi decoding algorithm has been hard-coded in C language and compiled as a C-Mex function for extremely fast execution. For that reason, bit error rates in the order of 10^{-7} or less can be simulated in a quite small execution time, depending on the processing speed and the system's physical memory.

The synchronization algorithms can be applied to any OFDM-based wireless LAN, such as IEEE 802.11g and HIPERLAN/2.

Finally, the toolbox can be modified to accommodate Multiple-Input Multiple-Output (MIMO) systems. Recent research in information theory suggests that there is a

tremendous capacity potential for wireless communication systems employing multiple antenna transceivers. This is the reason MIMO is considered as the key technology area of the future in wireless local area networks.

THIS PAGE INTENTIONALLY LEFT BLANK

APPENDIX A: PHYSICAL MECHANISMS LEADING TO SMALL-SCALE MULTIPATH FADING

In a typical wireless communications scenario, the transmitter and the mobile receiver are surrounded by scatterers comprised of walls, terrain, desks, chairs, etc., as well as by remote scatters. The phasor sum of the multiple waves at the receiver results in a signal that fluctuates rapidly. These signal fluctuations are known as fading; the fluctuations that occur over sub-wavelengths scale are known as small-scale fading, whereas those occuring over several wavelengths are known as large-scale fading [4]. When either the receiver or the environment moves with time, multipath fading will impose a varying envelope on a transmitted tone. Hence the frequency spectrum of the received signal will be spreaded. This phenomenon is known as *Doppler spreading*.

In order to fully understand the effects of multipath and motion on the received signal, we will consider a simple model of two plane waves arriving at the receiver from the azimouth plane.

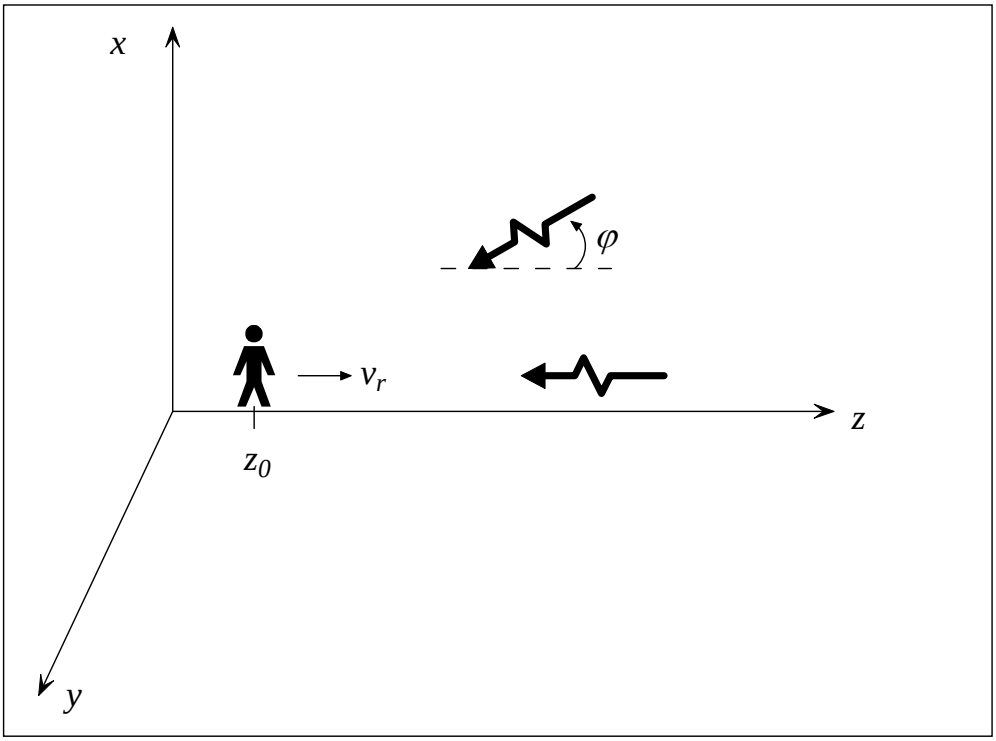

Figure 61. Two Plane-wave Model

Figure 61 illustrates two plane waves, each of equal amplitude $E_0/2$, carrier frequency ω_c, arriving from azimuth angles 0 and ϕ. The receiver moves along the *z*-axis, at a constant speed v_r. These two plane waves may be thought of as a direct signal from the transmitter and a scattered signal. The azimouth angles are measured from the *z*-axis. Using phasor notation, the total received signal is

$$\begin{aligned} r(t) &= \mathrm{Re}\left\{e^{i\omega_c t}\, E_0 e^{ik_0 z_0}/2\right\} + \mathrm{Re}\left\{e^{i\omega_c t}\, E_0 e^{ik_0 z_0 \cos\phi}/2\right\} \\ &= \mathrm{Re}\left\{E_0 e^{i\omega_c t}\left(e^{ik_0 z_0} + e^{ik_0 z_0 \cos\phi}\right)/2\right\}, \end{aligned} \tag{A.1}$$

where $k_0 = \omega/c = 2\pi/\lambda$ is the wavenumber in free-space, *c* is the speed of light in free-space and $\lambda = c/f$ is the radio wavelength in free space. Equation (A.1) can be further manipulated as follows:

$$\begin{aligned} r(t) &= \mathrm{Re}\left\{E_0 e^{i\omega_c t}\left(e^{ik_0 z_0 \cos^2\frac{\phi}{2}} e^{ik_0 z_0 \sin^2\frac{\phi}{2}} + e^{ik_0 z_0 \cos^2\frac{\phi}{2}} e^{-ik_0 z_0 \sin^2\frac{\phi}{2}}\right)\Big/2\right\} \\ &= \mathrm{Re}\left\{E_0 e^{i\omega_c t} e^{ik_0 z_0 \cos^2\frac{\phi}{2}} \cos\left(k_0 z_0 \sin^2\frac{\phi}{2}\right)\right\} \\ &= \underbrace{E_0 \cos\left(k_0 z_0 \sin^2\frac{\phi}{2}\right)}_{\text{Envelope}} \underbrace{\cos\left(\omega_c t + k_0 z_0 \cos^2\frac{\phi}{2}\right)}_{\text{Carrier}}. \end{aligned} \tag{A.2}$$

From Equation (A.2) it can be seen that the frequency of the carrier signal is changed from ω_c to $\omega_c + k_0 v_r \cos^2(\phi/2)$. The extra term depends on the speed of the receiver as well as on its relative motion with respect to the incoming plane wave.

The frequency spectrum of the transmitted and the received signal is depicted in Figure 62. Clearly, the transmitted spectrum has spread due to multipath fading and motion of the receiver. This frequency broadening is also known as *Doppler spread*.

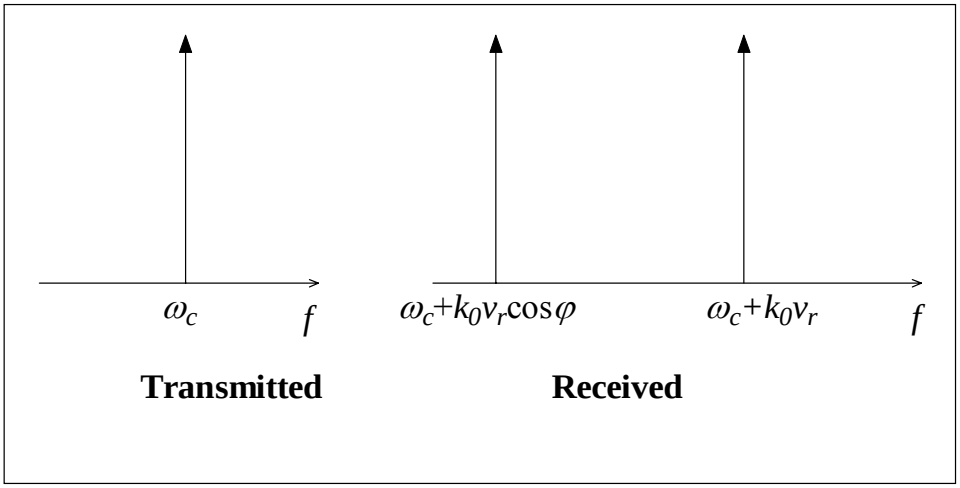

Figure 62. Doppler Spread for a Two Plane-wave Model (After Ref. [6].)

On the other hand, the magnitude of the carrier envelope is no longer constant but equal to

$$\left|\mathrm{Env}\left[\mathrm{r(t)}\right]\right| = E_0\left|\cos\left(k_0 v_r t \sin^2\frac{\phi}{2}\right)\right|, \tag{A.3}$$

where $\mathrm{Env}\left[r(t)\right]$ denotes the envelope of the received signal. Equation (A.3) shows that the envelope changes with time in a periodic manner and the rate of change depends not only on the speed of the receiver but also on the angle of arrival of the waves. The magnitude of the envelope goes from a peak value of E_0 to a minimum value of zero in a time T equal to

$$T = \frac{\lambda}{4v_r \sin^2\frac{\phi}{2}} = \frac{c}{4v_r f \sin^2\frac{\phi}{2}}. \tag{A.4}$$

For example, if $\phi = \pi$, $f = 5.2$ GHz and $v_r = 1$ m/s (walking speed), then $T = 14.4$ ms and the radio channel has changed over this time.

In an actual situation there may be more than just two plane waves and the amplitudes of these waves may also be different. As the mobile receiver passes through this multipath field in a random fashion, both the carrier frequency and the signal envelope will change randomly with time. In other words, the Doppler spread results to a time-

varrying channel. As the multipath phenomenon is random, the channel transfer function will be a random process.

LIST OF REFERENCES

[1] W.C. Jakes, *Microwave Communications,* IEEE Press, New York, 1974.

[2] P.A. Bello, "Characterization of Randomly Time-Variant Linear Channels," *IEEE Trans. on Communication Systems,* Vol. CS-11, pp. 360-393, December 1963.

[3] R. Heddergott, B.H. Fleury, and U.P. Bernhard, "Stochastic Radio Channel Model for Advanced Indoor Mobile Communication Systems", Tech. Rep. COST 259 TD (98) 057, COST 259, Bradford, UK, Apr. 1998.

[4] B. Sklar, *Digital Communications: Fundamental and Applications,* 2nd ed., Prentice Hall, Upper Saddle River, NJ, 2001.

[5] T.S. Rappaport, *Wireless Communications: Principles and Practice,* 2nd ed., Prentice Hall, Upper Saddle River, NJ, 2002.

[6] R. Janaswamy, *Radiowave Propagation and Smart Antennas for Wireless Communications*, Kluwer Academic Publishers, Norwell, MA, 2000.

[7] J.G. Proakis, *Digital Communications,* 4th ed,. McGraw Hill, New York, 2001.

[8] B. O'Hara and A. Petrick, *IEEE 802.11 Handbook: A Designer's Companion,* Standards Information Network IEEE Press, New York, 1999.

[9] J. Terry and J. Heiskala, *OFDM Wireless LANs: A Theoretical and Practical Guide,* Sams Publishing, Indianapolis, IN, 2002.

[10] A. Papoulis, *Probability, Random Variables, and Stochastic Processes*, 2nd Edition, McGraw-Hill, New York, 2000.

[11] J. Fakatselis, *IEEE 802.11-97/157-r1*, November 1997. http://grouper.ieee.org/groups/802/11/Documents/DocumentArchives/1997_docs/97novp.zip (last accessed April 2004.)

[12] S. Halford, K. Halford, and M. Webster, *IEEE 802.11-00/282r2*, September 2000. http://grouper.ieee.org/groups/802/11/Documents/DocumentHolder/0-282.zip (last accessed April 2004.)

[13] S. S. Haykin, *Adaptive Filtering Theory,* Fourth Edition, Prentice Hall, Englewood Cliffs, N.J., 1995.

[14] H. Harada and R. Prasad, *Simulation and Software Radio for Mobile Communications,* Artech House Publishers, Boston, 2000.

[15] A. R. S. Bahai and B. R. Saltzberg, *Multicarrier Digital Communications: Theory and Applications of OFDM,* Kluwer Academic/Plenum, New York, 1999.

[16] R. van Nee and R. Prasad, *OFDM for Mobile Multimedia Communications,* Artech House, Boston, 1999.

[17] W. Stallings, *Wireless Communications and Networks,* Prentice Hall, Upper Saddle River, New Jersey, 2002.

[18] A. V. Oppenheim and R. W. Schafer, *Discrete-Time Signal Processing,* Prentice Hall, Englewood Cliffs, New Jersey, 1989.

[19] IEEE 802.11a, "Wireless LAN Medium Access Control (MAC) and Physical Layer (PHY) specifications: High-speed Physical Layer in the 5 GHZ Band," IEEE Std 802.11a-1999. http://ieeexplore.ieee.org/xpl/tocresult.jsp?isNumber=17645 (April 2004.)

[20] T. M. Schmidl and D. C. Cox, "Low-Overhead, Low-Complexity [Burst] Synchronization for OFDM," *IEEE International Conference on Communications,* Vol. 3., pp 1301-1306, 1996.

[21] T. Pollet, M. van Bladel, and M. Moeneclaey, "BER Sensitivity of OFDM Systems to Carrier Frequency Offset and Wiener Phase Noise," *IEEE Trans. on Communications,* Vol. 43, Issue 2, Part 3, pp. 191-193, February, March, April 1995.

[22] P. H. Moose, "A Technique for Orthogonal Frequency Division Multiplexing Frequency Offset Correction," *IEEE Trans. on Communications,* Vol. 42, No. 10, pp. 2908-2914, October 1994.

[23] J-J. van de Beek, M. Sandell, and P. O. Börjesson, "ML Estimation of Time and Frequency Offset in OFDM Systems," *IEEE Trans. on Signal Processing,* Vol. 45, No. 7, pp. 1800-1805, July 1997.

[24] M. Speth, D. Daecke, and H. Meyr, "Minimum Overhead Burst Synchronization for OFDM Based Broadband Transmission," *IEEE Global Telecommunications Conference,* Vol. 5, pp. 2777-2782, 1998.

[25] J-J. van de Beek, O. Edfors, M. Sandell, S. K. Wilson, and O. Borjesson, "On Channel Estimation in OFDM Systems," *IEEE Proc. VTC-1995,* Vol. 2, pp. 815-819, Chicago, July 1995.

[26] S. M. Kay, *Fundamentals of Statistical Signal Processing: Detection Theory*, Prentice Hall, Upper Saddle River, New Jersey, 1998.

[27] S.R. Searle, *Matrix Algebra Useful for Statistics,* John Wiley & Sons, New York 1982.

[28] S. B. Wicker, *Error Control Systems for Digital Communication and Storage*, Prentice-Hall, Upper Saddle River, New Jersey, 1995.

[29] L. H. Lee, *Error-Control Convolutional Coding*, Artech House, Boston, 1997.

[30] C. Kao, "Performance of the IEEE802.11a Wireless LAN Standard Over Frequency-Selective, Slow, Rician Fading Channels", Master's Thesis, Naval Postgraduate School, Monterey, CA, 2002.

[31] G. J. Foschini and M. J. Gans, "On Limits of Wireless Communications in a Fading Environment When Using Multiple Antennas," *Wireless Personal Communications 6,* no. 3, pp. 311-335, March 1998. http://www.bell-labs.com/project/blast/wpc-v6n3.pdf (last accessed April 2004.)

THIS PAGE INTENTIONALLY LEFT BLANK

INITIAL DISTRIBUTION LIST

1. Defense Technical Information Center
   Ft. Belvoir, Virginia

2. Dudley Knox Library
   Naval Postgraduate School
   Monterey, California

3. Chairman, Department of Physics, Code PH/Lu
   Naval Postgraduate School
   Monterey, California

4. Chairman, Department of Electrical and Computer Engineering, Code EC
   Naval Postgraduate School
   Monterey, California

5. Professor Tri T. Ha, Code EC/Ha
   Department of Electrical and Computer Engineering
   Naval Postgraduate School
   Monterey, California

6. Professor Brett H. Borden, Code PH/Bo
   Department of Physics
   Naval Postgraduate School
   Monterey, California

7. Embassy of Greece, Naval Attaché
   Washington, DC

8. Michail Segkos
   Labraki 32, Elefsis
   19200, GREECE